Structure-property correlations in metallic glass and amorphous carbon films

By

Sachin V. Muley

A dissertation submitted in partial fulfillment of

the requirements for the degree of

Doctor of Philosophy

(Materials Science and Engineering)

at the

UNIVERSITY OF WISCONSIN – MADISON

2021

Date of final oral examination: 01/14/2021

The dissertation is approved by the following of the Final Oral Committee:

Voyles, Paul, M. Professor, Materials Science and Engineering
Ediger, Mark, D. Professor, Chemistry
Lagally, Max, G. Professor, Materials Science and Engineering
Morgan, Dane, Professor, Materials Science and Engineering
Kawasaki, Jason, K. Assistant Professor, Materials Science and Engineering

Dedicated to my family, without whom none of this was possible

Acknowledgments

Over the duration of my graduate studies, I have grown immensely in a professional and personal capacity. I owe my gratitude to all the brilliant mentors, collaborators and peers I have had the good fortune of working together with. First and foremost, I would like to profusely thank my advisor, Prof. Paul Voyles and mentor, Dr. Felix Lu for their constant encouragement and unwavering support during my graduate studies. Their patient and infectiously upbeat demeanor in the face of research difficulties rubbed off on me thus, cultivating the mental fortitude needed for research. Prof. Voyles' enthusiasm for research, expertise over a variety of areas, honesty and friendly demeanor have left a deep impression on me. I am grateful for all the opportunities he has given me, his strong support, praise and constructive critical remarks, which have helped me grow tremendously over the duration of my studies. I also want to thank my thesis committee for all their help and feedback throughout my stay at UW-Madison – Prof. Mark Ediger, Prof. Dane Morgan, Prof. Max Lagally and Prof. Jason Kawasaki.

My work has benefitted immensely from useful research discussions, feedback and collaborations within the Wisconsin Materials Research Science and Engineering Center's Interdisciplinary Research Group 1 (MRSEC-IRG1), especially Prof. Mark Ediger, Prof. John Perepezko, Prof. Lian Yu, Prof. Dane Morgan, Prof. Izabela Szlufarska, Prof. Frances Hellman, Prof. Clare Yu, Prof. Bu Wang, Dr. Chengrong Cao, Dr. Chaiyapat Tangpatjaroen, Dr. Ajay Annamareddy, Dr. Ye Shen, Wei Tang, Dr. Camille Bishop, Dr. Kushal Bagchi, Dr. Ankit Gujral, Dr. Li He, Vrishank Jambur, Thomas Dauer, and Zhenxuan Chen.

I am deeply indebted to faculty, students and staff for advice with research, experiments and instrumentation at the Materials Science and Engineering department, notably Prof. Donald

Stone, Prof. Kumar Sridharan, Prof. Paul Evans, Prof. Susan Babcock, Prof. Chang-beom Eom, Prof. Jason Kawasaki, Prof. Michael Arnold, Prof. John Pfotenhauer, Dr. John Jacobs, Dr. Julie Morasch, Dr. Jon McCarthy, Dr. Rick Noll, Dr. Mike Efremov, Dr. Don Savage, Dr. RB Jacobson, Dr. Joseph Jakes, Dr. Meng Gao, Dr. Austin Way, Dr. Robert Jacobberger, Dr. Jialiang Wang, Dr. Yajin Chen, Dr. Gerald Brady, and Chris Kailhofer. Machining by Steve Myers, Matthew Martin, Joel Ballweg, and Mike Hughes and vacuum leak-checking assistance by Gabriel Bernhardt and Zhiyi Zhang are highly appreciated. Composition measurements and interesting discussions with Dr. John Fournelle and Dr. Will Nachlas are acknowledged. I would also like to thank the many current and former support staff in Materials Science, especially Julie Gibes, Rebekah Turner, Diana Rhoads, Cynthia Rothwell, Annie Anderson, and Mary Sams for making the department such an enjoyable place to work.

A significant portion of my thesis involved industrial and academic research with organizations outside the University of Wisconsin-Madison. These opportunities expanded my exposure to materials research beyond metallic glasses in diverse areas such as industrial amorphous carbon coatings, high temperature superconductors, and mash seam welding. I want to thank all of my non-UW supervisors and collaborators for the opportunity to work on interesting projects and supporting my growth as a research professional, especially Dr. Patrick Heaney and Dr. Aiping Zeng at NCD Technologies, Dr. Qing Ji, Dr. Xiaorong Wang, Aurora Cecilia Araujo-Martinez, Dr. Andre Anders, Dr. Arun Persaud, Joseph Wallig, Tak Katanayagi and Dr. Tevye Kuykendall at Lawrence Berkeley National Laboratory, and Dr. Bruce Krakauer at A.O. Smith Corporation.

Thanks are also due to all current and previous Voyles group members for their help and friendship over the years, especially Dr. Alexander Kvit, Dr. Ashutosh Rath, Dr. Pei Zhang, Dr. Jason Maldonis, Debaditya Chatterjee, Carter Francis, Dr. Chenyu Zhang, Dr. Xing Wang, Dr. Congli Sun, Dr. Jie Feng, Dr. Xuying Liu, Yizhang Zhai, Dr. Andrew Yankovich, Dr. Dan Zhou, Dr. Min Yu, Shuoyuan Huang, John Sunderland, Jingrui Wei, Sriraksha Srinivasan, David Schyns, Malcolm Clark, and Alexander Bickelhaupt.

My research was primarily supported by National Science Foundation (NSF) through the University of Wisconsin Materials Research Science and Engineering Center (DMR-1720415), including sample synthesis, thermal and mechanical analysis, and structural characterization. I gratefully acknowledge the use of facilities and instruments supported by NSF through the University of Wisconsin MRSEC (DMR-1720415).

During my PhD, I discovered my passion for communicating research to a general audience by participating in the various outreach activities of Wisconsin MRSEC, Lawrence Hall of Science and the Wisconsin Initiative for Science Literacy Thesis Award program. I would like to thank Dr. Anne-Lynn Gillian-Daniel, Dr. Matt Stillwell, Veronica Urdaneta, Prof. Bassam Shakhashiri, Elizabeth Reynolds and Cayce Osborne for introducing me to the joys of science outreach.

My former undergraduate advisor, Prof. Gajanan Chaudhari deserves special mention for motivating me towards a research career early on. I have benefitted immensely from his mentorship throughout my undergraduate and graduate studies. I am deeply thankful for the strong friendships I built during my time in graduate school, especially with my roommates Dr. Raunak Bardia, Aashrith Saraswathibhatla, Dr. Prashant Kumar, Kunal Bhagat, Debayan Chaudhary, Dr. Palak Bhushan; and my dear friends, Dr. Yash Govind, Neha Godwal, Ayaansh Govind, Nidhi

Tyagi, Dr. Shreya Goel, Dr. Vivek Saraswat, Nitish Mathur, Kshiteej Mahajan, Dr. Arpit Agarwal, Soumil Gurjar, Keshav Mathur, Dr. Mrugank Bhatt, Dr. Swapnil Haria, Kaivalya Molugu, Dr. Shalaka Burlawar, Dr. Sumeet Katariya, Dr. Indroneil Ghosh, Dr. Gulpreet Kaur, Tithy Sahu, Salil Apte, Atindra Bandi, Sagar Tupkar, Parthe Pandit, Dr. Girish Sharma, Dr. Ankita Bhutani, Sukriti Singh, Babita Yadav, Viraj Belekar, Dr. Anand Puranik, Dr. Poonam Mahajan-Puranik, Anika Puranik, and Urvi Puranik.

Finally, none of this would have been possible without the constant support and sacrifices by my immediate family especially my parents and sister, and extended family, Prof. Ravindra Paretkar, Pratibha Paretkar, Dr. Dadhichi Paretkar, Dr. Anja Paretkar, Neils-Salil Paretkar and Mira Paretkar.

Abstract

Structure-property correlations are invaluable expertise to advance materials' technologies since well-designed materials offer a serious competitive edge, and robust failure analyses complement process improvements. This thesis invokes structure-property interrelationships with a focus on improving materials' performance for industrial adoption of various technologically important systems. In chapter 4, we studied the structure and properties of Zr-Cu-Al thin films synthesized by magnetron sputtering as a function of deposition parameters. In chapter 5, we investigated the structure, mechanical properties and scratch behavior in single-layered and multilayered amorphous carbon thin films made by NCD Technologies' proprietary vapor deposition method. In chapter 6, we presented a case study to identify the failure mode of upper copper weld wheels in an industrial production line which had a much shorter lifetime than the lower electrode.

Vapor deposition forms metallic glasses with novel thermodynamic and kinetic stabilities unachievable through conventional routes. In chapter 4, kinetic stability in Zr-Cu-Al metallic glass thin films, indicated by their glass transition temperature, was widely varied by changing deposition rate at constant temperature. The most kinetically stable film's reduced modulus was 22% higher than a glass of the same composition quenched from the liquid by melt spinning, suggesting increased density and improved thermodynamic stability. Fluctuation electron microscopy and angular correlations studies performed using coherent electron nanodiffraction attributed enhanced stability in glasses to increased nanoscale structural order at the medium range length scale, especially of icosahedral nature. Our results indicated that increased nanoscale

icosahedral order contributed to resistance of glass to both glass transition and mechanical deformation.

In chapter 5, the elastic modulus and hardness in single-layered amorphous carbon films were improved up to as much as 35 and 30 % respectively by varying the applied bias voltage and pulse width. Film structure measured by Raman spectroscopy showed that the maxima in mechanical properties due to bias voltage was correlated to highest sp^3 fraction, highest sp^2 disorder and overall lowest disorder. Based on single-layer results, multilayers were developed. Nanoindentation and scratch-testing revealed that while multilayering preserved high hardness and improved friction behavior irrespective of the recipe, the scratch volume was strongly correlated with hardness.

Table of Contents

List of figures

Declaration of source publications adapted in this thesis

The work in this dissertation is adapted from the following manuscripts which are either under consideration or will be submitted for publication in the future.

Chapter 4 is adapted from the manuscript: S. V. Muley, C. Cao, D. Chatterjee, C. Francis, F. P. Lu, M. D. Ediger, J. H. Perepezko, P. M. Voyles. *Varying kinetic stability, icosahedral ordering, and mechanical properties of a model Zr-Cu-Al metallic glass by sputtering.* Under review at Physical Review Materials.

Chapter 5 is adapted from the manuscript: S. V. Muley, A. Zeng, P. M. Voyles, P. J. Heaney. *Optimizing mechanical properties in single-layered and multi-layered amorphous carbon coatings for industrial applications.* To be submitted.

Chapter 6 is adapted from the manuscript: S. V. Muley, J. J. McCarthy, B. K. Krakauer. *Case study: Investigation of shorter lifetime of upper Cu weld wheels in an industrial mash seam welding setup.* To be submitted.

Chapter 1 Wisconsin Initiative for Science Literacy thesis chapter

This chapter of my PhD thesis aims to provide context for the general public to understand the new knowledge I created during my graduate school studies. Here, I discuss one (albeit major) out of three themes in my PhD thesis. Through this chapter, a more important personal goal for me is to share the deep sense of wonder and curiosity that I have experienced in trying to understand the physical world around me. I take this opportunity to thank all the members of the Wisconsin Initiative for Science Literacy at UW-Madison, especially Prof. Bassam Shakhashiri, Elizabeth Reynolds and Cayce Osborne for providing this platform, and for enabling the creation of this chapter. I have drawn inspiration from WISL Thesis Chapters written by my fellow students, namely Drs. Camille Bishop and Madeleine Beasley. I also want to acknowledge the very useful feedback on this chapter by my advisor Prof. Paul Voyles, mentor Dr. Felix Lu, Dr. Anne Lynn Gillian-Daniel and Dr. Matt Stilwell from the Wisconsin MRSEC, and my friends Ashley Tucewicz and Prarthana Prabhakar.

1.1 What is a metallic glass or any glass for that matter?

Glass, as a word, is most familiar to us through windows, cookware, and phone screens. Given that I am writing this document in the year 2020, most of us are now spending a lot of time staring at phone screens. Although a cracked cell phone screen is a pet peeve most people have experienced, modern cell phone screens are truly at the cutting edge of current glass technology. Over the past several years, phone manufacturers have improved the glass materials used to make phone screens to the point where we do not need screen protectors. The newly released Apple iPhone 12, developed with Corning Inc., boasts of a practically shatter-proof glass display. The carefully engineered glass structure provides a mechanism to deflect and arrest cracks.

Interestingly, glasses have been made for over 3000 years, yet glass making technology continues to evolve together with advances in our understanding of glass science.

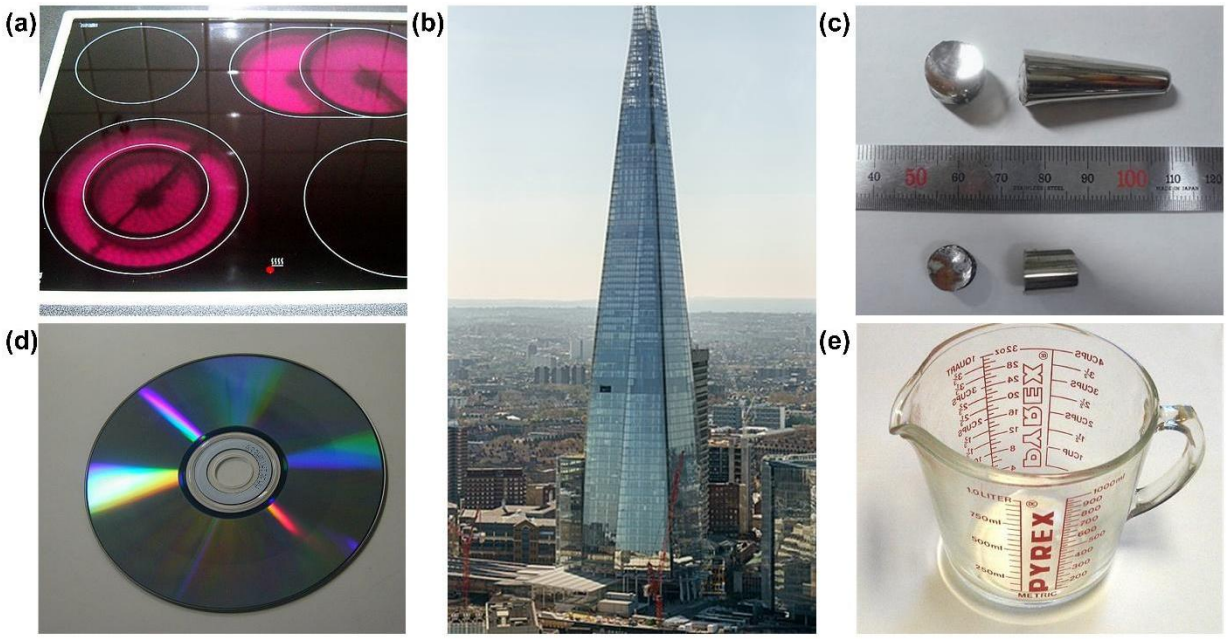

Figure 1*: Glasses used in common everyday applications such as (a) ceramic glass cooktop [1], (b) glass building [2], (c) metallic glass [3], (d) rewritable compact disc coated with chalcogenide glass [4], and (e) Pyrex measuring cup [5] are shown.*

Solids come in two main types: crystals and glasses. In crystals, like table salt, atoms pack together in a repeating pattern. In glasses, the atoms pack together without a repeating pattern. A wide range of materials, like metals (e.g. copper, iron), polymers (e.g. nylon), and pharmaceuticals (e.g. aspirin), form glasses, so long as their microscopic structure is disorganized as shown in Figure 2(a). When melting and cooling something, like water/ice, the atoms typically have enough time while cooling down to rearrange into repeating patterns. The most common way to make a glass is to melt something and then cool it down so quickly that the atoms do not have enough time

to find their places in the repeating pattern before they freeze into place. In theory, glasses could be made from any kind of liquid. In practice, only some materials form a glass.

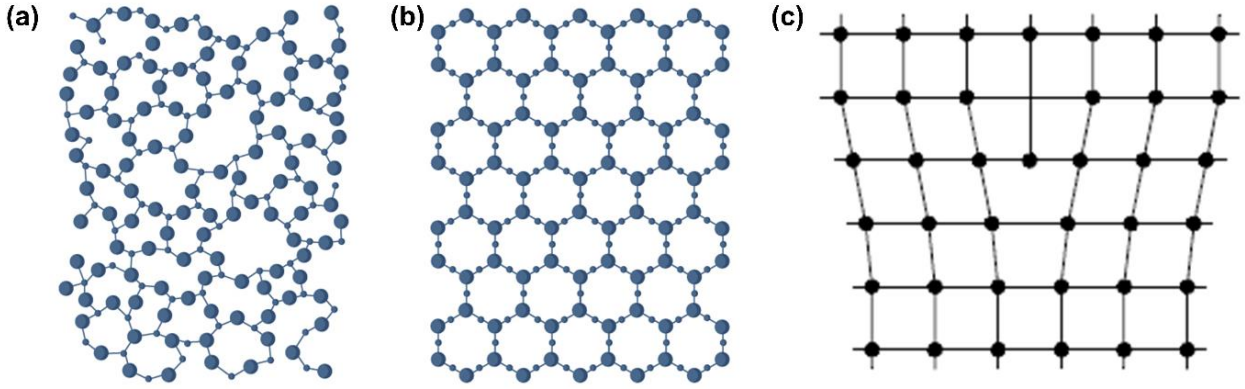

Figure 2*: Example atomic structures of a (a) glass and (b) crystal are shown. (c) shows a type of dislocation or imperfection in solid. Reproduced from [6,7]*

Crystalline metals such as copper and iron are commonly used in many everyday applications. Metal atoms in a solid crystal are like marbles in a jar that pack together in repeating patterns, just touching, and with little spaces in between. Upon filling the jar with sand, the much smaller sand grains fill gaps and make displacing the marbles more difficult than before. Similarly, metallic alloys are mixtures of metal atoms and commonly form regularly arranged crystals. For example, iron is a metal composed of one type of atoms, but steel made by adding small amounts of carbon to iron is an alloy. People use alloys since metals composed of only one type of atoms may not have exactly the right properties for a particular application. Iron can be a versatile material for many uses, but steel is stronger, harder, and rust proof. However, crystalline metals show a common crystal defect called a dislocation, as seen in Figure 2(c). Dislocations can occur when an atom is missing from a crystal or when an atom sneaks in where it does not belong,

disrupting the repeating pattern. Dislocations govern many of the mechanical property limitations, like strength, of common alloys.

Figure 3*: Picture of frictionless gearboxes being developed by NASA. Source [8]*

Alternatively, promoting a non-repeating arrangement of atoms can result in potentially useful properties. While fast cooling is essential to form a non-repeating structure, such a structure can be further promoted by mixing metallic atoms. Such materials formed by fast cooling and mixing different sized atoms to form non-repeating patterns are also called metallic glasses. Shaking the previously mentioned jar of marbles and sand particles vigorously will move its contents around, like continually moving atoms in molten metals. When the shaking is stopped abruptly, the contents will freeze in their place in a disordered way, just like atoms in a fast-cooled glass would. This analogy explains the common way to make glasses by fast cooling. Their non-repeating atomic structure results in a lack of dislocations resulting in metallic glasses being much stronger (3-4 times or more) than their crystalline counterparts. Metallic glasses, when heated and processed, provide great flexibility in the shapes they can be made into. These unique properties mean potential uses in novel applications. For example, exploring remote, extreme space environments presents an opportunity to develop materials so the hardware can survive harsh, cold

conditions like Jupiter's icy moon, Europa. Since metallic glass does not get brittle in extreme cold, NASA is developing frictionless gearboxes made from them, shown in Figure 3.

1.2 Thesis research summary

During my Ph.D., I made novel glasses using a new approach called thin film deposition to make glasses with a higher hardness than is possible when using the more common method of fast cooling. With this approach, I slowly built up very thin layers of atoms, kind of like stacking marbles in a box one layer at a time while gently shaking the box. To make these new glassy materials, I needed to add atoms slowly enough that the atoms could pack together tightly, but fast enough that the atoms did not find their spots in a repeating pattern (if they did this, it would be a crystal). This technique depends on many factors and is somewhat difficult to optimize. Nevertheless, it opens many doors for new applications, like coatings on complex geometries (e.g. gears), that are quite difficult to achieve without it. The result is thin layers of hard metallic glass – about 100 times thinner than a hair – with the atoms packed together very tightly. These hard, heat stable glasses are scientifically interesting because they may find uses as hard coatings in biomedical devices like scalpels, needles, and implants.

1.3 What is thin film versus bulk?

Thin films are defined as material layers being as thin as human hair or even thinner. Rather like how dust coats every surface on your desk, thin films are created as hot atoms are floating over a cool surface and stick, or condense, onto the cool surface. One way to create thin films is to deposit materials as layers on bulk objects to modify their surface properties. Depositing a thin film material is like applying paint to your house's exterior for protection against weather conditions. Thin films are technologically important and can be used because they alter surface

properties resulting in a range of functionalities. In the house painting example, water resistant paint (thin film) on a wooden house would protect the wood (bulk) from being easily damaged by water. Likewise, thin films made from chromium metal on automobile parts can protect them against ultraviolet rays and prolong their life while saving on materials and cost. Diamond coatings applied to drill bits can impart extreme hardness so they can be used to drill hard things like ceramics, porcelain, and gemstones. These materials can be made 10-10,000 times thinner than a human hair, depending on the application requirements. While the most popular application is in the materials making up computer chips, thin films have been engineered for a variety of applications, including:

- improved surface hardness and protection against wear
- resistance to oxidation and corrosion
- display screens and reflective or anti-reflective coatings
- heat sinks and barrier layers in thermal applications
- solar cells
- next generation memory devices for computers

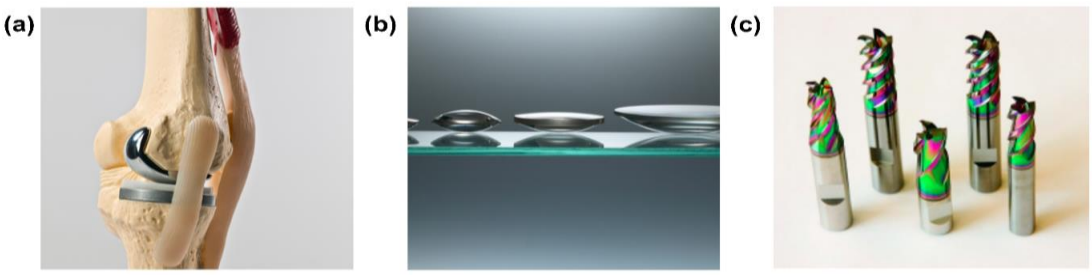

Figure 4*: Examples of thin films used in (a) biomedical implants to protect against corrosion [9], (b) optical applications requiring anti-reflective properties [9], and (c) cutting tool [10] applications to prolong drill bit lifetimes.*

1.4 How do you make thin films?

One common technique to make thin films is called physical vapor deposition (PVD). Solid or liquid materials, including metals, are vaporized in low pressure environments (or vacuum) by physical methods (such as heating). The vapors travel through vacuum and condense onto "substrates" or the bulk solids we want to coat. A useful analogy to thin film deposition would be water vapor from air fogging up a bathroom mirror or frosting on cold ice cream tubs taken out of the refrigerator. In my research, I used a PVD technique called sputtering.

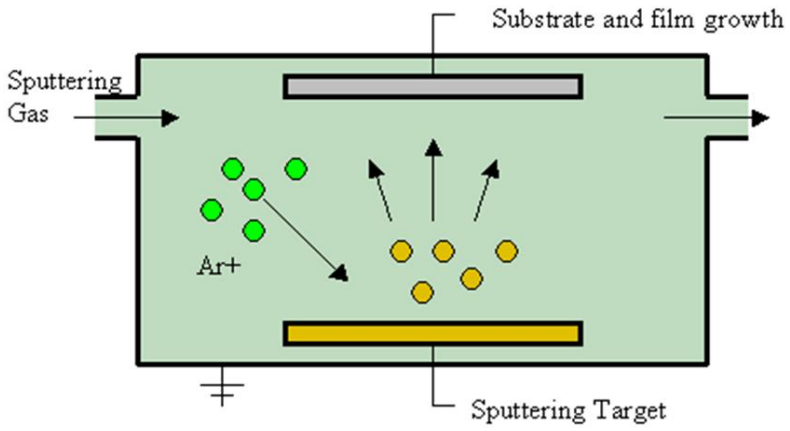

Figure 5*: Simple schematic showing sputtering process. Ar is argon gas and substrate is where you want to grow your thin film. Argon hits the sputtering target, knocking off atoms that then slowly accumulate on the substrate and grow a thin film one atom-layer at a time. Reproduced from [11]*

Sputtering uses plasma as the heat source to vaporize the material that is going to condense on the substrate. Plasma is one of the four fundamental states of matter (solid, liquid, and gas being the other three) and is composed of electrons and ions (atoms missing some of their electrons). The most familiar example of a plasma state is the sun, which is almost entirely a ball of plasma.

In the lab, we create plasmas by subjecting a non-reactive inert gas (such as argon) to powerful electromagnetic fields that creates a mixture of neutral gas atoms, ions and electrons.

Early on in my graduate school career, I did not know much about glasses. As an undergraduate student, I had dabbled in some research and was motivated by working with graduate students who clearly knew a lot more about the inner workings of the experiments we did together. Therefore, at the beginning, I was passionate to develop a deep fundamental knowledge of the experimental techniques I wanted to master for my thesis work. So, when this project presented along with itself an opportunity to rebuild a sputtering machine (pictures of the system in Figure 7) needed for my experiments, I dived right in. This project turned out to be especially tough, but now that I am on the other side of it, I really prize my learnings and feel rewarded.

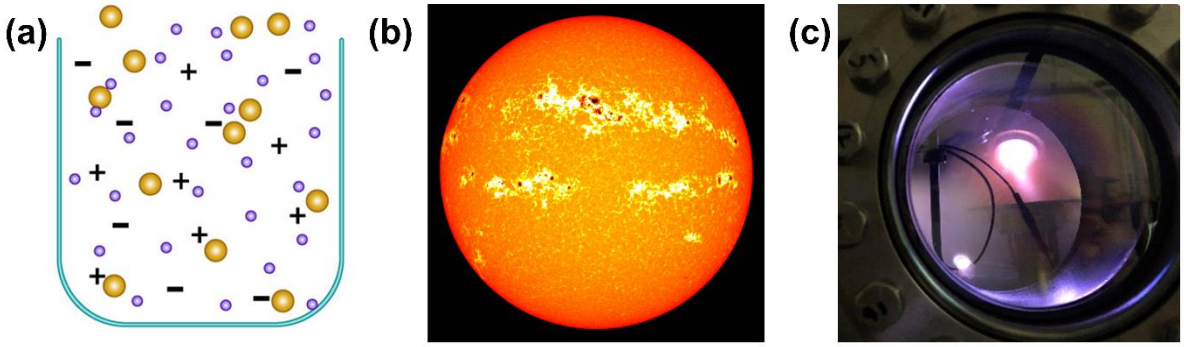

Figure 6*: (a) Schematic of plasma species [12], (b) picture of the sun [13] and (c) picture of plasma from my experiments.*

After I built my machine, I had to figure out the conditions to make glassy thin films of interest. Using the plasma state to vaporize and direct metal atoms to the substrate is a lot like playing pool: using the cue stick (the power supply controlling how the plasma is made), you aim the cue ball (plasma) at pool balls (source material) so they travel to the pockets (substrate). The

first step was to evacuate all the air from a vessel to get to a pressure like that of outer space. I achieved this by using two types of special pumps: a rotary vane pump that sucks air out and a cryopump that gets very cold (approximately 470 Fahrenheit below water's freezing temperature) so it can trap most of the gas molecules. In the second step, I heated up the substrate and allowed a tiny quantity of pure argon gas into the vessel. Next, I used a "sputter gun" to generate a plasma, which can both spark a plasma and keep it alive using electric and magnetic fields. Plasma is very energetic and when it contacts the source material, the material's atomic bonds break, vaporizing them. In my experiments, the starting material is a precisely controlled mixture of metal atoms (technically called an alloy), which is important to promote glass forming ability. Sputtering is a unique technique that can maintain the same atomic ratios in deposited thin films as the starting material.

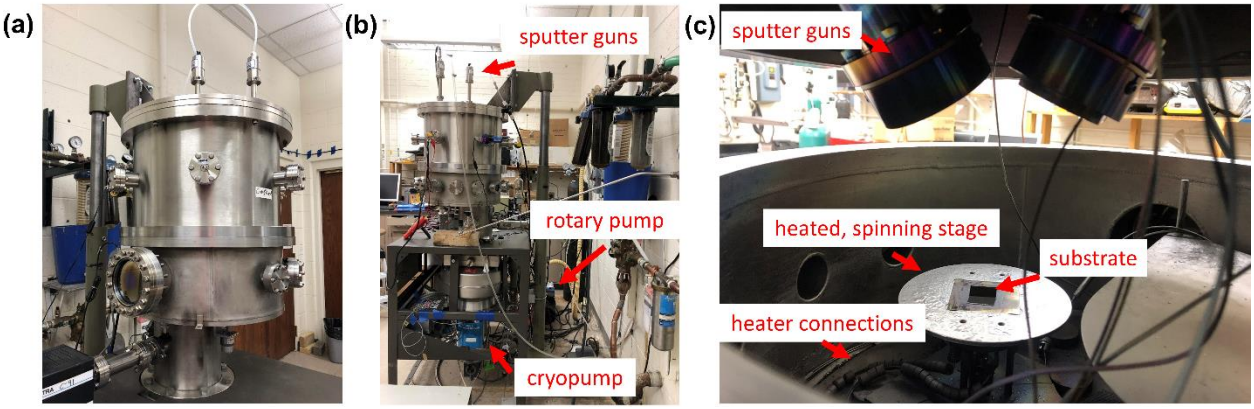

Figure 7*: (a) and (b) show two pictures from the outside of the sputtering system while (c) shows inside view.*

The metal vapor transfers through vacuum, condenses into a thin liquid layer at the substrate and then solidifies. Atoms on the surface can move as much as 100 million times faster than atoms buried beneath several layers (also called film bulk), like cold, solid ice cream staying

firm in the cone with the molten top running down the cone's sides on a hot summer day. This phenomenon is because each atom in the film bulk is surrounded by other atoms, but the surface layer has one side free of any neighbors as shown in Figure 8(a). Thus, surface atoms can move around and relax into preferred positions given enough time and energy. Therefore, a glass prepared by PVD likely has better organized atomic structure than glass made from fast cooling.

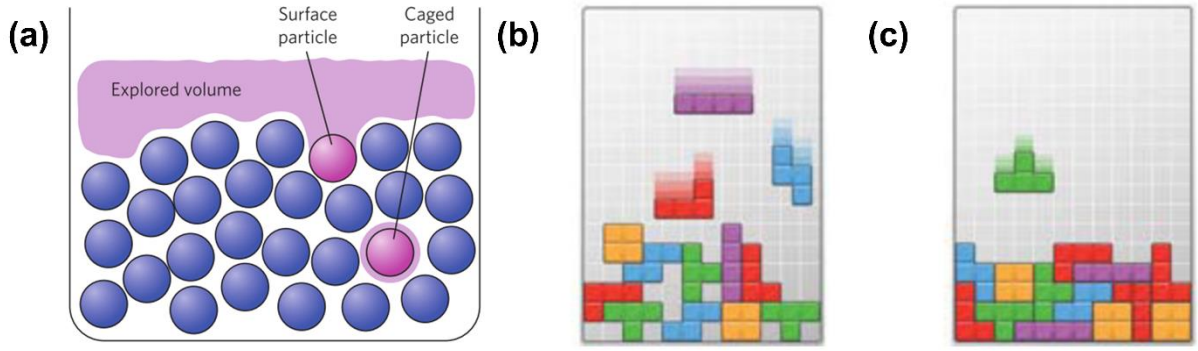

Figure 8*: (a) Schematic compares limited mobility of a bulk atom versus enhanced mobility of surface atom [14]. (b) and (c) relate vapor deposition of metallic glasses to playing Tetris: (b) is deposition at fast rates/low temperatures while (c) is deposition at slow rates/high temperatures [15].*

Next, how do we control the thin film formation process to promote better organized glass? Essentially, we have two controls on our experiment: deposition rate (or the rate at which vapor atoms arrive at the substrate) and substrate temperature. If we dial down the deposition rate to favor a layer-by-layer fashion, each atom gets a chance to be part of the "runny" surface layer. Therefore, a careful choice of slow deposition rate and optimally high substrate temperature can promote the time atoms stay at the surface and how much they move as part of this liquid layer. I would like to end this section by giving my favorite analogy about the effect of deposition rate on glass structure (borrowed from Drs. Bishop's and Beasley's WISL thesis chapters): making glasses

by PVD is like playing Tetris (shown in Figure 8(b), (c)). PVD at fast deposition rates and low substrate temperatures is like playing with the difficult game settings: blocks (or atoms making up the glass) will fly down fast and you won't have enough time to orient them well enough to fit tightly. PVD at slow deposition rates and high substrate temperatures is like switching Tetris to the easy setting: you have enough time to reorient the blocks for efficient packing.

1.5 How are groups of atoms organized in a better packed glass?

In an earlier section, I talked about how controlling the deposition conditions can result in a better organized glass. But what tells us that the glass is indeed better organized? Glasses don't have discernible repeating atomic arrangements, but they certainly have small clusters or groups of atoms (size can be ~ 20 atoms) arranged in certain patterns. We can study the types of these atomic clusters by determining symmetries present in them. Regular polygons are polygons with all sides of equal length and are said to have rotational symmetry since they can be mapped onto themselves about a central point by less than a complete rotation as shown in Figure 9(c). For example, an equilateral triangle is a 3-sided polygon with equal lengths, thus showing 3-fold symmetry. More generally, where n is a number, an n-sided regular polygon is said to have n-fold symmetry and can be mapped onto itself by a rotation angle of 360°/n.

Figure 9*: Five-fold symmetries in (a) starfish [16] and (b) okra slices [17]. (c) compares existence of 6-fold rotational symmetry in a regular hexagon versus none in a scalene triangle [18].*

As glass scientists, we care a lot about promoting increased resistance to both, (1) crystallization when heated and (2) deformation: (1) indicates a glass that can survive against heating and (2) indicates a stronger glass. The key to a glass' response to external stimuli like heating or deformation resides in clusters or groups of atoms making up the glass. So, what are the different types of symmetries that exist in these atomic clusters and what can they tell us? A famous mathematical theorem called crystallographic restriction (based on observing many actual crystals) states that only regular shapes with 2-, 3-, 4- and 6-fold symmetries can completely fill up a plane's space (also called tiling a plane). These symmetries mostly make up crystals with long range repeating structure. On the other hand, 5-fold symmetry cannot efficiently tile a plane, leaving behind unfilled space. Then, 5-fold symmetry is incompatible with forming repeating patterns of atomic arrangements and cannot form a crystal (except in one class of materials called quasicrystals, but we will not talk about those here). Five-fold symmetry is all around us, like starfish or okra slices. Some previous experiments and simulations have attributed a higher 5-fold or "icosahedral" atomic clusters to metallic glass structure as the reason for increased resistance to crystallization and deformation both.

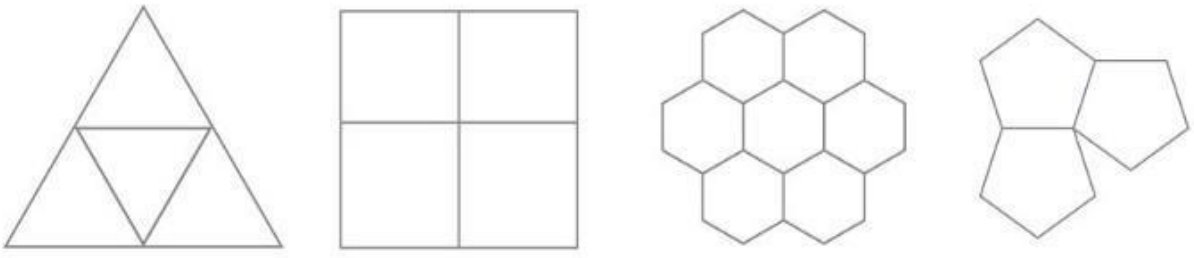

Figure 10*: 3, 4 and 6 sided tiling shapes fill all space perfectly while 5 sided shapes leave gaps [19].*

1.6 How do we study glass structure in the lab?

Once I made a new thin film material, I needed to find out what the structure was. To do that, we studied the glass structure by aiming either X-rays or high energy electron beams at our samples and detecting how they "diffract." Similar to light, X-rays and electron beams usually travel in straight lines, but upon encountering a barrier, they bend around it and become spread out. This phenomenon, called diffraction, occurs when X-rays or electron beams are bent around atoms that are nearly the same order of magnitude or bigger in size than the beams' wavelengths. An everyday example of diffraction (although from sunlight rather than X-rays or electron beams) is diffraction of sunlight by clouds, which we call silver lining (Figure 11(a)). Diffraction from X-rays and electrons helps us understand how far apart the atoms are. Lab-grade X-ray diffraction informs us as to whether our thin films are crystalline or glassy. Figure 11(b) shows the instrument's measurement geometry and Figure 12 shows example X-ray diffraction results on glassy and crystalline thin films. While the crystalline data shows well-defined sharp peaks, the glassy data represents a broad peak. The sharp peak means there are crystals with atoms spaced regularly at the corresponding distance. On the other hand, the amorphous sample indicates a range of distances for the interatomic spacing, highlighting its non-repeating atomic structure.

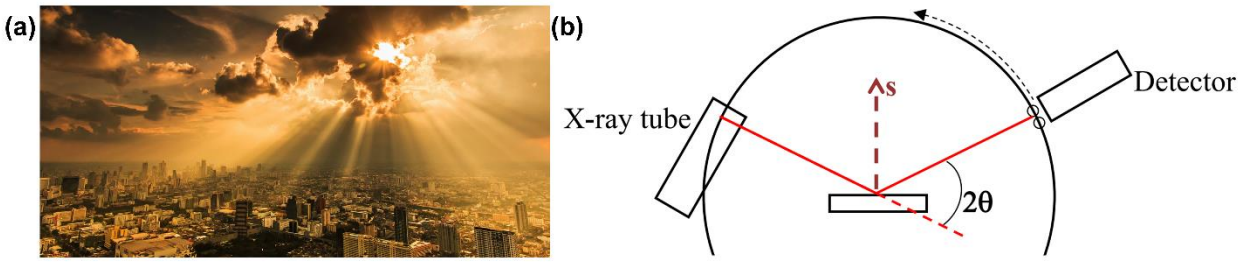

***Figure 11**: (a) Picture of silver lining [20]. (b) Schematic shows geometry of incident X-ray beam originating at the X-ray tube aimed at the sample and detector detects the diffracted beam intensity [21].*

While X-rays can tell us whether thin films are amorphous or crystalline, we need a much more sophisticated tool to perform something called electron beam diffraction so we can look at atomic clusters with five-fold and the other symmetries. We performed electron beam diffraction in a million-dollar machine called a scanning transmission electron microscope, shown in Figure 13(a). Figure 13(b) shows the measurement geometry of this technique. My colleague, Debaditya Chatterjee scanned a high energy, focused electron beam of a size ~10,000 times smaller than hair diameter (the same size as atomic cluster features we are looking for) across a sample and collected the diffraction signal resulting from transmission through the sample. Then, we analyzed this diffraction data to reveal dominant symmetries present in our atomic clusters.

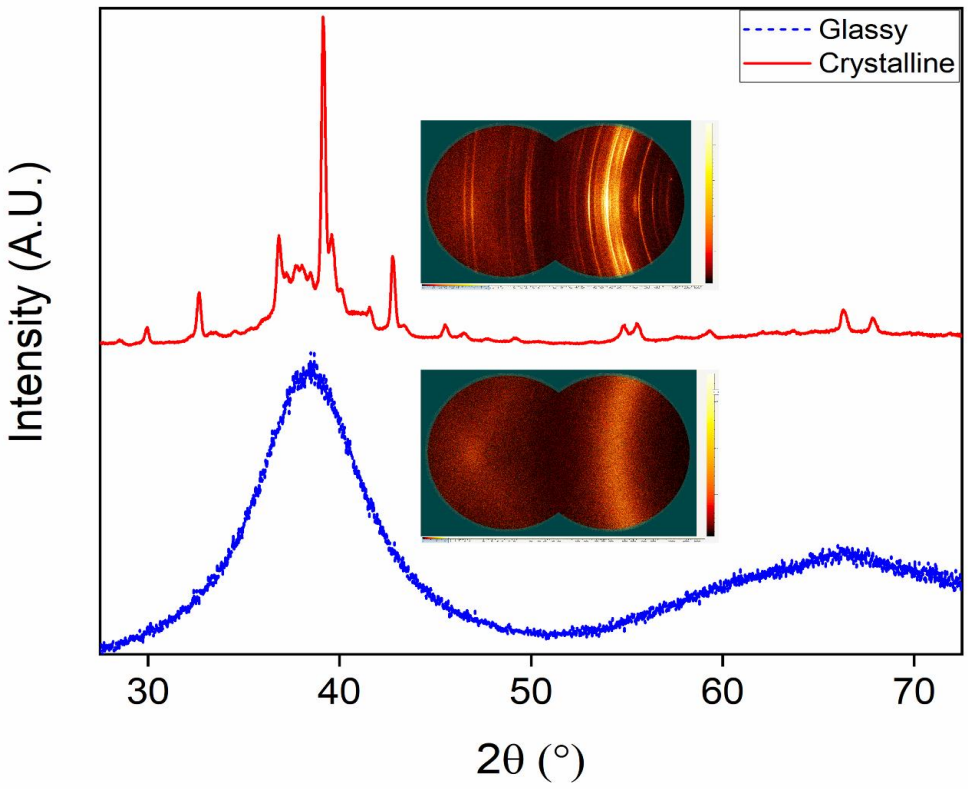

Figure 12*: The curves represent example results from X-ray diffraction on a glassy (blue dotted curve) and a crystalline (red solid curve) thin film while the insets show detector signal acquired by the instrument.*

1.7 My key results: shaking a martini of metal atoms to make harder glass

In this document, I want to focus on one main result from my experiments since I consider this piece of new knowledge I created very important to the glass community. Working together with a team of professors, other graduate students and postdocs, we discovered that slowing the deposition rate promotes the occurrence of "icosahedral-like" clusters (size ~20 atoms) in our metallic glasses, which makes their structure more resistant than fast-cooled glasses to breaking either by heating or mechanical deformation. Our work provides a novel understanding of the deposition conditions required to make harder glass (~4% harder than fast cooled glass) and connect the improved glass properties to a structural origin.

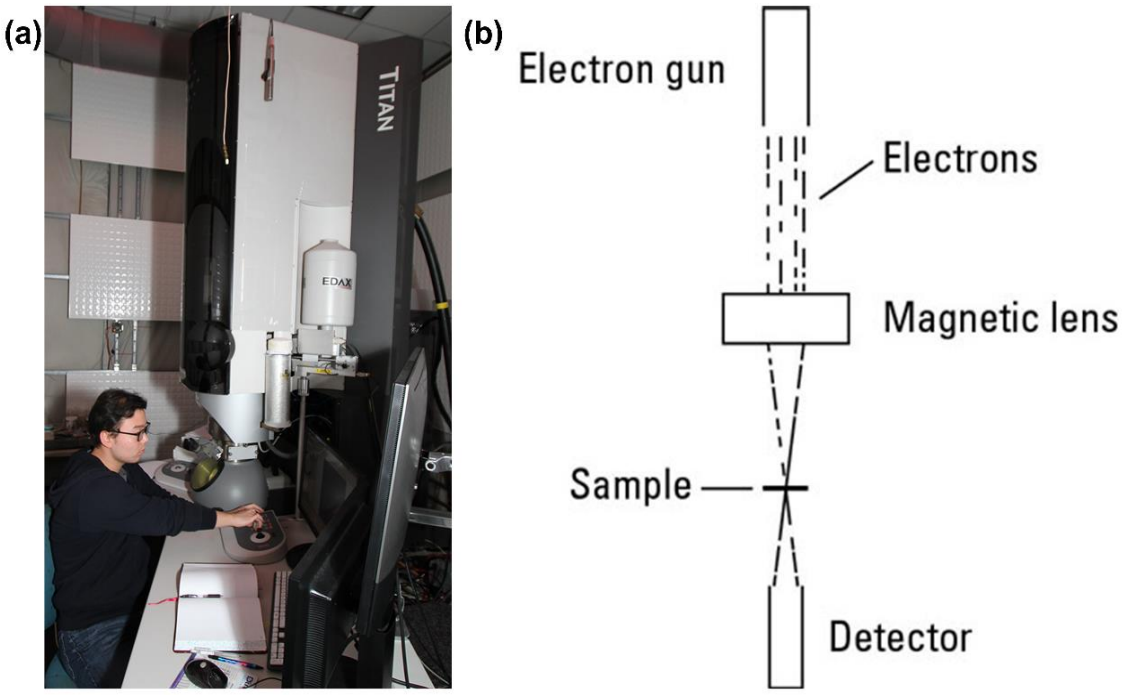

Figure 13*: (a) Picture shows my colleague, Dr. Chenyu Zhang driving the million-dollar microscope [22]. (b) Schematic shows geometry of electron diffraction measurements [23].*

1.8 Potential uses: great things come in small packages

My PhD thesis has focused on preparing and promoting 5-fold ordered atom clusters in metallic glass thin films. By virtue of the novel metallic glass states and resulting properties my work could achieve, we think our glasses could have applications in protection of interacting surfaces in relative motion such as gear assemblies (also called tribological applications in the engineering community), and mechanical barrier coatings. Particularly, we think our glasses show promise as hard coatings in biomedical devices like scalpels, needles, and implants. My favorite application was developed in Prof. Jinn P. Chu's group in Taiwan, shown in Figure 14: the team compared interactions of a surgical needle with pig tissue. For the bare needles and those coated with crystalline titanium and titanium nitride, the tissue stuck to the needles noticeably indicating damage as the needle was inserted and then retracted. Comparatively, the needle coated with thin film metallic glass by sputtering showed minimal tissue damage. The thin film metallic glass needle had a smooth surface and lesser friction, allowing it to easily pierce the skin and thus reduce the pain of receiving an injection. So, if vaccine syringes are made with these coatings, shots would hurt less.

1.9 Personal outlook

My stay in the United States so far has exposed me to academic research in university and national lab settings, and industrial research. As I wrap up my PhD thesis and look back at the last six years of my life, I see the truly immense professional and personal growth graduate school has afforded me. As an international student originally from India, I came to an unfamiliar country with just two full suitcases and frankly, didn't know what to expect. Now having spent five plus years at Madison and one year in Berkeley pursuing research, I understand the scientific process

much better and feel as much at home in the United States as I do in my home country. I want to acknowledge all the brilliant academic and industry mentors, colleagues and all my peers I had the pleasure of working with. Despite graduate school being full of ups and downs, I am deeply grateful for this opportunity since it allowed me to build lasting friendships, personal resolve, and grit. After my PhD, I will be starting as a Process Engineer at Intel Corporation, and I hope to leverage my hardware skills and fundamental understanding of physical phenomena, so I contribute to solving impactful problems. Nevertheless, no matter where I end up in the future, I endeavor to take with me the cultivated scientific attributes of rigorous inquiry and abject wonder.

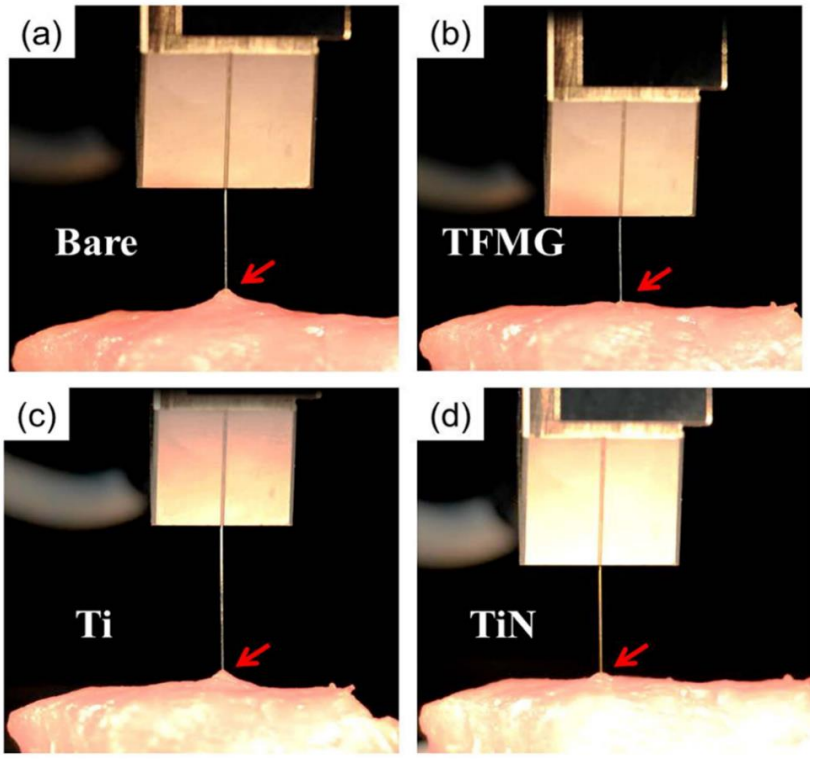

Figure 14*: Pictures of (a) bare, (b) metallic glass thin film-coated, (c) titanium-coated and (d) titanium nitride-coated needles during retraction from pork muscle. Arrows show needle does not stick to pork muscle in (b) but does so in (a), (c) and (d) [24].*

Chapter 2 Introduction

2.1 Motivation

The history of human civilization is replete with examples of technological breakthroughs like the printing press, electricity, telephones, automobiles, semiconductors, etc. that completely transformed quality of life. Enabling these inventions has been intimately linked to deploying diverse materials such as metals, glasses, ceramics and polymers. Just like these previous inventions, the discovery and design of new solid materials continue to drive modern technological advancements. Many pressing scientific problems currently faced by human society have their genesis in the limits of available materials and are expected to be solved by breakthroughs in materials science. The role of materials scientists is to develop an understanding of how processing history can manipulate material structure, which in turn is intrinsic to their properties and performance.

Relating observed structure-properties to processing is called the materials paradigm, commonly represented by the tetrahedron in Figure 15. In a nutshell, the constituent elements' physical and chemical interactions are the major determinants of material structure and can be altered by processing. Taken together, these characteristics are related by the laws of kinetics and thermodynamics and dictate material properties. The framework afforded by materials paradigm is an exceptionally powerful tool, whether to advance understanding in a variety of research areas or as means for failure analysis of products which fail or do not perform as required resulting in injury or monetary losses. This thesis invokes principles of materials paradigm to

(1) manipulate metallic glass' thermal stability by vapor deposition route and identify the structural origin for these changes (chapter 4),

(2) create a data library of processing-structure-property relationships in vapor deposited amorphous carbon thin films for industrial applications (chapter 5), and

(3) investigate failure mechanism of copper weld wheels in an industrial manufacturing set-up which did not function as intended (chapter 6).

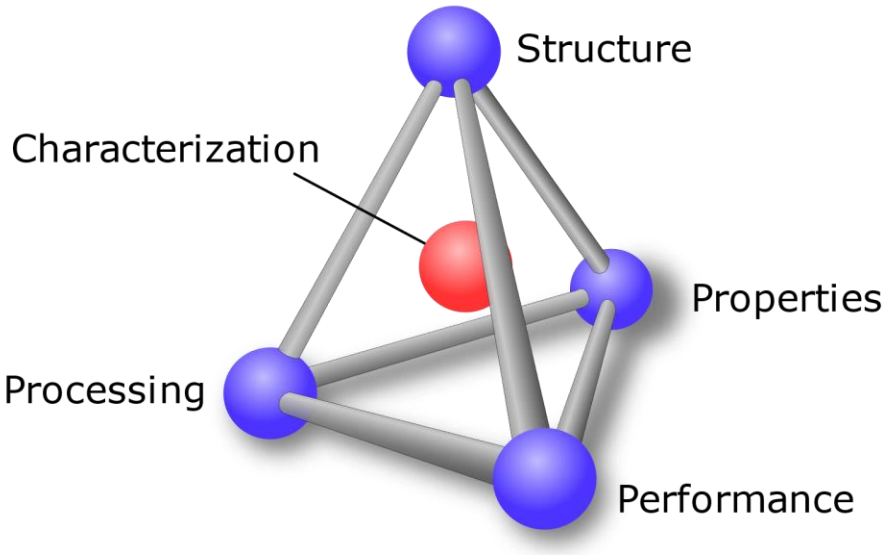

Figure 15*: Materials paradigm represented as a tetrahedron is shown* [25].

2.2 Plasma-based thin film deposition techniques: background

Plasma-based deposition technologies are critical to miniaturization and enable modern inventions spanning applications in semiconductor manufacturing, energy storage, microfabrication, superconductors, etc. Gas-phase plasmas contain significant percentage of ionized atoms and molecules with fractional ionization spanning from 10^{-4} in common capacitive discharges to ~ 5 – 10 % in high density inductive plasmas. Plasmas used for material processing are operated in the pressure range from a few millitorr to a few torr, although arc discharges and inductive plasmas can still work at atmospheric pressure. The goal of plasma-based deposition is

to controllably transfer atoms from the source material to a substrate which provides a base for film formation and growth to happen atomistically [26].

Materials' fabrication with desired functionality by plasma-based deposition requires some background on the key concepts of plasma generation. Commonly, a plasma called glow discharge is formed by passing electric current through a gas. Glow discharges can be struck by applying voltage across two electrodes in a glass tube containing low-pressure gas [27]. For the gas ionization to become self-sustaining, the voltage value should exceed a certain "striking voltage". The low gas pressure facilitates an increase in mean free path, meaning a longer mean free path allows a charged particle to attain more energy before striking another particle for a fixed electric field. Initially, a small fraction of gas atoms is ionized by random thermal collisions between atoms. The applied electric potential drives the positive ions towards the cathode and the electrons towards the anode. This motion of initial population of ionized species results in interactions with other atoms, thereby ionizing them and sustaining the plasma. Also, the concept of secondary emissions is an important one: some of the gas ions' energy is transferred to the cathode in two forms. Primarily, ions transfer momentum to the more numerous neutral gas atoms, which in turn strike the cathode. Also, some of the ions strike the cathode directly. However, irrespective of which species strike the cathode, internal collisions redistribute this transferred energy within the cathode and emit electrons, which are then accelerated into the bulk of the glow discharge. This process is called secondary electron emission.

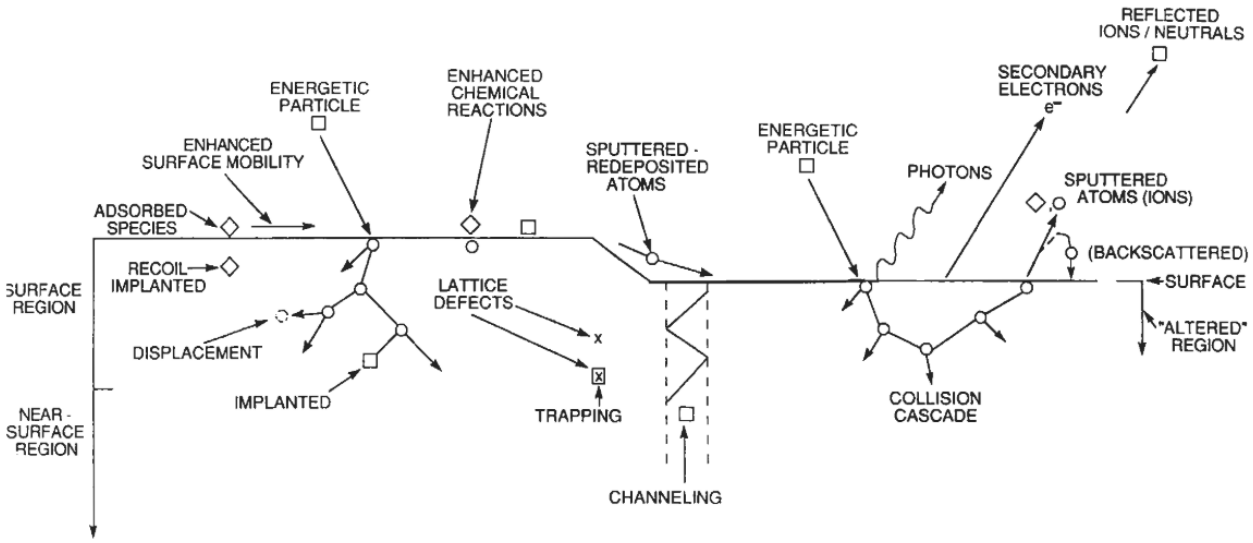

Figure 16*: Schematic depicts a summary of collision and transport processes at the growing surface and plasma-cathode interactions* [26].

The choice of type and pressure of process gas and harnessing electric and magnetic fields is critical to achieve optimal plasma properties, which can then enable thin film growth with desired characteristics. Either of direct current or alternating current plasma technology can enable both physical and chemical vapor deposition. For example, instead of only secondary electron emissions, positive ions can be sufficiently energized to eject out neutral cathodic atoms through momentum transfer by a process called sputtering [26]. Striking a high current, low voltage arc at a cathode surface can cause a micrometers-wide mobile, highly energetic emitting area called cathode spot. This is an arc evaporation technique called cathodic arc deposition [28]. Condensation by chemical reactions from gas phase to solid phase on a substrate can be aided by plasma discharge in a process called plasma-enhanced chemical vapor deposition [29]. Figure 16 provides a summary of the numerous fundamental processes happening at film and cathode surfaces.

2.3 Background on metallic glass thin films

Amorphous metallic alloys, also known as metallic glasses (MGs) are a class of materials characterized by amorphous structure without long-range atomic periodicity. Perhaps one of the most important distinguishing features of MGs is the glass transition phenomenon, as shown in Figure 17(a). The noncrystalline state is retained if the supercooled liquid can be quenched sufficiently fast to suppress formation of crystalline phases [30]. Ever since the first MG was synthesized in 1960 [31], these class of materials have been a subject of scientific interest due to their many exceptional properties: excellent mechanical properties of high specific strength, large elastic modulus, high resistance to corrosion and wear, and good soft magnetic properties. However, the atomic-level descriptions for glassy systems and their non-equilibrium thermodynamics hinder our understanding of fundamental glass physics and chemistry [32]. A pursuit for this understanding will not only transform an empirical discipline to one built upon rigorous scientific principles, but also aid atomic-level design of glasses.

Glassy structure retains information about its processing history. Therefore, it is insightful to think of glasses in the context of a potential energy landscape – a complex multidimensional surface composed of basins of different widths and depths [33,34]. Figure 17(b) illustrates such a landscape. In this landscape, while a liquid at equilibrium is constantly sampling different regions, a glass on the other hand is trapped in a basin. The height of this basin relates with the glass' properties. The lowest basin corresponds to a strongly cohesive glass with high thermal stability. When cooling a liquid to form glass, the glass will be trapped in a higher basin for a faster cooling rate (structural rejuvenation) and will correlate with inferior modulus properties. On the other hand, with processing such as annealing or aging, the amorphous configuration will be trapped at

lower configurational potential energy corresponding to improved modulus and yield strength. Until recently, liquids cooled at the slowest experimentally possible cooling rate formed glasses that were trapped in relatively higher basins.

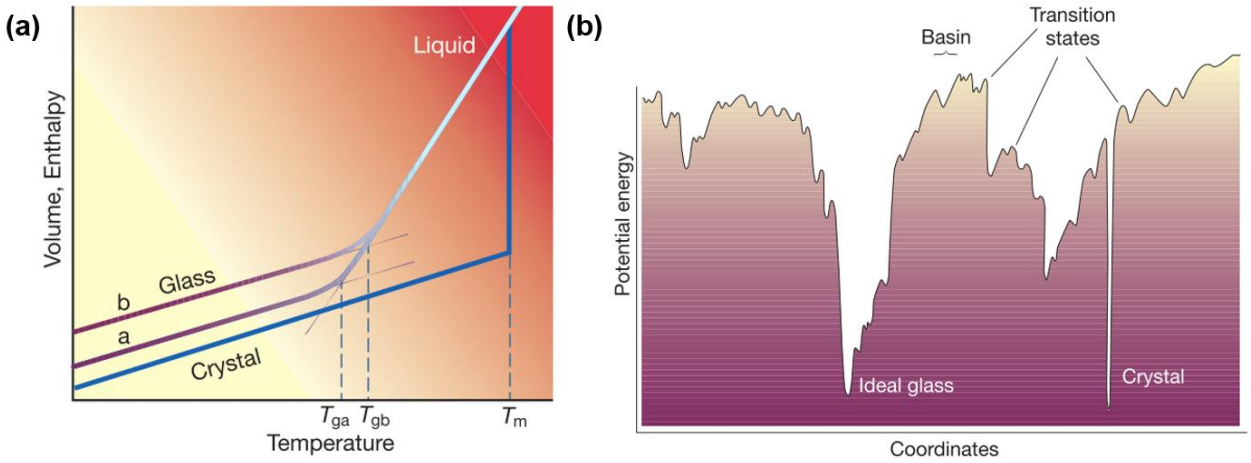

Figure 17*: (a) The dependence of volume/enthalpy at constant volume on temperature for a liquid is shown.* T_m *is the melting temperature and* T_{ga} *and* T_{gb} *are glass transition temperatures of glasses a (slower cooled) and b (faster cooled) respectively. (b) Schematic illustration of a potential energy landscape is shown* [34].

To sample the deep basins, fabrication by physical vapor deposition (PVD) onto substrate heated to 0.85 T_{onset} (temperature at which glass begins to transition into supercooled liquid upon heating) resulted in glassy films with thermodynamic and kinetic stability equivalent to aging ordinary glasses for millennia in molecular glasses [35–37]. These glasses were termed ultrastable glasses. A combination of longer surface residence time on account of low deposition rate and high surface diffusivity allow for the surface liquid layer to explore many possible configurations to find a local minimum on the potential energy landscape. Figure 18 shows enthalpy measurements on 1,3-bis-(1-naphthyl)-5-(2-naphthyl) benzene (TNB) and indomethacin (IMC) via calorimetry measurements. The vapor-deposited samples of TNB and IMC fabricated in a few

hours demonstrated higher T_{onset} than ordinary glasses aged below T_{onset} for several days. A higher T_{onset} value corresponds to better kinetic stability because higher temperature is required to dislodge atoms from glassy configuration. Also, for these glasses, the fictive temperatures T_f and integrated enthalpies were lower for vapor deposited TNB and IMC as compared to their respective ordinary glasses. This indicates better thermodynamic stability of vapor-deposited samples. These results motivated efforts to create and study ultrastable glasses in other materials' systems including metallic [38,39], polymer [40] and chalcogenide [41] glasses.

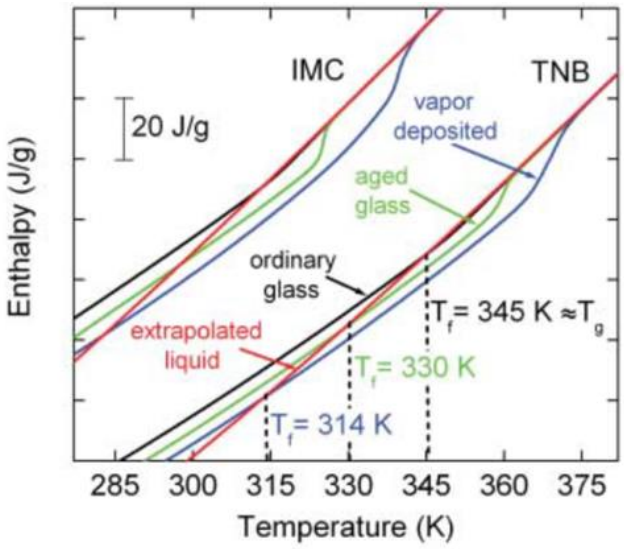

***Figure 18**: Ultrastable glasses have lower enthalpy and higher T_{onset} than ordinary glasses* [35].

Lack of thermal stability poses a paramount difficulty to develop MGs for wide applications. Previous studies to enhance stability in metallic glass thin films with PVD have resulted in intriguing but conflicting observations. Notably, deposition rate [38,42] and substrate temperature [39,43–46] seem to be the most important controlling parameters as shown in Figure 19. Applying ion-beam assisted deposition (IBAD) to access very low deposition rates, Luo et al. [38] and Liu et al. [42] demonstrated that decreasing the deposition rate by only one order of

magnitude resulted in large increase in kinetic stability of deposited films as compared to liquid-quenched glass, but neither reported thermodynamic stability. Yu *et al.* [39] reported higher kinetic stability but lower thermodynamic stability in sputtered $Zr_{65}Cu_{27.5}Al_{7.5}$ at a deposition temperature of $0.8T_{onset}$. For comparison, Aji *et al.* [43] showed both higher kinetic and thermodynamic stabilities at a deposition temperature of $0.8T_{onset}$ in sputtered $Zr_{55}Cu_{30}Ni_5Al_{10}$. In sputtered $Pd_{77.5}Cu_6Si_{16.5}$, Magagnosc *et al.* [44] discovered that the mechanical properties as a function of deposition temperature peaked at $0.73T_{onset}$, which they argue is evidence of better thermodynamic stability. Liu et al. [45] observed higher elastic modulus (suggesting densification and improved thermodynamic stability) but reduced kinetic stability with increasing deposition temperature in Zr-Cu-Ni-Al-Hf-Ti films. For a Zr-Cu-Ni-Al system, Chu et al. [46] showed improved hardness and elastic modulus with increasing substrate temperature, but kinetic stability for all films was nearly the same. In summary, PVD clearly seems to be an effective method to explore a wide spectra of glass structure and establish structure-property relationships. So far, the relationships between synthesis parameters, formation mechanisms and stabilities are unclear.

The quest to manipulate glass stability in a consistent way seems to rest upon a competition between kinetic film growth and thermodynamic film crystallization. While melt-quenched metallic glasses can explore a relatively limited number of configurations due to constrained structure relaxation from neighboring atoms, metallic glasses grown by vapor deposition are expected to sample a much larger subset of glass structures due to ultrafast surface dynamics. Yang et al. [47] deduced surface diffusivity to bulk diffusivity (D_s/D_b) ratios of ~ 10^8-10^{11} for metal films grown at 0.3-0.5 times T_m. Surface self-diffusion measurements in an ultrastable molecular glass [48] and a model metallic glass system [49] have suggested that surface diffusivity is 5-8

orders of magnitude faster than bulk diffusivity near T_{onset} and the activation barrier to surface hops is half of that for bulk rearrangements.

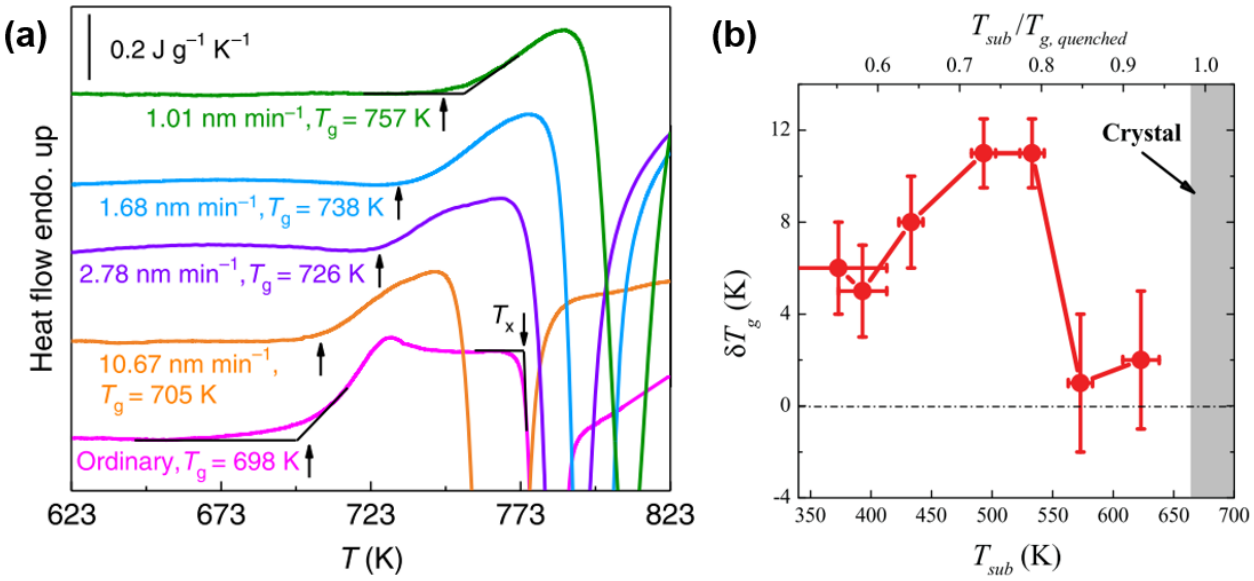

***Figure 19**: Increase in kinetic stability of vapor deposited Zr-Cu-Al MGs due to optimal (a) deposition rate [38] and (b) substrate temperature [39] are shown.*

Optimizing for high residence time and surface diffusivity while avoiding crystallization seems to be the key recipe to producing metallic glasses with exceptional thermodynamic and kinetic stabilities. Kinetically, the island nucleation rate n on a growing film surface is given by: $n \sim D(\rho h)^2$ where D is the diffusion constant, ρ is the surface atomic density and h is the film thickness [50]. For the case of constant h, a high n would be facilitated by high D and ρ which in turn, would be enabled physically by high substrate temperatures and low deposition rates respectively. High kinetic stability corresponds with high n [51]. Thermodynamically, the melting temperature T_m for an ideal infinitely large crystal film is given by: $T_m = T_{m,bulk}\left(1 - \frac{2\gamma_f}{\rho h \Delta H_f}\right)$, where ΔH_f is the enthalpy of fusion and γ_f is the film surface energy [52]. T_m would increase with

increasing ρ (decreasing deposition rate) and tend to $T_{m,bulk}$ at an infinitesimally slow deposition rate. This means slowing the deposition rate increases the propensity to crystallize.

Vapor-deposited MGs with varying stabilities are ideal candidates to explore a wide spectra of glass structure and establish structure-property relationships. Presumably, excess surface diffusivity means the ultrastable glass has better packing leading to lesser fraction of free volume and an overall densification of the structure [35]. This idea was supported by simulations for vapor-deposited Zr-Cu-Al glass films which predicted high substrate temperature (0.625 T_{onset}) contributed to structural densification and improved chemical order [53]. Previous molecular dynamics (MD) simulations have recognized solute-centered nearest neighbors as the primary building blocks of MG structure [54]. Short range order (SRO) is dominated by icosahedral ordering with fivefold symmetry in certain MG systems such as Zr-Cu [55] and Zr-Cu-Al [56,57].

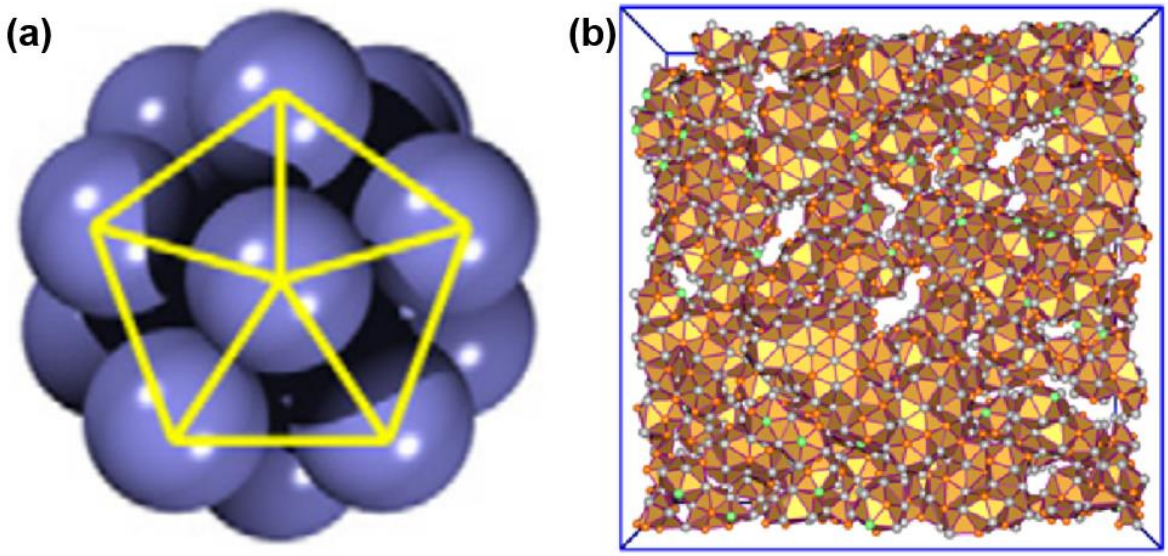

Figure 20*: (a) Fivefold symmetry in icosahedron shown by a hard spheres model* [56] *and (b) snapshot of molecular dynamics simulation of Zr (grey), Cu (orange) and Al (green) showing medium-range interconnectivity degree in a Zr-Cu-Al MG* [57].

Medium-range order (MRO) occupies the length scale between short and long-range order and can be considered as interconnected SRO. A higher icosahedral contribution to MG structure results in slow structural relaxations [58], resistance to local transitions, increase in heat capacity and elevation of barrier to crystallization [59,60]. However, the inherent disordered arrangement of atoms poses a unique challenge to experimentally characterize glass structure. The atom pair correlation functions (PCF) measured by conventional diffraction methods are insensitive beyond short range [61] meaning many qualitatively different MRO structures can have indistinguishable PCFs. While Yu et al. [62] suspected only differences in distributions of local clusters to explain ultrastability based on simulations, Luo et al. [38] reported a relatively more homogeneous glass structure in ultrastable glass from high-angle annular dark field scanning transmission TEM (HAADF-STEM) and Aji et al. [43] found enhanced MRO of size ~1-2 nm in ultrastable glass originating from chemical clustering as measured by a combination of HAADF-STEM and angstrom beam electron diffraction (ABED). A clear consensus on structural origin of glass stability has evaded us thus far and points towards an urgent need to employ novel structural characterization techniques.

2.4 Amorphous carbon thin films for industrial applications

Hydrogenated amorphous carbon (a:C-H) is a metastable, allotropic carbon-based material. It is made up of three-fold sp^2- and four-fold sp^3-hybridized carbon (< 50 %) in an amorphous matrix [63]. a:C-H thin films enhance mechanical, wear and chemical performance characteristics of substrates [63–66], leading to uses in a range of applications with numerous materials requirements. Examples include x-ray detection devices, implantable medical devices [67], cutting and drilling tools [68], and magnetic discs [69]. a:C-H coatings can be prepared by various thin

film deposition methods such as sputtering [70], ion beam assisted deposition [71], cathodic arc deposition [72], plasma enhanced chemical vapor deposition [73] and pulsed laser deposition [74]. However, applying a:C-H thin films to substrates requires optimizing several surface properties while contending against tradeoffs with other performance characteristics. An optimal blend of low coefficient of friction, high hardness, wear resistance, elasticity, and adhesion are invaluable for many products but is hard to attain.

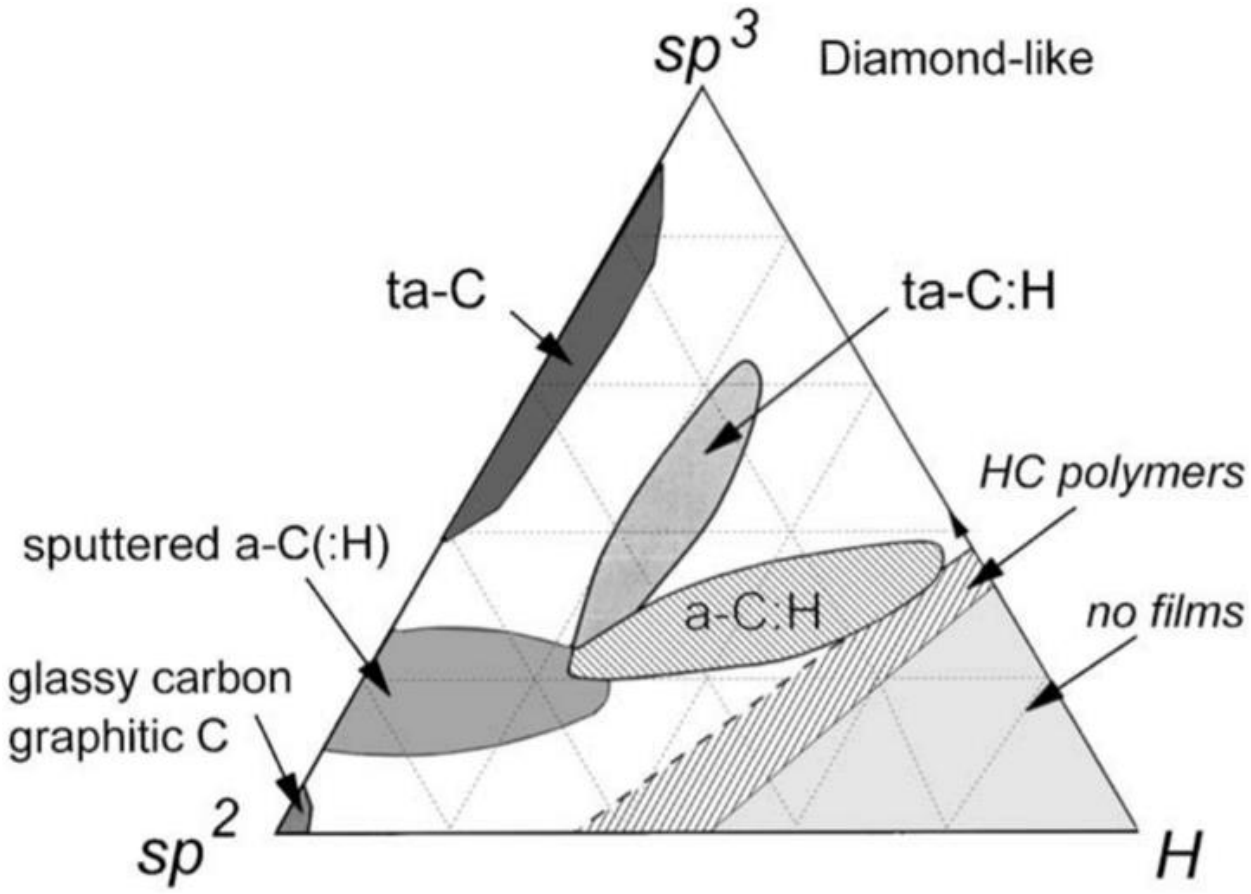

Figure 21*: Ternary phase diagram of bonding in amorphous carbon-hydrogen materials is shown* [63].

Four-fold sp^3 bonding controlled by ion energy during deposition results in many useful properties of amorphous carbon films including high hardness and low wear rates [75]. The highest

sp^3 fraction can be achieved by tuning C^+ ion energy to 100 eV [76]. However, maximizing sp^3 bond contribution to film structure was observed to coincide with undesirably high compressive film stresses (> 9 GPa), which limit the film thicknesses to ~ 100 nm before delamination happens [77]. Previous work discovered methods to reduce or eliminate intrinsic stress including substrate biasing during deposition [78], post deposition annealing [79] and multilayering [80,81]. Amongst these techniques, while substrate biasing could substantially reduce intrinsic stress (0.5 GPa from 9 GPa), a concurrent decrease in sp^3 content lowered the hardness dramatically (26 GPa from 85 GPa). Post deposition annealing eliminated the stress without altering film structure but needed additional multiple cycles of thin film growth and annealing to substantially thicken the adherent coating. In contrast, multilayering alternate soft and hard layers enhanced coating adhesion to substrates together with an overall low compressive stress and acceptable mechanical performance. Therefore, previous research implies industry can tailor these methodologies to make desired multilayered coatings in a single-step process for large scale production.

The incorporated hydrogen satisfies existing surface covalent or free-bonds for a:C-H films. This greatly enhances friction behavior, but mechanical properties worsen on account of hydrogen loss induced by annealing and doping. Another form of amorphous carbon films were fabricated by combining PECVD growth and insitu annealing. These films had high electrical and thermal conductivities due to big fullerene-like sp^2 clusters [82,83]. But delamination happened due to high intrinsic compressive stress and plasma-based overheating. Alternatively, a discontinuous and periodical discharged plasma environment formed fullerene structures due to film annealing while the plasma was not discharging [84]. Driven by thermodynamics, a variety of fullerene structures could be made from diverse precursors like amorphous carbon and

nanodiamonds at optimal annealing conditions [85]. This novel nanostructure made up of hydrogen-free fullerene has curved and interlocked graphitic planes with the ability to propagate the high strength of a planar sp^2-coordinated carbon network into three dimensions. Consequently, the films show large elasticity with an unprecedented elastic recovery of 85% together with high hardness up to 55 GPa [86].

2.5 Thesis outline

Chapter 3 introduces the common experimental techniques used in this work for deposition and materials characterization. Chapter 4 presents results on controlling kinetic stability of sputtered Zr-Cu-Al thin films with deposition rate and compares the structural nanoscale ordering between glasses with different stabilities. Chapter 5 reports structure-property correlations in single-layered and multi-layered amorphous carbon thin films. Chapter 6 evaluates a case study on significantly lower lifetime of upper copper weld wheels in an industrial mash seam welding setup. Finally, chapter 7 summarizes conclusions and suggestions for future work.

Chapter 3 Experimental Details

This chapter summarizes common experimental techniques used for all later work in chapters 4 and 5, namely the thin film deposition techniques, x-ray diffraction (XRD), scanning electron microscopy (SEM), energy dispersive spectroscopy (EDS), electron probe microanalysis (EPMA), atomic force microscopy (AFM), flash differential scanning calorimetry (f-DSC), fluctuation electron microscopy (FEM) and nanoindentation.

3.1 Thin film deposition of Zr-based glass forming alloys and amorphous carbon

3.1.1 Substrate preparation

To sputter-deposit Zr-based 100 – 600 nm thick films, 001-oriented Si wafers coated with 50 and 200 nm-thick chemical vapor deposited amorphous Si_3N_4 were used as substrates. 2 cm × 2 cm pieces cleaved from a bigger wafer were sonicated sequentially in acetone, isopropyl alcohol, methanol and deionized water for 5 minutes each. Then, the substrates were blow dried with dry nitrogen and mounted onto alumina plate by applying and curing a thin layer of either carbon paste or silver paint for good thermal contact (appendix A covers the procedure steps in detail). After curing, the substrate + alumina plate assembly was mounted inside the vacuum chamber. Samples for FEM studies were grown on 15-nm thick electron transparent amorphous Si_3N_4 windows, pre-cleaned with an Ar + O_2 gas-based plasma at 20 psi for 10 minutes. Bulk metallic glass ribbons of Zr-Cu-Al composition for nanoindentation studies were made by melt-spinning technique by our collaborator, Dr. Ye Shen. Prior to deposition of amorphous carbon films on 001-oriented Si wafer, the chamber was pumped to 2 mTorr, and the substrates were cleaned by Ar plasma for 15 minutes at pressure of 30 mTorr, D.C. pulse of 5.0 kV, 5kHz, and 10 µs.

3.1.2 Magnetron sputter deposition of Zr-based alloy thin films

We employed direct current (DC) magnetron sputtering for depositing alloy thin films. Sputter deposition is a physical vapor deposition technique that causes ejection of 'target' atoms by bombardment with highly energetic ions [26]. In the presence of a process gas such as argon, magnetron sputter sources employ strong electric and magnetic fields to ionize and confine charged plasma particles near target surface. Due to magnetic field generated by a permanent magnet, electrons follow a helical path along magnetic lines. This results in greater number of ionizing collisions near target surface than would otherwise occur. The efficiency of the initial ionization process and stable plasma at lower gas pressures result from the closed magnetic field. Sputter deposition parameters need to be optimized to grow thin films with desired characteristics.

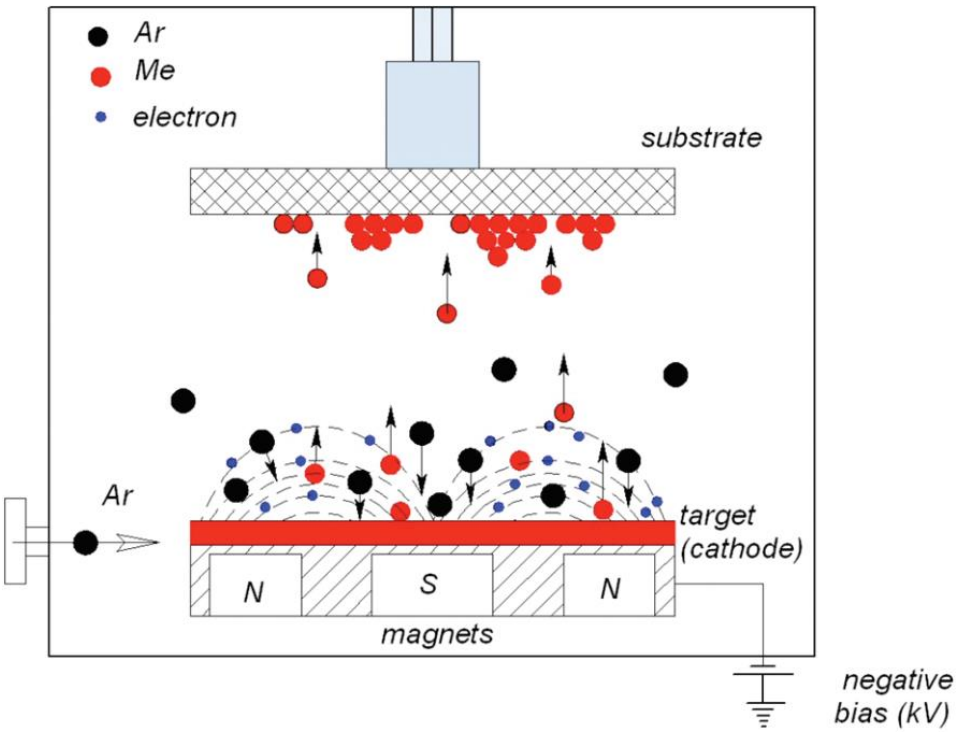

***Figure 22**: Schematic of DC magnetron sputtering* [87]. *Me is the metal used as target and N and S represent north and south poles.*

We chose two known Zr-based good glass forming systems known to show ultrastability [39,43] for our studies. Zr-based thin films were deposited by employing an in-house built high vacuum DC magnetron sputtering tool. Arc-melted alloy targets with nominal composition of $Zr_{65}Cu_{27.5}Al_{7.5}$ and $Zr_{55}Cu_{30}Al_{10}Ni_5$ (at. %) were purchased from Haohai Metal Materials Co. Ltd., China and ACI Alloys Inc., United States. The base pressure of the vacuum vessel was better than 5×10^{-8} Torr with partial pressures of oxygen of 2×10^{-10} Torr and water vapor of 5×10^{-9} Torr as measured by a SRS 100 residual gas analyzer. Before running every deposition, the substrate temperature was calibrated against the heater voltage (V) – current (I) characteristics and filament temperature. During the actual deposition, the substrate temperature was assumed to be the same as calibration while carefully maintaining the same filament temperature and V – I characteristics. The target power was cautiously ramped up to avoid shocking the targets, and pre-sputtering for ~ 1 minute was practiced to remove surface oxide and allow the vapor to achieve steady-state composition. The operating pressure of Ar process gas was 5 and 2 mTorr during deposition of $Zr_{65}Cu_{27.5}Al_{7.5}$ and $Zr_{55}Cu_{30}Al_{10}Ni_5$ respectively as measured by KJLC 275i convectron gauge. A range of thin films were grown at deposition rates from 0.19 nm/s to 1.91 nm/s and substrate temperatures from 300 K to 573 K. 100 – 650 nm thick films were grown for XRD, SEM, EDS, EPMA, AFM and nanoindentation studies Approximately 20 nm thick films were grown on electron transparent 15 nm thick Si_3N_4 membranes for FEM studies.

3.1.3 Deposition of amorphous carbon thin films

Single-layered and multi-layered diamond-like carbon thin films were deposited on single crystalline silicon substrates (mechanical grade, single side polished, thickness of 500μm) by NCD Technologies, with a custom-developed plasma immersion ion implantation (PIII)-based plasma

enhanced chemical vapor deposition (PECVD) set-up, represented in Figure 23. PECVD proceeds by introduction of reactant precursor gases between parallel electrodes – an electrically energized electrode (either direct current or radio frequency) and another grounded one which holds the substrate. The precursor gases are ignited to a plasma state due to capacitive coupling of the electrodes, thereby inducing a chemical reaction and subsequent deposition at the substrate. PECVD can produce an array of dense films adherent to different substrates [88]. The deposition process can be aided further by PIII, meaning negatively biasing the substrate to attract energetic positive ions and creating more energetic surface condensation. The influence of ion irradiation on the deposition process was shown to alter film properties such as hardness, surface roughness and optical transmission [89].

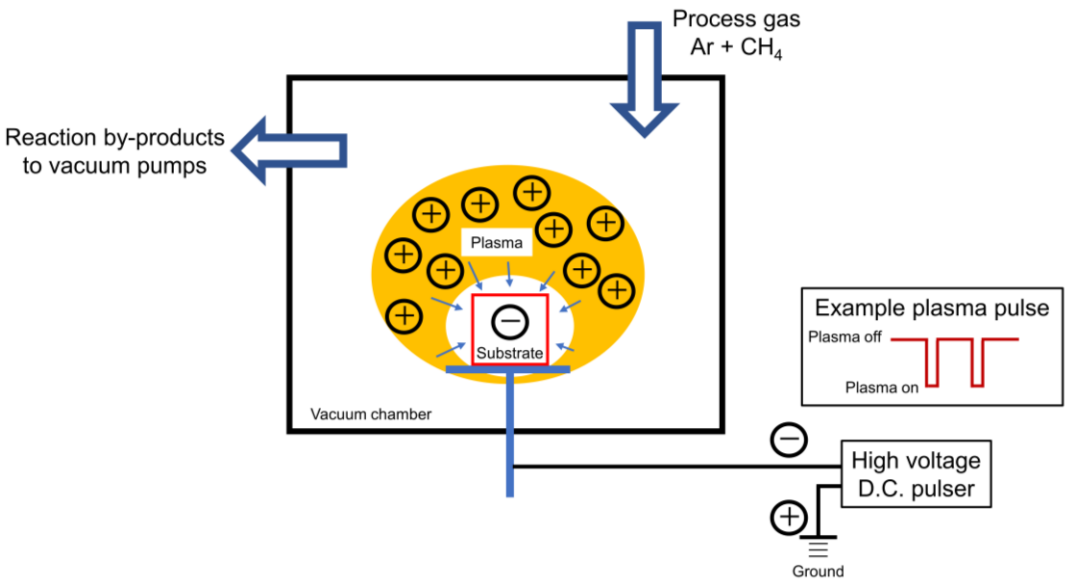

***Figure 23**: A simple schematic representing the PIII-based PECVD process and the inset shows example pulse characteristics.*

The plasma energy was controlled by a D.C pulser (Applied Energetics). A mixture of Ar + CH_4 was used as the process gas. Prior to deposition, the chamber was pumped to 2 mTorr. The DLC deposition pressure was 150 mTorr. For every deposition, 4 pieces of Si squares (10 mm × 10 mm) were equally spaced on the copper sample stage of Φ65mm on which the D.C. pulse was applied. As a first step, single-layered thin films were made to systematically study the effect of three parameters: applied D.C. voltage, pulse width and frequency. In order to study the effect of applied D.C. voltage, the deposition voltage was varied from 1.02 kV to 6.11 kV at a duty cycle of 5.5 μs and frequency of 5.0 kHz. In the study of pulse width effect, the pulse width was spanned from 2.0 μs to 25.0 μs at a voltage of 2.5 kV and frequency of 5.0 kHz, while the frequency ranged from 1.0 kHz to 16.0 kHz, at pulse width of 5.5 μs and voltage of 2.5 kV for the study of frequency. Two sets of 800 nm thick multilayered recipes (total of seven samples) were prepared: (1) three samples with alternating interlayers of 10 nm grown at 1.02 kV and 10, 20 and 30 nm grown at 1.94 kV, one sample with alternating interlayers of 20 nm, each grown at 1.02 kV and 1.94 kV, and (2) three samples with alternating layers of 10 nm grown at 6.11 kV and 10, 20 and 30 nm grown at 1.94 kV. For all the multilayered samples, the pulse width and frequency were set at 5.5 μs and 5.0 kHz respectively.

3.2 Materials characterization of Zr-based alloy thin films

A standard suite of characterization techniques was to screen the grown thin films and melt-spun ribbons of same nominal compositions as alloy targets. These were performed by myself and Debaditya Chatterjee.

3.2.1 X-ray diffraction

The thin film and ribbon samples were screened for amorphicity using a Bruker D8 Discover X-ray diffractometer using coupled Θ-2Θ scanning mode. This technique primarily relies on interactions between x-ray photons originating in the instrument and atomic electrons from the samples [90]. Upon collision, incident x-ray photons are deflected and some of these will not lose any energy from a process called elastic scattering. The x-ray instrument detects these scattered x-rays which carry information about electron distribution in the sample. Diffracted signal from different atoms interfere and the resulting intensity is strongly controlled by their interactions. For instance, in crystals with periodically arranged atoms, a sharp intense peak corresponding to a characteristic atomic distance will show up in the diffraction pattern, as shown in Figure 24(a). The condition for a diffraction peak to occur is governed by Bragg's law, $2dsin\theta = n\lambda$, where d is the interplanar distance, θ is the diffracting angle, n is an integer and λ is the wavelength of incident x-rays. While the x-ray instrument can be run in numerous settings, we employed coupled Θ-2Θ scanning mode (Figure 24(b)) to quickly screen the samples for amorphicity. The x-ray diffractometer uses Cu-K_α source and is equipped with an area detector for fast scans, such as shown in Figure 25 (inset). The two-dimensional plot of observed intensity versus scanned 2Θ angles (Figure 25) shows a broad hump for amorphous films and sharp peaks for crystalline films, indicative of interatomic distances making up short-range order.

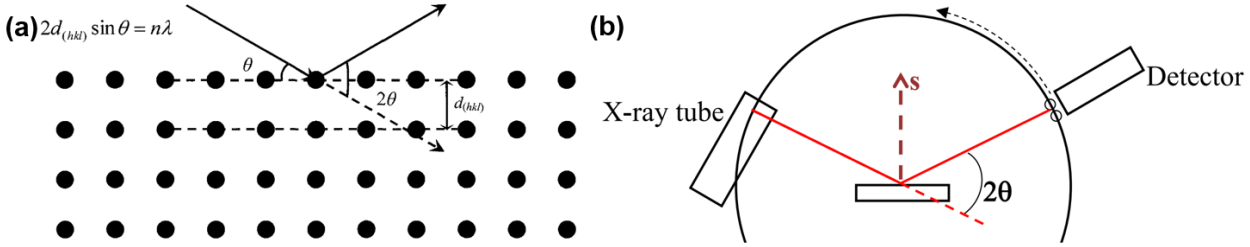

***Figure 24**: Illustrations of (a) x-ray diffraction based on Bragg's law* [91] *and (b) Θ-2Θ geometry [21] are shown.*

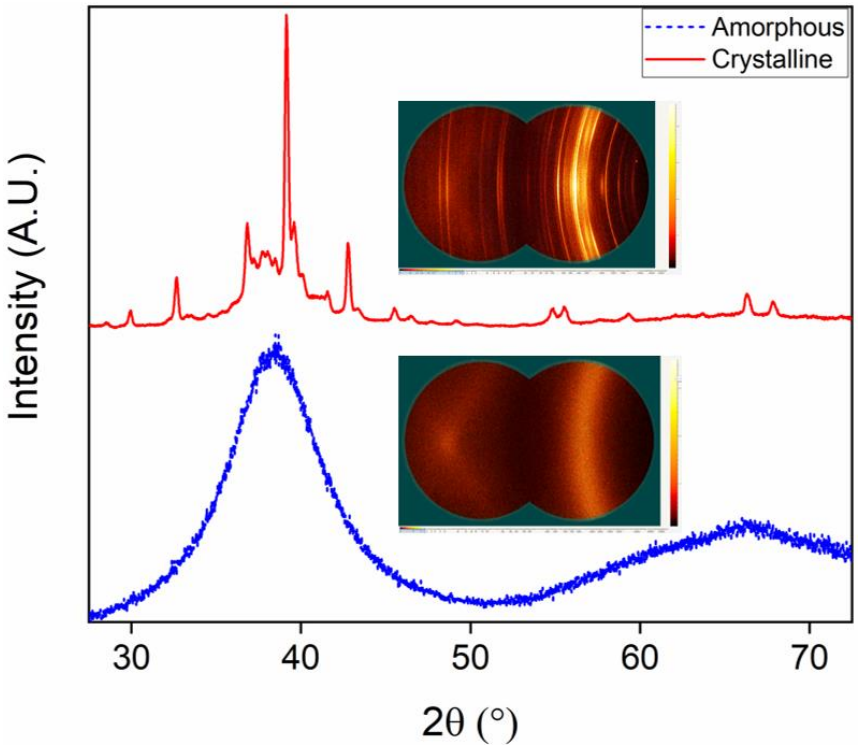

***Figure 25**: Example XRD patterns of amorphous and crystalline Zr-Cu-Al-Ni films are shown along with the instrument's 2D detector signal (inset).*

3.2.2 Scanning electron microscopy and energy dispersive x-ray spectrometry

A scanning electron microscope can image samples by scanning the surface with an electron beam generated inside an "electron gun" thermionically (typical accelerating voltage 1 – 30 kV and magnification of 10 – 3000000 times). Due to the beam-sample interactions, a range of

different signals containing information about the surface topography and composition are produced, as shown in Figure 26(a). Combining raster scans of the electron beam and the detected signal intensity, an image is produced. The most common imaging method relies on detection of low energy, secondary electrons (SE) which originate near the surface (first few nanometers) [92]. These SEs are ejected from conduction bands of the sample atoms due to inelastic beam-atom interactions and detected by an Everhart-Thornley detector [93]. We used a Zeiss LEO-1530 field emission scanning electron microscope (FESEM) to observe morphology of grown thin films at different magnifications and a gun energy of 3 kV. The samples were cleaved and their cross-section was studied to reveal thickness and fracture morphology at a gun energy of 3 – 10 kV. Dividing the thickness by deposition time gave an estimated deposition rate.

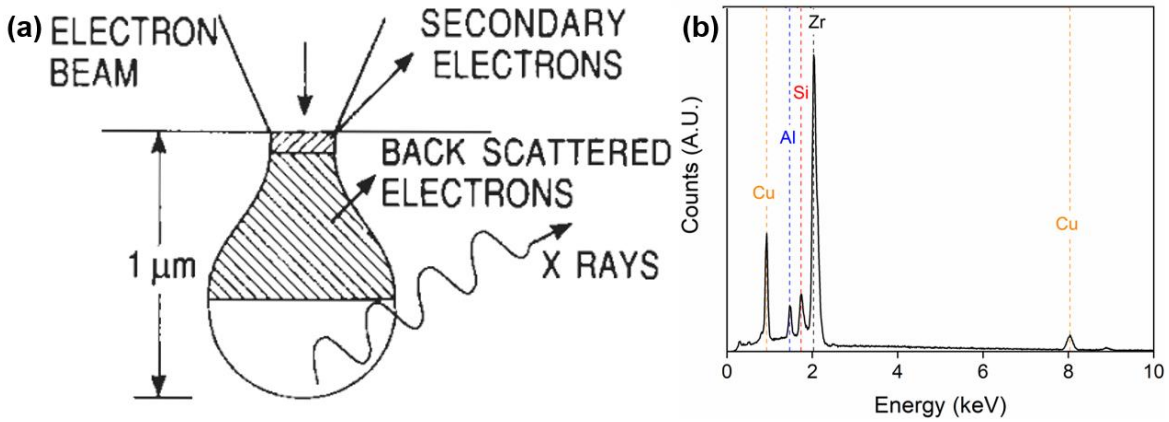

Figure 26*: (a) Photon and electron signals from tear-shaped volume due to sample-beam interactions in SEM* [26]*. (b) Example EDS spectrum on a Zr-Cu-Al thin film grown on a SiN on Si substrate.*

A localized chemical composition can be determined in solid samples by analyzing x-ray spectrum originating from bombarding a sample with an electron beam inside SEM by a technique called energy dispersive x-ray spectrometry. While all elements with atomic numbers (Z) from 4 (Be) to 92 (U) can be qualitatively detected, SEMs typically cannot be used to derive quantitative

results for lighter elements (Z < 10). A qualitative analysis is straightforward and relies on identifying spectra lines. The spectra line intensities can be used to quantify relative concentrations of the elements present in the sample. The films' composition was analyzed by an energy dispersive x-ray spectrometer (EDS) mounted on the FESEM without standards. The EDS measurements were made at a working distance of 9 mm, gun energy of 15 kV and 1000× magnification. Typical EDS spectra for Zr-Cu-Al and Zr-Cu-Al-Ni thin films reveal clear elemental presence of the film and substrate, as represented in Figure 26(b). The composition was quantified by normalizing K-line (Cu, Al, Ni) and L-line (Zr) intensities by their k-factors. For thin film samples, the reliability of EDS depends strongly on film thickness. To avoid dominance of substrate signal, the films should be relatively thick (at least 500 nm for Zr-based alloy systems).

3.2.3 Electron probe microanalysis on Zr-Cu-Al-Ni thin films

The SEM-EDS route of quantifying composition for the Zr-Cu-Al-Ni system was error-prone due to a large substrate signal. Instead, we used a related but more accurate technique called wavelength dispersive x-ray spectroscopy (WDS) inside an electron probe microanalyzer (EPMA) with standards. An electron beam incident at the sample causes emission of characteristic x-rays which are then detected by the EPMA [94]. In contrast to SEM-EDS which utilizes a solid-state semiconductor detector to gather the complete range of x-ray wavelengths produced in the sample, WDS uses Bragg's law to screen for wavelengths of interest and direct them to the EPMA detectors. Chemical composition is then calculated by comparing characteristic x-ray intensities to those of pre-measured elemental standards. Counts are corrected for matrix effects, absorption and secondary fluorescence [92]. Owing to better x-ray peak resolution and signal-to-noise ratio, WDS with standards is a more precise quantitative technique than standard-less SEM-EDS.

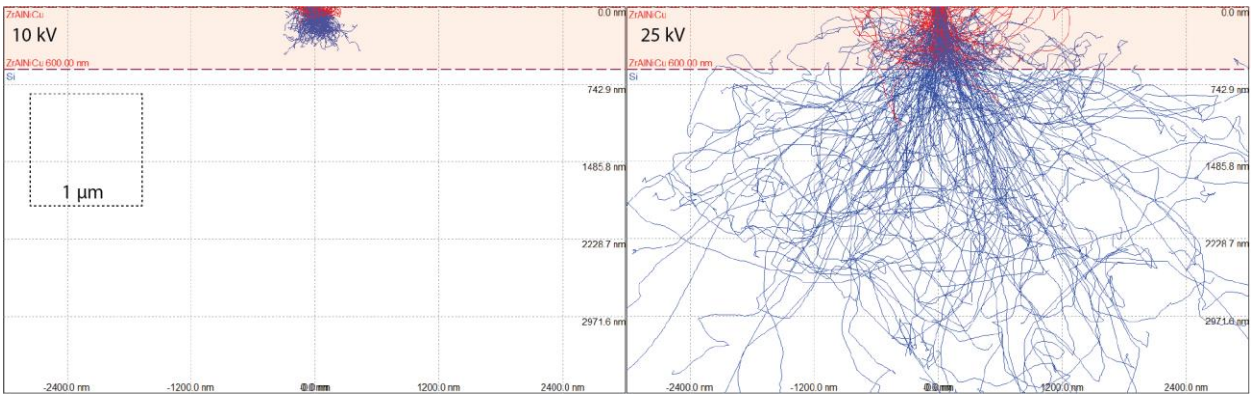

***Figure 27**: Monte-Carlo simulation results of electron-specimen interactions within a 600 nm thin film of $Zr_{55}Cu_{30}Ni_5Al_{10}$ atop Si wafer. By changing primary beam accelerating voltage, it is possible to control activation volume from which X-rays are generated. This image shows the volume from which Si-Kα x-rays are generated within this sample geometry at 10 and 25 kV accelerating voltages.*

EPMA was used to quantify the composition and thickness of thin films and their surface oxidation layer. A Cameca SX-Five-FE EPMA was used to conduct WDS measurements at 10, 12, 15, 20, 25, and 30 kV accelerating voltage to generate characteristic X-rays from different activation volumes within the sample (Figure 27). Analyses were performed at 10-20 nA with either a fully focused beam (~80 nm) or 2-5 µm defocused beam. X-rays from Zr-Lα (LPET), Cu-Kα (LLIF), Ni-Kα (LLIF), Al-Kα (TAP), Si-Kα (LTAP), and O-Kα (PC0) were collected using 5 WDS spectrometers equipped with gas flow proportional X-ray detectors. Pure metals were used as calibration standards for Zr, Cu, Ni, Al, and Si. Synthetic Fe_3O_4 was used as calibration standard for O. An exponential background fit was used for O quantification. Differential pulse height analysis was used for Si-Kα on LTAP to account for high order (n=5) reflections from Cu-Kβ.

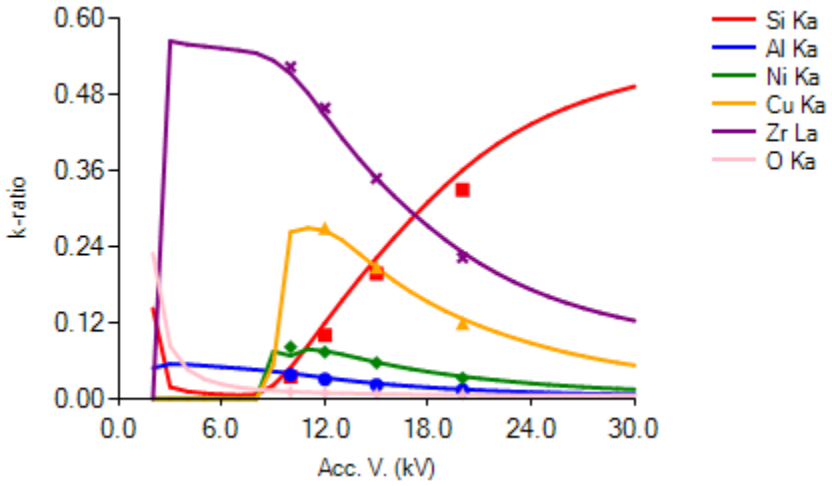

***Figure 28**: BadgerFilm simulation results for ZrCuNiAl thin films with ZrO_2 oxidation layer atop Si substrate. Experimental k-ratios are used to extrapolate the composition and thickness of multi-layered stratified samples.*

Thin film quantification was performed using the BadgerFilm (v1.2.11) Thin Film Analysis Program [95] which performs Monte Carlo simulation of electron and photon transport to model X-ray fluorescence within the thin film and surface oxidation layer. Experimental k-ratios for each element at every accelerating voltage are used as inputs to extrapolate X-ray emission behavior within thin film and surface oxidation layer (Figure 28). These measurements were performed by Drs. John Fournelle and Will Nachlas.

3.2.4 Atomic force microscopy

Atomic force microscopy (AFM) is a common tool to image local morphology of bulk and thin films samples at very high resolutions [96]. An AFM probe has a nanometer-sized sharp tip on the flexible end of micron-sized cantilevers, which in turn are protruding out of a holder [97]. Imaging relies on scans due to deflection of the sharp tipped cantilever as it is brought close to the sample surface as per Hooke's law [96]. The AFM has three imaging modes namely contact,

tapping and non-contact and the choice depends on the desired application. Our measurements primarily used the contact mode – the tip is dragged along the sample surface and the contours typically result from using a feedback signal that keeps the cantilever at a static position. To minimize contributions of noise and drift to the image, low stiffness cantilevers can simultaneously achieve suitably large deflection and maintain a low interaction force. A Bruker Catalyst AFM was used to study surface features of thin films in contact mode at a scan rate of 0.7 Hz.

3.2.5 Calorimetry measurements

The thermal properties of thin films and ribbons were measured by our collaborator, Dr. Chengrong Cao in a high rate differential scanning calorimeter (Flash DSC 2+, Mettler Toledo) at a heating rate of 5000 K/s. Flash DSC measures the heat flows and temperatures at relatively much higher rates (several thousand K/s) [98] related to endothermic and exothermic transitions such as the glass transition and crystallization in melts respectively. This technique relies on measuring as a function of temperature, the difference in the amount of heat required to increase or decrease the temperature of sample and reference pans. Samples were scraped off with razor blades and carefully mounted onto flash DSC chips. We estimate typical sample masses to be between 10 ng and 1 μg. Ar gas was continuously flown (60 ml/min) during testing to minimize sample oxidation. The raw glass transition onset data from DSC measurements was processed in the following manner: first, we applied Savitzky-Golay data smoothing with 20-point window. Then, straight lines fit for the temperature range 360 – 375 K was subtracted from heat flow data. Finally, the heat flow traces were moved vertically such that the corrected heat flow value at 360 K for all samples was zero. The raw crystallization datasets were processed in the following manner: after smoothing, subtraction of straight line and zeroing at 360 K just like processing of the glass

transition onset data, area under the crystallization peak was integrated. Then, the curves were offset to zero at 815 K (supercooled region of all samples) and normalized so that all curves had the same area under the curve.

3.2.6 Nanoindentation

A nanoindenter of Hysitron TI 950 make was used to make elastic modulus and hardness measurements on thin films and ribbon samples. Nanoindentation is a popular technique to measure mechanical properties of small sample volumes. In this technique, a hard tip with known mechanical properties and tip geometry (usually made from diamond) is pressed into the sample and the mechanical properties are determined by observing the impression. Unlike traditional indentation techniques which rely on optically measuring the impressions' dimensions, nanoindentation uses an indenter with precisely known geometry. The instrument continuously records penetration depth and the indent area can be calculated from the tip geometry. An example load-displacement curve is shown in Figure 29. The hardness (H) and reduced elastic modulus (E_r) values are calculated by fitting the unloading curves to a power law, as per the Oliver-Pharr method [99]. H values reported in this study are as per the Meyer formula [100]

$$H = \frac{F}{A_c} \quad (1)$$

while E_r values are determined by the following formula

$$E_r = \frac{0.5 \times (dF/dh)}{\sqrt{(A_c/\pi)}} \quad (2)$$

where F, A_c and h are the applied force, contact area and depth respectively.

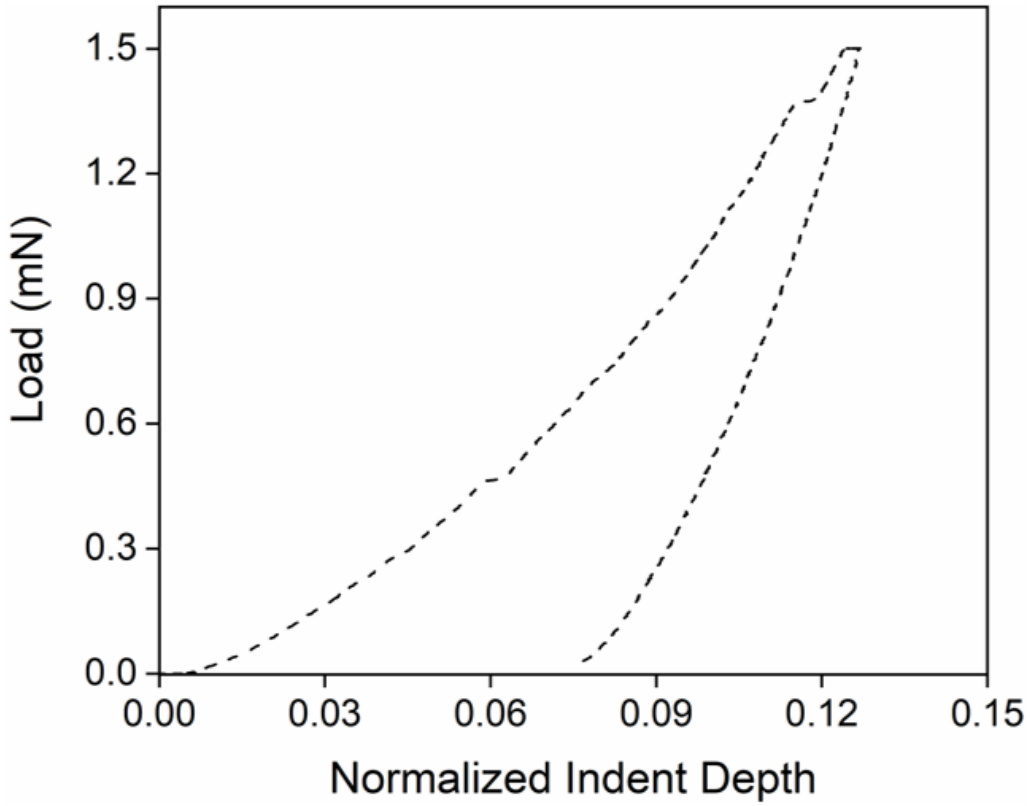

Figure 29: An example load-displacement measurement on one of the MG thin films shows pop-ins, characteristic of MGs. Mechanical properties are calculated by fitting the unloading curve to a power law.

Prior to the actual experiments, the instrument was determined to be satisfactorily calibrated by indenting a standard fused silica sample and ensuring that the mechanical properties were within acceptable range of values. The thin film samples were glued to magnetic pucks with superglue. The bulk ribbon sample was clamped edge-on between two steel clamps and cloth-polished to 0.03 μm. An optimum indent depth was found for each sample by partial unload function [101]: a small force was applied by the nanoindentation probe, withdrawn, and then a slightly higher force was applied, withdrawn, and so on for a prescribed number of cycles. At lower depths, elastic modulus and hardness depend on the indent depth. This dependence ceases above a threshold indent depth and applied force. Also, the threshold depth should be less than 10

– 20 % of sample thickness to minimize substrate effects [102]. Once this threshold depth was identified for each sample, 25 - 50 automated indents of same contact depth were made on each sample using a basic trapezoid load function: the probe ramped up applied force to a preset peak value over 5 seconds, held at the peak value for 2 seconds and then withdrawn over 5 seconds. While the Oliver-Pharr calculation is known to not account for pile-up effects in metallic glasses [103], the pile-up effect is negligible for $h_f/h_{max} < 0.7$ [104] as was the case for our study, where h_f and h_{max} are the residual and maximum indentation depths.

3.2.7 Fluctuation electron microscopy and angular correlations analysis

We combined fluctuation electron microscopy (FEM) experiments with angular correlation to reveal structural differences in metallic glass thin films with different kinetic stabilities. Hwang et al. [105] and Zhang et al. [106] demonstrated that a combination of FEM and hybrid reverse Monte Carlo simulations could reveal nanoscale structural insights at the medium-range order. Figure 30 is a schematic illustration of FEM experiments. FEM uses a high energy, focused electron beam of size 1-2 nm inside a scanning transmission electron microscope (STEM) to measure variance of fluctuations in diffraction measurements from many positions on the sample. The FEM experiment measures normalized variance V of the spatially-resolved intensity I from many nanodiffraction patterns as a function of scattering vector magnitude k and the coherent spatial resolution R. Specifically,

$$V\ (k, Q) = \frac{<I^2(k,Q,R)>}{<I(k,Q,R>^2} - 1 \qquad (3)$$

where < > indicates averaging over position on the specimen. The Rayleigh criterion gives R = 0.61/Q where Q is the radius of virtual objective aperture in reciprocal space [107,108].

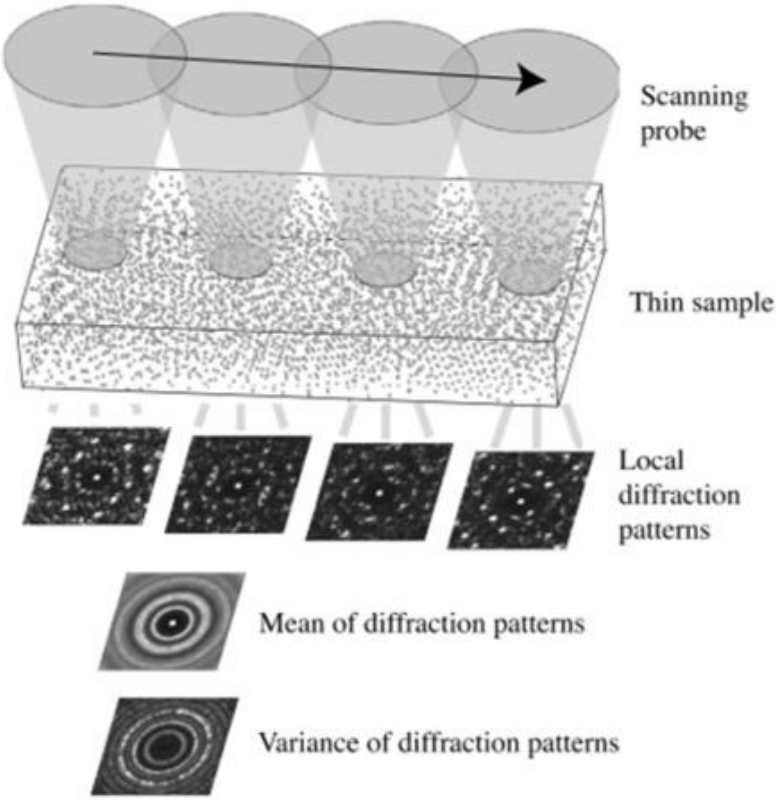

Figure 30: Coherent nano-diffraction patterns originating from different samples positions are used in FEM experiments to characterize glass structure *[108]*.

Nanodiffraction patterns from FEM show Bragg diffraction speckles originating from MRO. Then, the rotational symmetry of MRO can be revealed from rotational symmetry of speckles as a function of k. However, this determination is complicated by occurrence of several ordered regions through the sample thickness with overlapping speckles. Instead, angular correlation functions can identify MRO regions since the diffracted intensity from ordered regions is stronger and more directional as compared to diffuse diffraction from disordered regions [109]. For angular correlation analysis, all nanodiffraction patterns from FEM are converted to polar coordinates and corrected for elliptical astigmatism. Then the angular correlation for individual

patterns, C(φ) as a function of the azimuthal angle φ at a given k is calculated according to the equation below:

$$C(\phi) = \frac{<I(\theta+\phi)\, I(\theta)>_\theta - <I(\theta)>_\theta^2}{<I(\theta)>_\theta^2} \quad (4)$$

Both the individual pattern angular correlations and the summed angular correlations are then analyzed by calculating the power spectrum, giving information about the relative presence of symmetries present in the individual nanodiffraction patterns and structure across the entire sample.

Approximately, 20 nm thin film samples with transmittance of 55 – 65 % were grown directly on electron-transparent Si_3N_4 membranes for FEM measurements. This thickness was previously found to be acceptable for FEM and angular correlation analysis [110]. The FEM measurements were performed by Debaditya Chatterjee on a FEI Titan STEM with probe C_s aberration corrector at 200 kV. 512 × 512 pixel nanodiffraction patterns were acquired with a CCD binning of four on a 10 × 10 grid of positions, covering 30 × 30 nm^2 sample area. Variance data from 10 different sample regions was averaged and reported with one standard deviation of mean error bars. STEM images were acquired via a Gatan annular dark-field detector simultaneously with the nanodiffraction patterns. For our measurements, we chose a probe size of 2 nm, C2 aperture size of 10 μm, convergence angle of 0.6 mrad, spot number 7, and probe current of 3.36 pA [106]. V(k) data was not corrected for surface oxide on the surface of thin films. For the same data set, angular correlation analysis was performed by Carter Francis. The angular correlations for each of the ten sample regions were summed to get its summed angular correlation and power

spectrum, as given in equation (4). Data were averaged and reported with one standard deviation of mean error bars.

3.3 Materials characterization of amorphous carbon thin films

3.3.1 Preliminary characterization

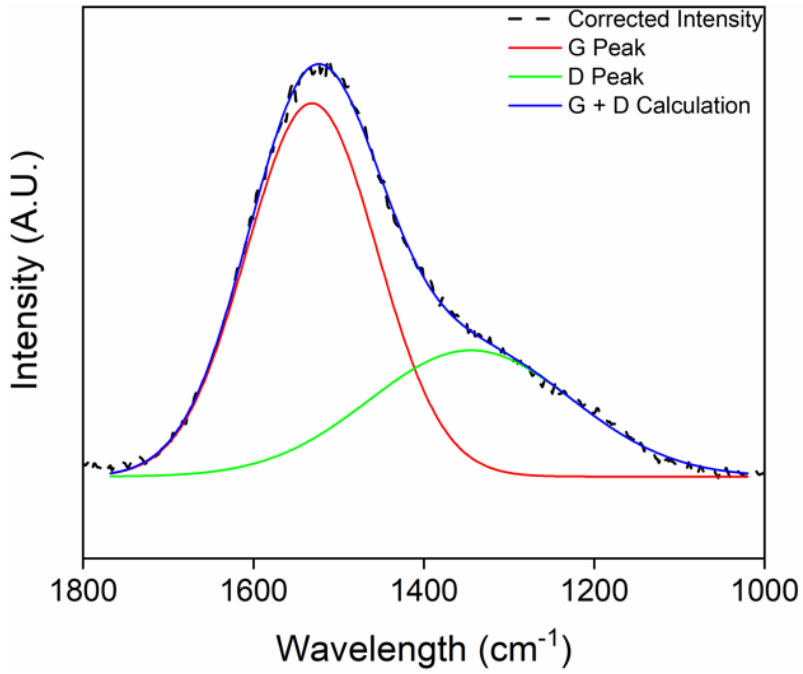

Figure 31*: Fitting a representative Raman spectrum acquired on one of the amorphous carbon films reveals broad G and D peaks.*

The film thickness was measured with Single-Spot Thickness Measurement F20 (Filmetrics). All the films had the thicknesses of about 800-1243 nm. The film structure was characterized by a Thermo-Fisher Scientific DXRxi Raman Imaging microscope with 532 nm Ar laser as excitation source, laser energy of 10 mW, exposure time of 0.2 seconds per scan and 50 scans per spectrum. The Raman spectra were first background-subtracted with a spline fit and then

fitted based on two Gaussian curve shapes (one for G peak and another for D peak) in Origin software. An example is show in Figure 31.

3.3.2 Nanoindentation

The single-layered and multi-layered films' hardness (H) and reduced elastic modulus (E_r) were investigated by nanoindentation experiments, using a Hysitron TI950 triboindenter with a Berkovich diamond tip. Prior to running these experiments, the instrument was found to be satisfactorily calibrated by indenting a standard fused silica sample. Triboscan, a software provided by the instrument maker digitally recorded the load-displacement characteristics while indenting and the H and E_r values were calculated by fitting the unloading curves to a power law, as per the Oliver-Pharr method as reported in section 3.2.6. The elastic modulus E was calculated according to the following formula

$$\frac{1}{E_r} = \frac{(1-\upsilon^2)}{E} + \frac{(1-\upsilon_i^2)}{E_i} \quad (5)$$

where υ and υ_i are Poisson ratios for DLC and the diamond indenter respectively, while E_i gives elastic modulus of the diamond indenter (υ = 0.22 [111], E_i = 1141 Gpa, υ_i = 0.07 [112]). Calculating the residual (h_{res}) to maximum depth (h) revealed that pile-up effect is negligible in our measurements since $h_{res}/h < 0.7$ [112]. In order to minimize the substrate effect, all the indentations were limited to less than 15% of the total film thickness. All data points were averages of at least 10 indentations using the same condition of a trapezoidal loading function with peak load of 2 mN.

3.3.3 Scratch testing

Coefficient of friction measurements was performed on the films by using the nanoscratch feature of Hysitron TI950 triboindenter. In this instrument setting, a normal load is applied by a horizontal capacitive transducer while the lateral force experienced by the scratching tip is measured by two vertical capacitive transducers with load and normal displacement resolutions of 3 μN and 0.04 nm respectively. Using a spherical tip of diameter 1 μm, scratches of length 10 μm were made at constant loads of 3, 6 and 10 mN. The loading cycle was performed with the following steps: first, the tip moved 5 μm to one side of the mean position; then, load was applied over 5 seconds during which the instrument recorded sample surface profile to be later used for tilt correction; finally after reaching peak load, the tip started scratching at a speed of 0.57 μm/s and the load was withdrawn over 5 seconds after a scratch distance of 10 μm. Post-scratching, the same tip was used for imaging at a contact load of 3 μN and the resulting scanning probe microscopy (SPM) images were analyzed by Triboscan software to extract scratch profiles. Gwyddion software [113] was used for post-processing of the SPM images.

Chapter 4 Varying kinetic stability, icosahedral ordering, and mechanical properties of a model Zr-Cu-Al metallic glass by sputtering

This chapter is adapted from the work S. V. Muley et al. "Varying Kinetic Stability, Icosahedral Ordering, and Mechanical Properties of a Model Zr-Cu-Al Metallic Glass by Sputtering", currently under review at Physical Review Materials.

4.1 Background

In this work, we employ deposition rate in magnetron sputtering to manipulate the stability of $Zr_{65}Cu_{27.5}Al_{7.5}$ metallic glass films, creating materials both more stable than and similar in stability to liquid-quenched glass with the same composition. We show using electron nanodiffraction fluctuation microscopy and angular correlations that enhanced stability is correlated to increased nanometer-scale medium-range order in this material, with a marked icosahedral character. We also demonstrate that improved kinetic stability coincides with increased modulus measured by nanoindentation, suggesting improved thermodynamic stability.

4.2 Results

4.2.1 Structural and composition characterization by XRD and SEM-EDS

Figure 32(a) represents XRD data on thin films fabricated at deposition rates of 0.24, 0.83, and 1.19 nm/s and at substrate temperatures of 443 to 453 K **(**0.700 ± 0.007 T_{onset} of reference liquid-quenched ribbon as measured by conventional calorimetry). Films grown at higher temperatures were crystalline, irrespective of the deposition rate. Figure 32(a) shows a first broad diffraction peak at 36.7 – 36.9° and a second broader halo at higher angles. The full width at half maximum (FWHM) of the first peak ranges from 5.24° to 5.64°, depending on the deposition parameters, as shown in Figure 32(b), which corresponds to a scattering vector magnitude q of ~

0.37 $Å^{-1}$ – 0.40 $Å^{-1}$ ($q = 4\pi \sin \Theta / \lambda$, where λ is X-ray wavelength, 1.5418 Å). These values are close to values reported for BMGs (~ 0.4 – 0.5 Å) [114], confirming that the peaks are amorphous by this measure. For amorphous thin films, the position of the first peak is nearly constant at 36.7° ± 0.04°, similar to the value for the ribbon of 36.9°, as seen in Figure 32(c).

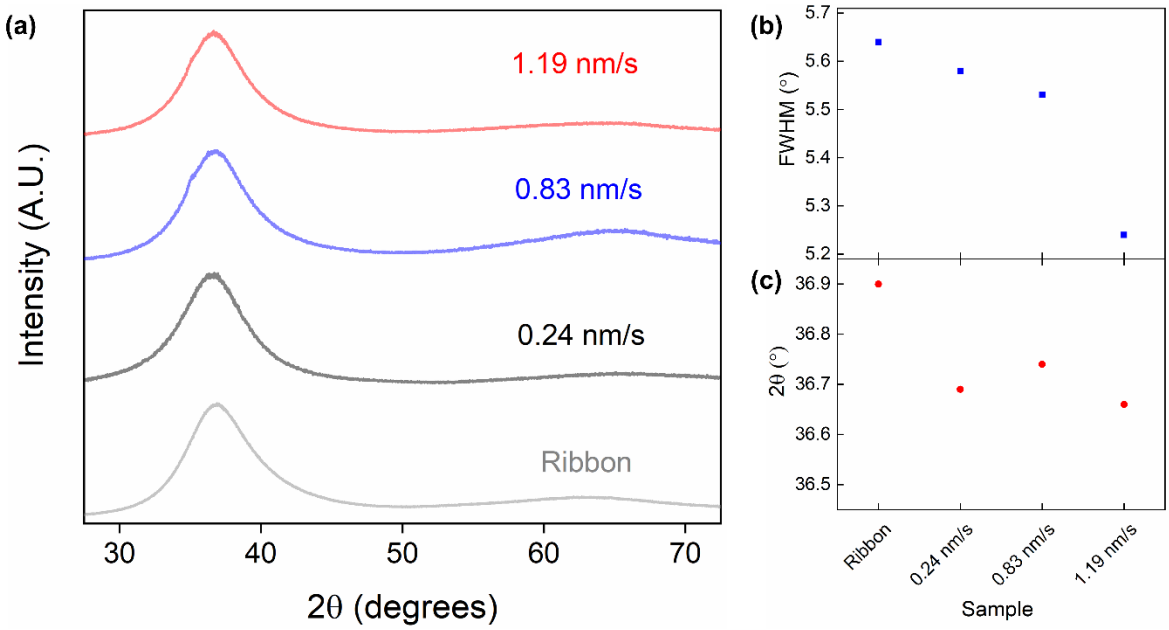

***Figure 32**: (a) X-ray diffractograms are shown for ribbon and thin films (offset for clarity). (b) FWHM and (c) first broad diffraction peak positions for the thin film and ribbon samples.*

Figure 33 shows elemental composition by EDS of the liquid-quenched ribbon, , the sputter target and the films. EDS shows same composition for all the films within experimental uncertainty. Error in each measurement is reported as the standard deviation in EDS measurements at five different spots. The results suggest that for films grown at different deposition conditions, the composition difference is within 1%, while the bulk ribbon and target differ by 2%. The variations in composition are too small to account for the differences in T_{onset} reported in section 4.2.2.

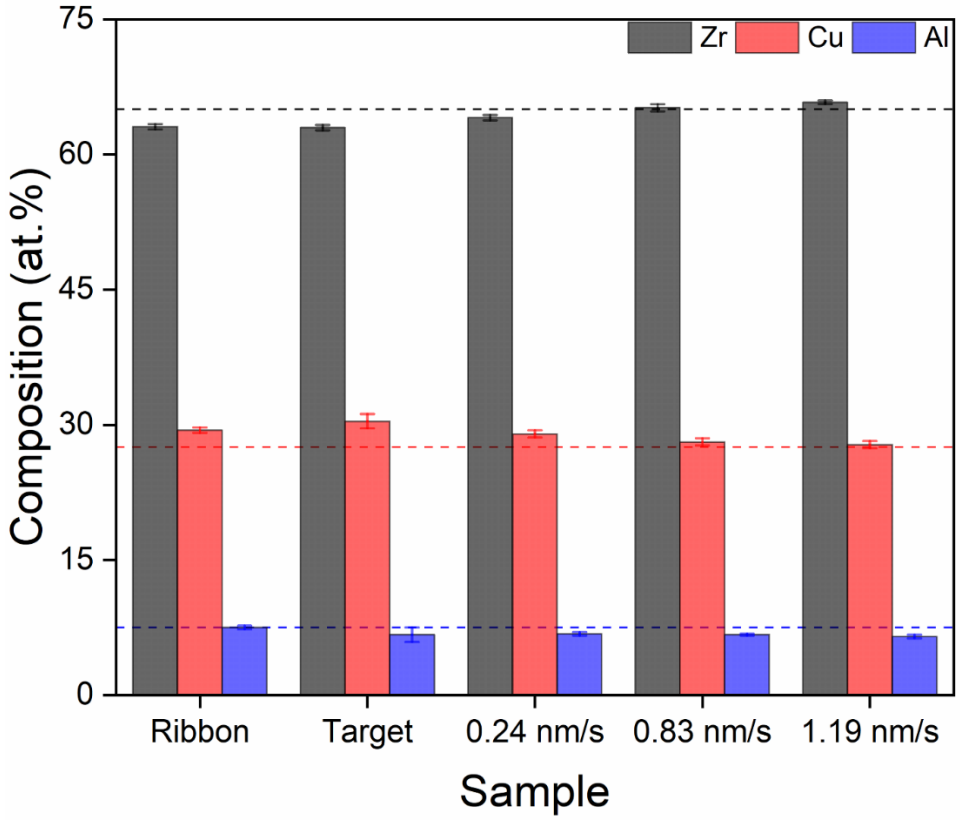

***Figure 33**: Compositions of ribbon, thin films and target source as measured by SEM-EDS are shown. Dashed lines represent nominal alloy composition.*

4.2.2 High rate calorimetry

Figure 34 summarizes high rate calorimetry data measured at a heating rate of 5000 K/s for the films and ribbon. Glass transition onset temperatures T_{onset} estimated by the standard tangent method for all samples are reported in this study. Figure 34(a) shows that the slower deposited films (0.24 nm/s and 0.83 nm/s) have enhanced kinetic stability as shown by a T_{onset} increase of 25 ± 5 K compared to the bulk ribbon sample. The film deposited at 1.19 nm/s has nearly the same T_{onset} as the ribbon sample within experimental error. This trend in T_{onset} with respect to deposition rate is also observed for DSC measurements at heating rates of 1000 and 2000 K/s (not shown).

All the reported T_{onset} data are higher than previous reports on similar compositions using conventional DSC, partly because of the high heating rate. High thermal rate DSC is preferred over conventional DSC in our experiments since it enables studies on relatively thin films, avoiding the very long depositions required to accumulate the large sample volumes necessary for conventional DSC.

Figure 34(b) represents the crystallization signal from f-DSC. While the ribbon shows a single crystallization peak with a well-defined supercooled liquid region, all the films on the other hand show a lower crystallization onset temperature and two crystallization exothermic peaks. The lower onset temperature and the first crystallization event may result from heterogeneous nucleation of crystals at the film surface for the relatively thin films (< 1 μm) we have studied. The second event, which occurs at approximately the same temperature as the crystallization of the ribbon, is then bulk crystallization from the interior of the film [115,116].

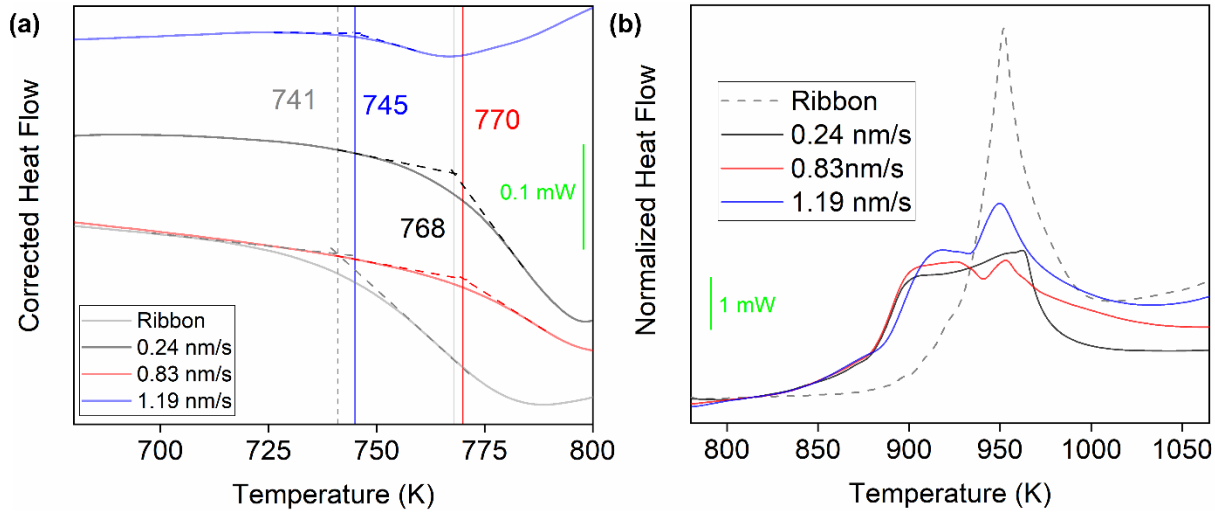

***Figure 34**: Calorimetry data at a heating rate of 5000 K/s showing (a) T_{onset} values and (b) crystallization behavior. Raw data have been smoothed and background-subtracted as described in section 3.2.5.*

4.2.3 Fluctuation electron microscopy and angular correlations

Figure 35 shows electron nanodiffraction structural characterization results for a set of thinner films directly deposited onto electron-transparent Si_3N_4 substrates at the same temperature as a function of deposition rate. Nanodiffraction patterns from many sample positions were measured using a high coherence, focused electron beam 2 nm in diameter in a scanning transmission electron microscope (STEM). Figure 35(e) shows one such example pattern. Quantitatively, V depends on the three- and four-atom position correlation functions. Qualitatively, nanoscale-sized structural variations increase $V(k)$, and internal atomic arrangements within strongly diffracting regions are revealed by the position of peaks in k. Figure 35(a) shows the $V(k)$ data, with error bands representing the standard deviation of the mean of $V(k)$ calculated from at least 10 different areas of the sample. All the samples have a broad peak centered near ~ 0.40 $Å^{-1}$. The slower deposition rate samples (0.24 nm/s and 0.83 nm/s) have a low-k shoulder at ~0.36 $Å^{-1}$. There is an additional high-k feature in the faster deposition rate sample (0.83 nm/s and 1.19 nm/s) at 0.46 or 0.48 $Å^{-1}$, respectively, and there may be a small feature near ~0.42 $Å^{-1}$, although it is not outside the errors bars of the data.

Figure 35(b)-(f) shows the power spectrum of angular correlations computed from the same set of nanodiffraction patterns, which complicates and expands this structural picture. Angular correlations and their power spectrum probe the approximate rotational symmetries exhibited by the nanoscale structure of a glass [16,17]. Starting from the pattern shown in Figure 35(e), an example power spectrum was computed as shown in Figure 35(f). This pattern was selected out of the data set to show strong $n = 10$ symmetry.

The angular power spectrum will identify ordered, rotationally symmetric structures because the diffracted intensity from ordered regions is stronger and more directional than the diffuse diffraction from disordered regions [109]. However, previous angular power spectrum results comprise of significant odd-*n* components which are inconsistent with Friedel symmetry in diffraction and were argued to be unphysical [117]. Recently, these odd-*n* features were shown to be artifacts from TEM samples that are too thick [118], presumably due to chance alignments of speckles arising from different structures that overlap through the projected thickness of the TEM sample. Our samples are thin enough to minimize these artifacts.

Figure 35(b)-(d) show the power spectrum of the summed angular correlations for 4-, 6- and 10-fold symmetries respectively, with error bands representing the standard deviation of the mean of $P(k, n)$ computed from at least 10 different areas of the sample. The slowest deposition rate, 0.24 nm/s sample shows substantially more structure in the 4-, 6-, and 10-fold power spectra than the other two samples, and it has the highest ratio of even to odd total power at 1.9. For the slowest rate sample, $P(k, n=4)$ has clear peaks at 0.36, 0.39, and 0.438 $Å^{-1}$, $P(k, n=6)$ has peaks at 0.385 and 0.42 $Å^{-1}$, and $P(k, n=10)$ has peaks at 0.37 and 0.42 $Å^{-1}$. The fastest deposition rate, 1.19 nm/s sample shows the least structure in $P(k, n)$. There are broader peaks near $k = 0.40$ $Å^{-1}$ for $n =$ 4, 6, and 10, and features in $P(k, n=4)$ near 0.42 and 0.475 $Å^{-1}$. The intermediate rate, 0.83 nm/s sample, has intermediate features in $P(k, n)$, including a small feature in $P(k, n=10)$ near $k = 0.36$ $Å^{-1}$. The ratio of even to odd power is 1.51, somewhat smaller than the fastest rate sample.

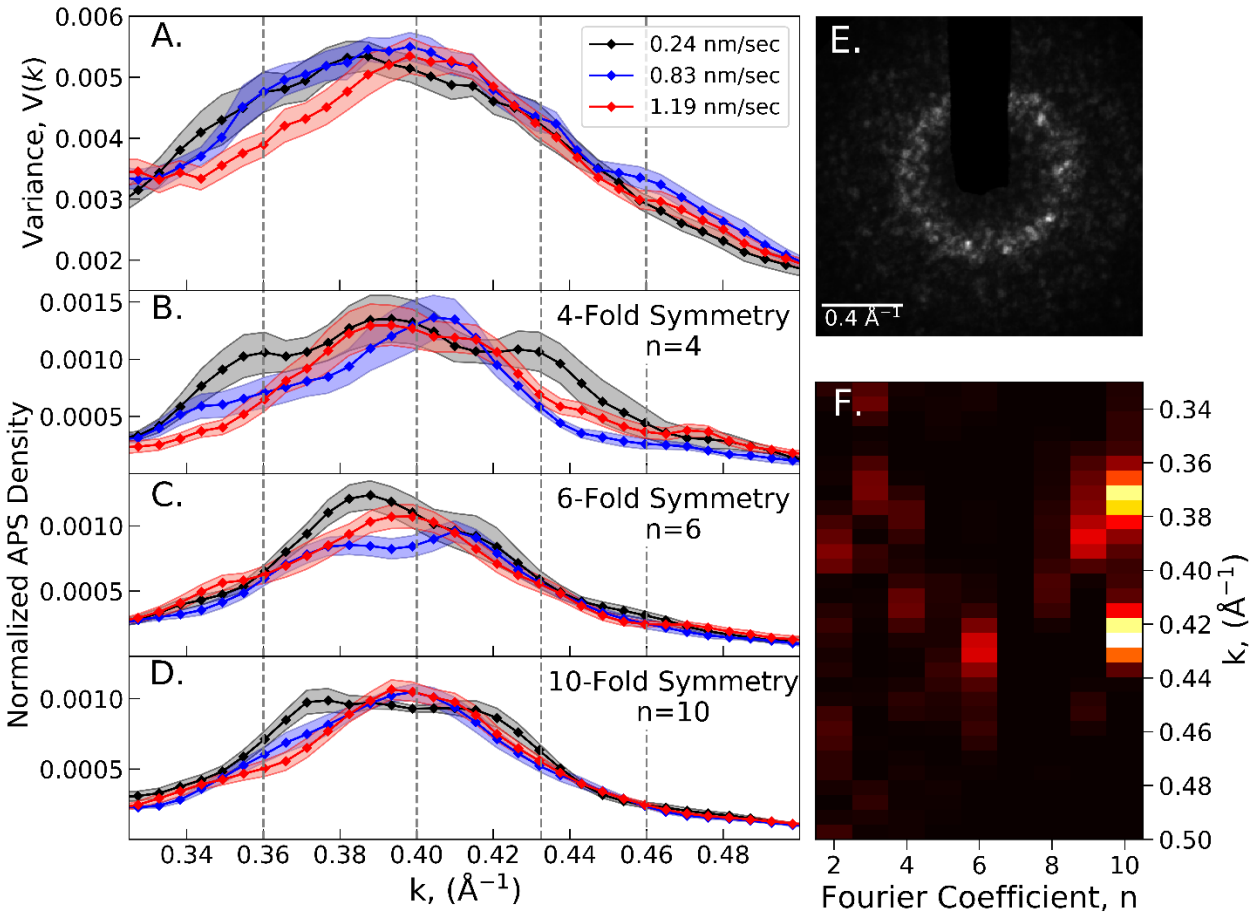

***Figure 35**: (a) V(k) measured Zr65Cu27.5Al7.5 MG films deposited at different deposition rates. Normalized average power spectral density of the (b) 4-fold, (c) 6-fold and (d) 10-fold rotational symmetry in nanodiffraction for all samples. (e) An example nanodiffraction pattern showing the polar coordinates (k, φ) used in Eq. (4). (f) The power spectrum of the pattern in (e) showing strong 10-fold symmetry.*

Figure 36 shows all the average angular power spectra for $n = 1$ to $n = 10$. $n = 1$ corresponds to single speckles without symmetry-related partners, presumably arising from ordered arrangements of atoms that satisfy a pseudo-Bragg condition on one side of the optic axis (*i.e.* **+g**) but not the other side of the optic axis (*i.e.* **-g**). $n = 2$ are Friedel pairs. Odd orders $n \geq 3$ arise from some chance correlation of speckles arising from random overlap of ordered structures along the

beam direction through the TEM sample thickness. Even orders $n \geq 4$ can have some contribution from random correlations but can also arise from rotational symmetries of single ordered regions. Because the even *n* symmetries are systematically higher power than the odd *n* symmetries, we interpret the even *n* symmetries as arising from real rotational symmetries in the material [118]. These results show that the even *n* power is systematically larger than the odd *n*-1 or *n*+1 powers. Ignoring the *n*=1 power created by isolated, single speckles, the ratio of even *n* power to odd *n* power ranges from 1.5 to 1.9 for the three samples.

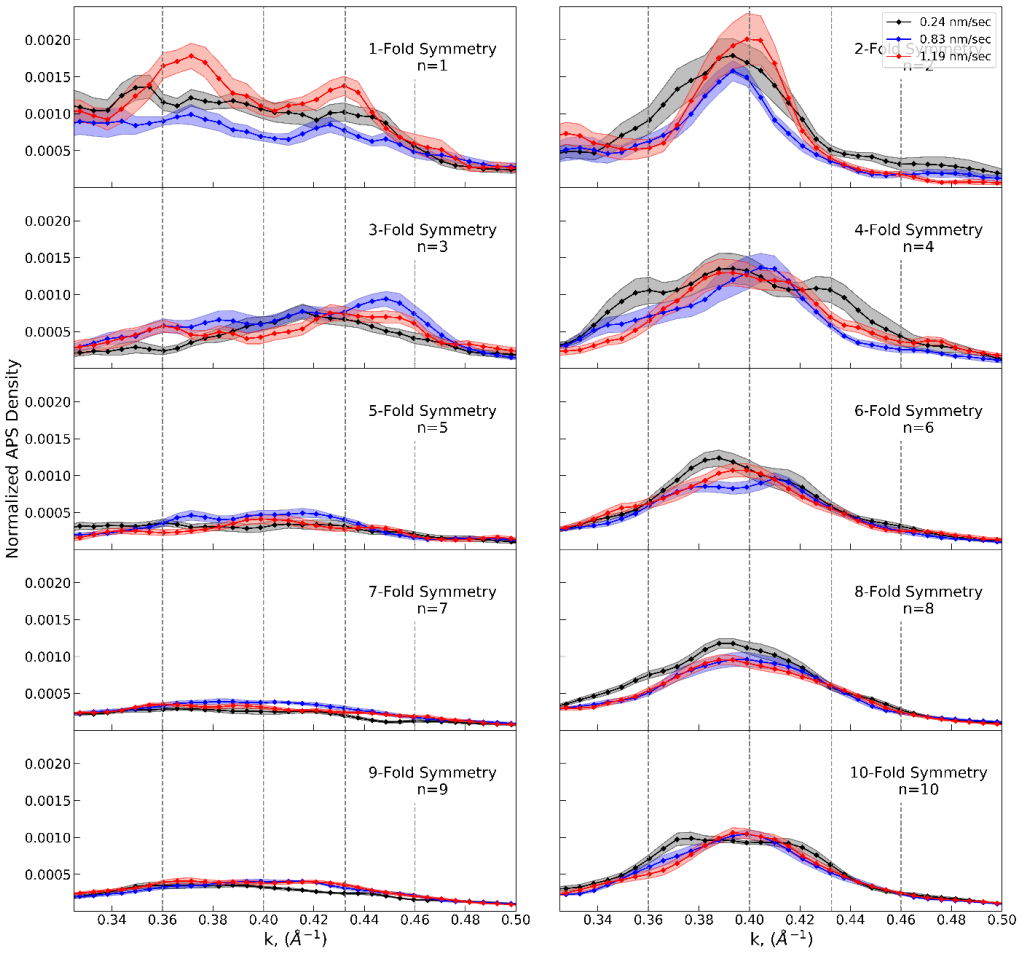

***Figure 36**: Average angular power spectrum for n = 1 to 10 for all three samples with the same vertical scale for every order.*

4.2.4 Mechanical properties

Figure 37 shows the reduced elastic modulus (E_r) and hardness (H) as a function of T_{onset} values for the films and the ribbon. All the films have higher E_r than the ribbon, and the film E_r increases 5% with T_{onset}. At constant composition, E is related to the interatomic potential U, average atomic radius r_0, and the bonding length between two atoms r by [119] $E = \frac{1}{r_0}\left(\frac{1}{r}\left(\frac{dU}{dr}\right)\right)$. The small variation in measured composition of ± 2 at. % shown in Figure 33, even if it is real and not composition measurement uncertainty, accounts for at most a 0.8% variation in modulus, as estimated by composition-weighted averages of the elemental moduli. For the thin films, H increases by 14% with decreasing deposition rate and increasing T_{onset}. The difference in hardness between the slowest 0.24 nm/s film and the ribbon reference sample is 3.8%. We also measured a ~ 3 μm thick film grown at a deposition rate of 0.83 nm/s to look for sample size effects on the glass's mechanical response. The results were consistent within experimental uncertainty with results on the thinner film grown at same deposition condition.

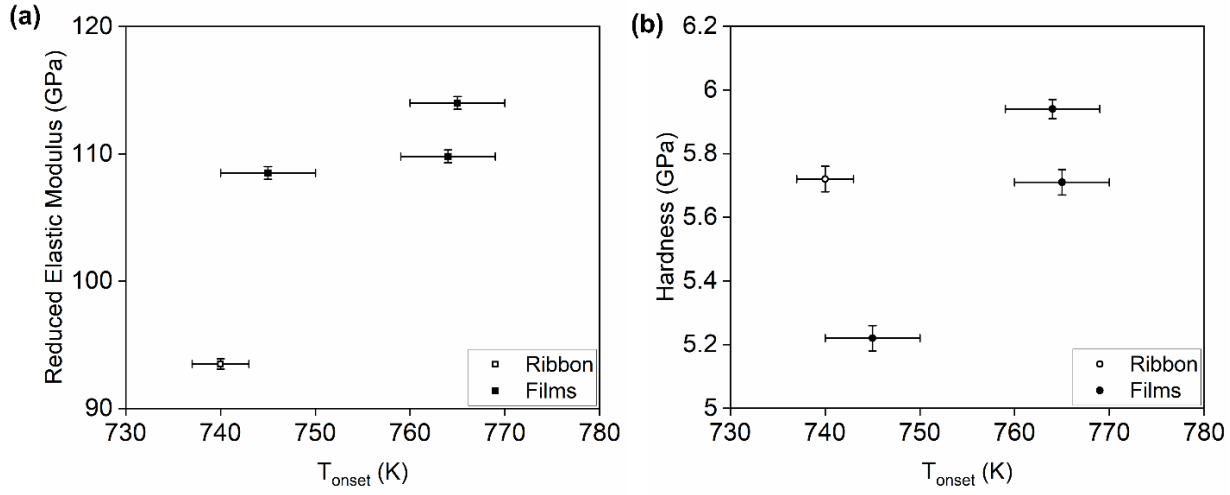

***Figure 37**: (a) Reduced elastic moduli and (b) hardness vs T_{onset} for thin films and ribbon samples.*

Figure 38 compares images of indents made at a peak load of 1.5 mN in the ribbon and the thick, 0.83 nm/s film. Figure 38(a) and (b) show gradient force images (scanning set point error), and Figure 38(c) and (d) show two-dimensional surface maps. The indents in the ribbon are surrounded by pileups, but no pileups are observed for the film indents. This difference in pileup behavior was consistent up to higher peak loads of 16 mN, and images of indents (not shown) in the thinner films also showed no pileups.

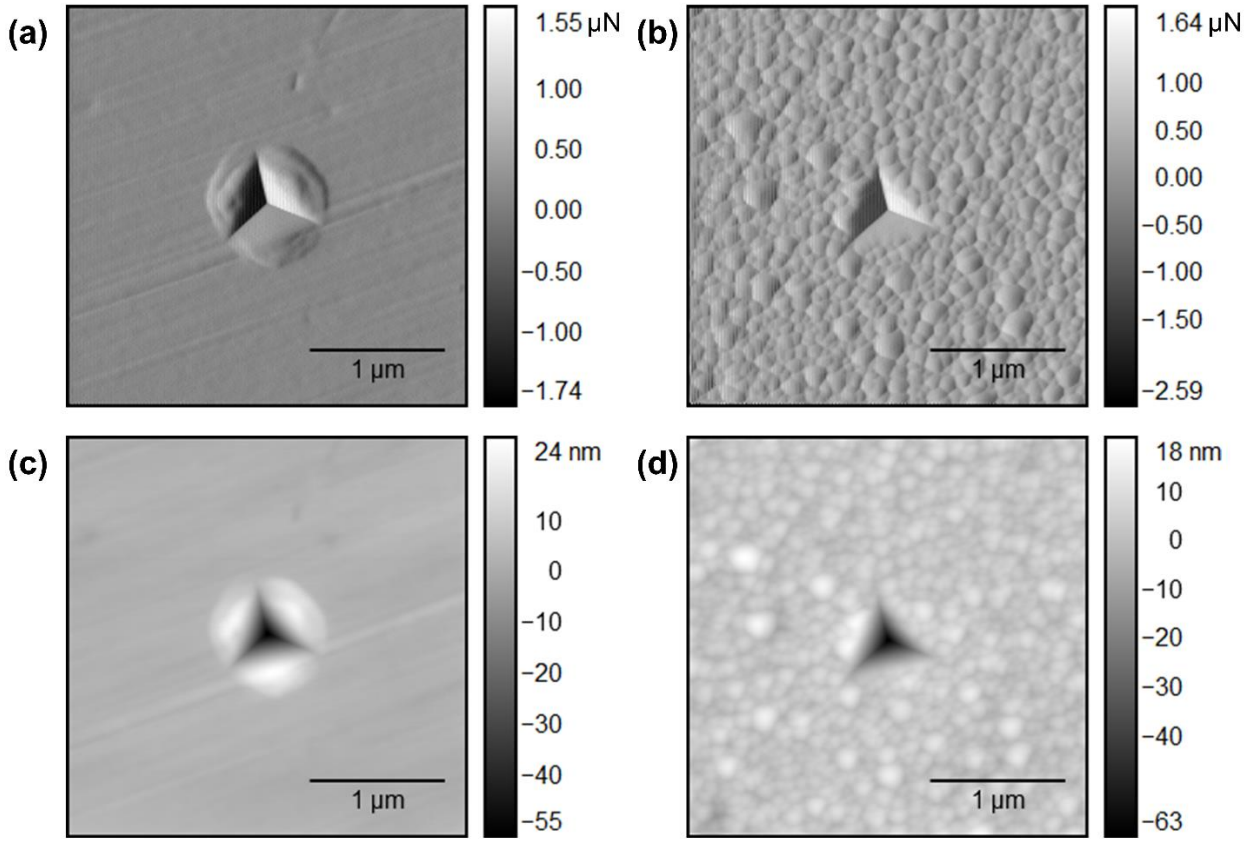

Figure 38*: (a) and (b) show gradient force images (scanning set point error) while (c) and (d) show two-dimensional surface maps for ribbon and the ~ 3 µm thick film grown at a deposition rate of 0.83 nm/s respectively.*

4.2.5 Microstructural characterization

As shown in Figure 39, the 0.24 nm/s and 0.83 nm/s samples have a similar root mean square (RMS) roughness of 3.7-3.8 nm and a similar roughness length scale (~ 70-90 nm), based on AFM and SEM images. The 1.19 nm/s sample on the other hand shows a bimodal distribution of a few large hillocks (~ 110 nm) distributed in a matrix of smaller ones (~ 45-50 nm). It also has a smoother surface, with an RMS roughness of 1.6 nm. The mean hillock size, determined by applying the grain-intercept image analysis method used to determine crystal grain sizes, is 66, 71, and 73 nm for the 0.24 nm/s, 0.83 nm/s, and 1.19 nm/s samples respectively. The slower deposited films have much taller hillocks (~16-18 nm), while the fastest deposited film has shorter ones (~7-8 nm).

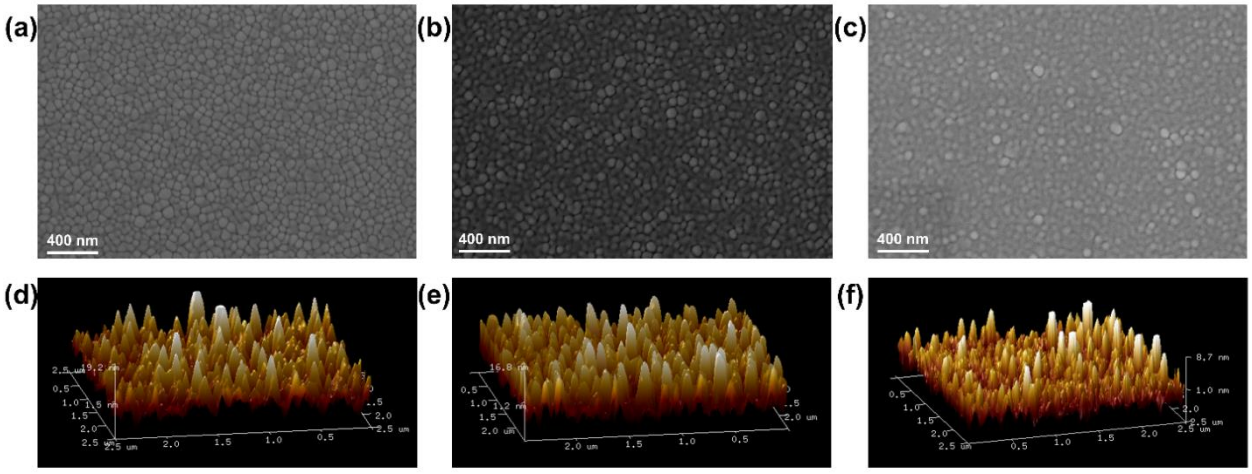

Figure 39*: Plan view SEM (top) and AFM images (bottom) of thin films grown at deposition rates of (a), (d) 0.24, (b), (e) 0.83 and (c), (f) 1.19 nm/s.*

A widely accepted rule of thumb to avoid influence of surface roughness on nanoindentation measurements is to employ an indentation depth ~ 20 times the RMS roughness,

which we have done. Given that precaution and the small differences in the size of the hillocks, it seems unlikely that surface roughness is the major cause of the differences in mechanical properties amongst the films measured by nanoindentation. However, the ribbon has a smoother surface because it was polished before nanoindentation testing, so some of the difference between the ribbon and the films may be attributable to surface roughness.

4.3 Discussion

The nanodiffraction data show that the film's structure grows more icosahedral with decreasing deposition rate and as the films increase in T_{onset} and grow more kinetically stable. Previously, in bulk Zr-Cu-Al metallic glasses, we have used FEM data and hybrid reverse Monte Carlo (HRMC) modeling to show that the low-k shoulder on the main $V(k)$ peak, near k = 0.36 Å^{-1} in Figure 35(a), arises from icosahedral ordering, and the main peak (k = 0.40 Å^{-1}) and the high-k shoulders (k = 0.44 – 0.48 Å^{-1}) arise from crystal-like order [106,120]. Icosahedral order in the HRMC models is identified as regions with icosahedral or quasi-icosahedral Voronoi polyhedra and local, approximate five-fold rotational symmetry. "Crystal-like" order is identified by regions with approximate six-fold rotational symmetry [106,120]. Shifts in the $V(k)$ peak positions occur because the geometry of different types of clusters produces different pseudo-planar alignments of atoms which give rise to strong speckles in nanodiffraction [120]. Interpreted in the same way, Figure 35(a) shows that all of the films have both icosahedral and crystal-like nanoscale structural order, but that the lower deposition rate films, especially the lowest rate, 0.24 nm/s film, have stronger icosahedral nanoscale order than the high deposition rate film, as shown by the higher V at k = 0.36 Å^{-1}. The two higher rate films have relatively stronger crystal-like order, given the high-k features, than the lowest rate film, which has no features at k > 0.40 Å^{-1}.

The angular symmetries reinforce and expand this finding. The angular symmetries show that the structural order in the slowest sample is both icosahedral and crystal-like. 10-fold symmetry arises only from icosahedral order, so peaks in $P(k, n=10)$ confirm icosahedral ordering. 4-fold symmetry arises only from crystal-like order, so peaks in $P(k, n=4)$ confirm crystal-like ordering. 6-fold symmetry can arise from either crystallographically-allowed 6-fold symmetry, Friedel doubling of crystallographically-allowed 3-fold symmetry or doubling of diffraction from the 3-fold symmetry axis of an icosahedron. As a result, the peaks in $P(k, n=6)$ are hard to assign uniquely, but the lower k position of the main peak compared to the data for the other two samples suggests a different structural origin, pointing perhaps to icosahedral instead of crystal-like structures. Combined with the FEM data, these results suggest contribution of a stronger icosahedral character to the nanoscale order in this sample. Unlike the FEM results, this result does not depend on structural modeling. Instead, it is derived directly from rotational symmetries in the data. The higher overall magnitude of $P(k, n)$ for the slowest sample shows that this sample has, on average, brighter, more symmetric speckles in nanodiffraction than the other two samples, suggesting that its well-ordered, strongly diffracting regions occur at higher density, have more perfect internal order, or are larger, or some combination of all three. Angular symmetry mapping with a fast detector might distinguish these scenarios [118], but the spatial sampling of the current data is not sufficient for that type of analysis.

For the fastest deposition rate sample, the features in $P(k, n=4)$ are consistent with the assignment of features in $V(k)$ at similar k to crystal-like order, and suggest that on balance this sample has more crystal-like character to its order. The ratio of even to odd order power is 1.61, and much of that power is concentrated in $P(k, n=2)$, suggesting less overall order and either

smaller or less internally structured ordered regions. The intermediate rate, 0.83 nm/s sample is also intermediate in structural order. The small feature in $P(k, n=10)$ near $k = 0.36$ Å^{-1} is consistent with $V(k)$ and icosahedral ordering, but not as pronounced as the slowest rate sample. It does not show a similar peak in $P(k, n = 4)$, indicating substantial crystal-like order.

The mechanical property results are consistent with increased stability of the glass at lower deposition rate. An increase in E can result from a shortened average interatomic distance and a denser glass structure, making it a proxy for glass thermodynamic stability [39,44,121]. The modulus results suggest that all the films have higher thermodynamic stability than the ribbon sample. The mechanical energy needed for onset of plasticity has been related to the glass fictive temperature, T_f, which is another, indirect measure of thermodynamic stability [122]. The change in fictive temperature is $\Delta T_f = - \Delta\sigma_y V/\Delta C_{lg}$, where $\Delta\sigma_y$ is the change in yield strength, V is the molar volume, and ΔC_{lg} is the difference in heat capacities of the supercooled liquid and the glass extrapolated to a temperature below T_g. T_f is then related to the enthalpy required for the glass transition by $\Delta H = \Delta T_f \Delta C_{lg}$ [122]. For our composition, ΔC_{lg} = 23.6 J/mol.K [39] and the molar volume is 11.4 cm^3/mol. With a Tabor factor of 1/3, $\sigma_y = H / 3$ [123]. If we compare the 0.24 nm/s slowest rate film to the 1.19 nm/s fastest rate film, $\Delta T_f = 116 \pm 5$ K and $\Delta H = 2.7 \pm 0.1$ kJ/mol, derived from the hardness. These changes are significantly larger than examples previously reported changes in T_f (~ 75 K) and H (~ 1.5 kJ/mol) created by thermal aging in Zr-based glasses [124,125] measured by calorimetry. The difference in hardness between the slowest 0.24 nm/s film and the ribbon reference sample is 3.8%, which results in $\Delta T_f = 35 \pm 5$ K and $\Delta H = 0.9 \pm 0.1$ kJ/mol. We suggest the hardness differences between slower deposited films and reference ribbon sample are likely underestimated due to the influence of microstructure between the ribbon and the films, including roughness (Figure 39) and possibility of columnar growth [126,127].

Part of the motivation for this work was to attempt to replicate and expand on the previous work of Yu et al. on the same glass forming system [39]. While we have replicated their results in general by using sputtering to manipulate the stability of same composition metallic glass thin film, we do not replicate the results in detail. Films we grew at the same substrate temperatures they used (> 0.707 T_{onset}) were crystalline, not amorphous, but the fractional change in T_{onset} we find for our glassy films as a function of deposition rate at lower substrate temperature is twice what they reported. This result points to a need for significantly improved process control over key parameters that could include the chamber base pressure and residual gas composition, process gas pressure and trace contaminants, plasma energy density at the sample, *etc.*, if enhanced stability metallic glass coatings are to see reliable use in applications.

The changes in stability we report are smaller than those reported by Luo et al. [38] and Magagnosc et al. [44]. Luo et al. [38] report a 8.5% T_{onset} increase for a one decade reduction in deposition rate, but we observe a 3.3% T_{onset} increase for ~ 0.7 decade of deposition rate. This difference may arise because IBAD enables overall one decade lower deposition rates than our work and has a more energetic plasma (100 – 2000 eV) than sputtering (1 – 100 eV) [128], which might densify the film or enhance surface mobility. Organic glass films exhibit a significantly weaker dependence of kinetic stability of deposition rate, with a 5% increase in T_{onset} reported from a two decade reduction in deposition rate [129]. We suggest this difference is connected to the fragility, *m*, of the different glass systems, which is 80-90 for indomethacin and 40-50 for Zr-based MGs [39]. Magagnosc et al. [44] reported ΔT_f of 333 K and ΔH of 6.19 kJ/mol for a Pd-Si-Cu glass films by substrate temperature control, which is very large, but that results reflects the reduced stability possible in deposited films at low temperature, as well as enhanced stability at high temperature, and not the difference to a quenched glass reference. The influence of stability

on crystallization onset temperature is also complicated. We observe a lower crystallization temperature with higher stability, probably due to surface crystallization. Yu et al. [39] reported nearly the same crystallization temperatures for their ultrastable glass and bulk ribbon, and Luo et al. [38] and Aji et al. [43] both observed higher crystallization temperatures with enhanced stability. More generally, sputtered metallic glass films often have different crystallization pathways than bulk glasses [126,130], so this is an area which requires additional research.

Changing a glass's stability changes its structure and mechanical properties. In structure, the results on film samples here fit within a picture we have previously developed for Zr-Cu-Al glasses in which icosahedral and crystal-like order compete at the nanoscale. Previously, we had shown that changes in composition which increase glass-forming ability (from $Zr_{50}Cu_{35}Al_{15}$ to $Zr_{50}Cu_{45}Al_5$) also increase both the prevalence of icosahedral order and its stability under sub-T_g annealing [106,120]. In those experiments, changes in enthalpy and T_{onset} were dominated by the changes in bond energies arising from changes in composition, rather than arising from changes purely in structure. Here, we show similar behavior, but at constant composition: increased order at the nanoscale gives rise to overall increased stability, and that order tends to be icosahedral. The higher modulus and hardness observed here are consistent with higher density at low deposition rate and higher substrate temperature, as observed in other materials [121]. The higher density is accommodated by denser atomic packing, leading to increased nanoscale structural order. Molecular dynamics simulations of vapor-deposited Zr-Cu-Al glass films also show that more stable glasses have a markedly higher fraction of icosahedral nearest-neighbor clusters than simulated glasses created by quenching from a liquid [131]. Also in molecular dynamics simulations, nearest-neighbor icosahedral clusters exhibit slower dynamics than other clusters in the liquid [58], greater resistance to local transformations in structure, and increased heat capacity

and barrier to crystallization in the glass [60,132], all of which is consistent with increased icosahedral order leading to increased T_{onset}, as observed.

Lack of pileup around the film indents is likely a sign of homogeneous plastic deformation and suggests brittle failure. The amorphous structure is intrinsically heterogeneous and large clusters of inherent defects can be fertile sites for percolation of shear transformation zones [133]. Simulations show more icosahedral ordering can cause higher resistance to shear transformation zones' activation and operation, reducing the chance for localized plastic flow and promoting homogeneous plastic deformation [133]. On the other hand, material pileup in Zr-based bulk glass samples is well documented, indicating the plastic deformation is localized and dominated by heterogeneous nucleation, resulting in subsequent sliding of shear bands as governed by exceeding a critical flow stress [134,135]. Our results are in contrast Magagnosc *et al.* [44], who reported shear banding for their more stable glassy films.

Simulations also support the connection between icosahedral ordering and higher strength, [136–138] measured here as higher hardness. Peng *et al.* [137] showed in CuZr that local five-fold rotational symmetry in the structure is correlated to reduced non-affine displacement under strain, meaning that five-fold symmetric local structures (including icosahedra) were harder to deform than other parts of the glass structure. They also showed that plastic deformation started at regions with low five-fold order and proceeded towards regions with high five-fold order. Cheng et al. [136] reported that mechanical properties in CuZr MGs have a structural origin in the relative populations of icosahedra and liquid-like clusters, with more icosahedral clusters leading to lower potential energy and stronger resistance to deformation. If a MG has more liquid-like clusters than the percolation limit, the glass-to-liquid transition will be easier resulting in poorer mechanical

properties [138]. We suggest that the liquid-like clusters in their simulations have reduced structural order compared to the rest of the glass, so the overall enhanced order we observe may relate to a reduction in the concentration of liquid-like clusters, consistent with the increased hardness.

4.4 Summary

In summary, we report that kinetic stability of sputtered metallic glass thin films can be controlled by the deposition rate at constant substrate temperature from stability similar with liquid quenched glasses to significantly more stable. Structural studies using electron nanodiffraction show that the improved kinetic stability originates from increased nanoscale order in the glass, especially in the form of nanoscale clusters of icosahedra. Modulus and hardness both increase with increasing kinetic stability, suggesting that the higher kinetic stability also means higher density and lower enthalpy. These results show that increased icosahedral nanoscale order increases the resistance of the glass to changes in structure, either thermally in the form of the glass transition or mechanically in the form of plastic deformation. These correlations are drawn entirely at constant composition, so they derive purely from changes in structure without the complexities of changes in bond strength due to changes in composition.

Chapter 5 Optimizing mechanical properties in single-layered and multi-layered amorphous carbon coatings for industrial applications

This chapter is adapted from the manuscript under preparation: S. V. Muley et al. "Optimizing mechanical properties in single-layered and multi-layered amorphous carbon coatings for industrial applications". NCD Technologies is a Madison-based company that makes amorphous carbon coatings as per their customers' needs. With a goal to understand processing-structure-mechanical property correlations in DLC coatings, I along with my supervisors, Drs. Patrick Heaney and Aiping Zeng at NCD wrote up a proposal that was funded by the Advanced Materials Industrial Consortium Seed Program Award. For this project, my primary role was to provide materials characterization consulting while the thin film samples were prepared by Dr. Zeng.

5.1 Background

We report processing-structure-property correlations with an emphasis on bonding fraction and mechanical properties in hydrogenated DLC containing fullerene structures. We systematically reveal structural origin of mechanical behavior in single-layered amorphous carbon thin films and then extend this understanding to develop recipes for multi-layered thin films that show a better combination of desired properties including coefficient of friction and wear resistance while preserving high hardness.

5.2 Results and discussion

5.2.1 Dependence of deposition rate on growth parameters

Figure 40 summarizes monotonically increasing deposition rate as a function of increasing deposition parameters, namely bias voltage, pulse width and frequency. By employing a PIII-based

PECVD for a:C-H thin film fabrication, a D.C. pulser served as an ionization power source and hydrocarbon precursors were used as the carbon source. The pulser supplied variable bias voltage to easily 'tune' the ionization and the C^+ ions' energies in the deposition process and consequently, the sp^3 content in thin films. Also, the variable substrate bias voltage and duty cycle (varied by changing pulse width and frequency) enable the annealing temperature and time to be optimized during the discharging period to control the sp^2 fullerene-like carbon fraction, resulting in the ability to span the structural spectrum of hard a:C-H with high sp^3 and soft-tensile a:C-H with high abundances of fullerene structures.

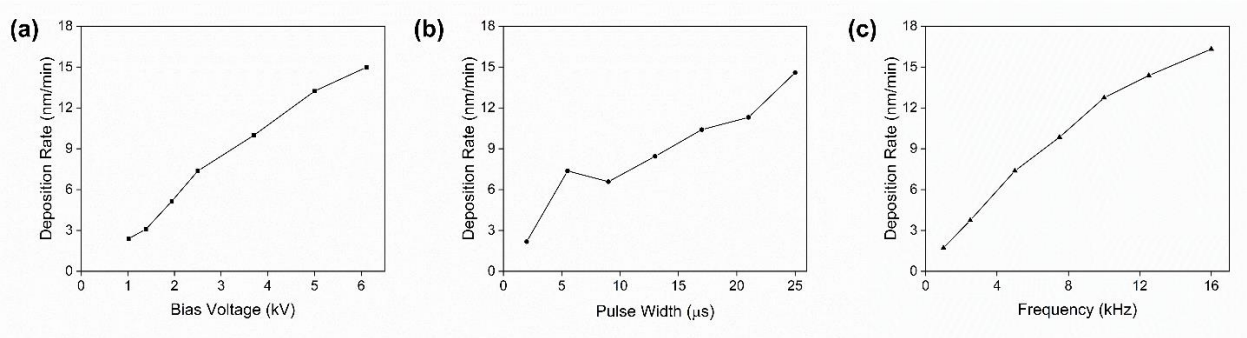

Figure 40*: Deposition rate of single-layered amorphous carbon thin films versus (a) bias voltage, (b) pulse width and (c) frequency are shown.*

5.2.2 Structural characterization of single-layered thin films

Raman spectroscopy has been reported to reveal subtle microstructural changes in carbon films. Typical Raman spectra on a-C:H films are characterized by a G (graphitic) band around 1550 cm^{-1} and a D (disorder-induced) band around 1380 cm^{-1}, originating in the size, distribution and breathing modes of sp^2 sites [139]. While the Raman scattering from sp^2 sites is 50 times stronger than sp^3 [140], qualitative trends in sp^3/sp^2 can still be inferred [141]. Figure 31 shows fitting an example background-subtracted Raman spectrum to D and G peaks for one of the thin

film samples. We observe good fits for all Raman spectra (R-squared values ~ 0.999) using the conventional method of fitting only for D and G bands.

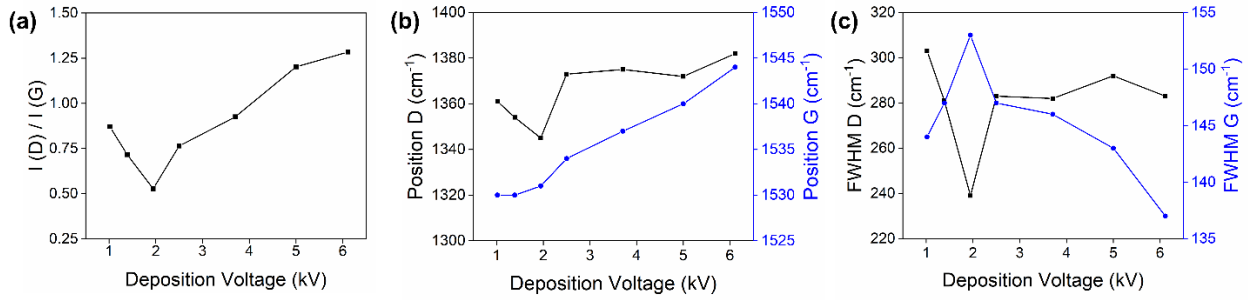

Figure 41*: Fitting Raman spectra acquired on single-layered amorphous carbon films as a function of deposition voltage plotted versus (a) I(D)/I(G), (b) D and G positions, and (c) D and G FWHM values are shown.*

Figure 41 shows Raman spectroscopy measurements on single-layered films as a function of the deposition voltage. The I(D)/I(G) value first decreases from 0.87 to 0.52 as the voltage is increased from 1.01 kV to 1.94 kV. At voltages above 1.94 kV, the I(D)/I(G) ratio monotonically increases up to 1.28. Correlatedly, the G-peak position stays at 1530-1531 cm^{-1} for voltage values from 1.01 to 1.94 kV and then increases slightly up to 1544 cm^{-1}. Taken together, the trends in I(D)/I(G) ratios [142] and G-peak [143] values suggest that maximizing sp^3 contribution to the film structure requires an optimal voltage. The D-peak position first decreases from 1361 cm^{-1} to 1345 cm^{-1} as the voltage increases from 1.01 to 1.94 kV, becomes constant at 1373 - 1375 cm^{-1} for voltage values from 2.50 to 5.00 kV and rises slightly to 1382 cm^{-1} at a voltage of 6.11 kV. This reveals that the overall structural disorder, smaller aromatic rings and ordered aromatic rings first decrease for voltages of 1.01 – 1.94 kV and then increase from 2.50 – 6.11 kV [139]. The G-FWHM values increase from 144 to 153 cm^{-1} as voltage is increased from 1.01 to 1.94 kV and

then decreases monotonically to 137 cm^{-1} at 6.11 kV. The trends in G-FWHM values suggest sp^2 disorder is maximum at voltage of 1.94 kV [143]. For voltage values above 1.94 kV, we suggest that the ion bombardment from increasing bias voltage is strong enough to raise the substrate temperature and contribute to graphitization of film structure (some sp^3 fraction gets converted to sp^2). These results are consistent with other studies in literature relating overall reduction in the films' bonded hydrogen content as the annealing temperature is increased [84] since increasing the bias voltage is analogous to increasing the films' annealing temperature.

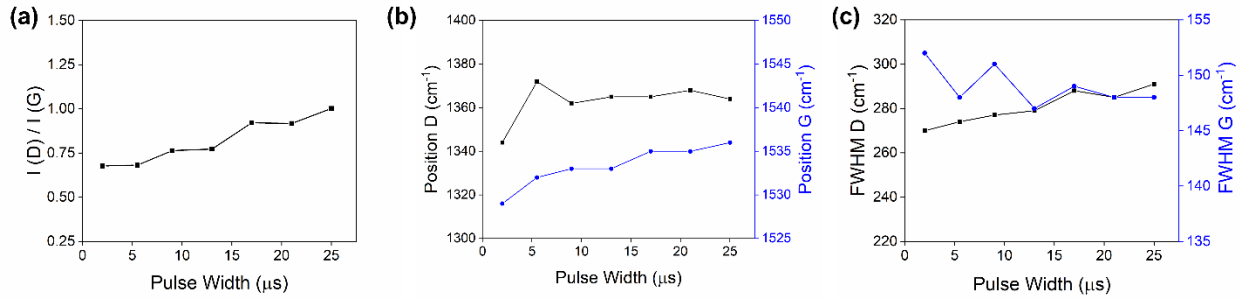

***Figure 42**: Fitting Raman spectra acquired on single-layered amorphous carbon films as a function of pulse width plotted versus (a) I(D)/I(G), (b) D and G positions, and (c) D and G FWHM values are shown.*

Duty cycle or the plasma on-off time ratio was varied by independently changing pulse width and frequency, akin to increasing the annealing time at constant bias voltage (or annealing temperature). Figure 42 shows Raman spectroscopy measurements on single-layered films as a function of the pulse width. The I(D)/I(G) value increases from 0.68 to 1.00 as the pulse width is increased from 2 to 25 μs. Correlatedly, the G-peak position increases slightly from 1529 cm^{-1} up to 1536 cm^{-1}. Taken together, the trends in I(D)/I(G) ratios and G-peak values suggest that sp^3 contribution to the film structure increases as pulse width is increased. The D-peak position peaks to 1372 cm^{-1} at a pulse width of 5.5 μs and stays nearly the same for pulse width values from 9 to

25 μs. This reveals that the contribution of overall structural disorder, smaller aromatic rings and ordered aromatic rings to the film structure is maximum at 5.5 μs. The G-FWHM values showing a small decreasing trend with increasing pulse width, suggesting sp^2 disorder is decreasing.

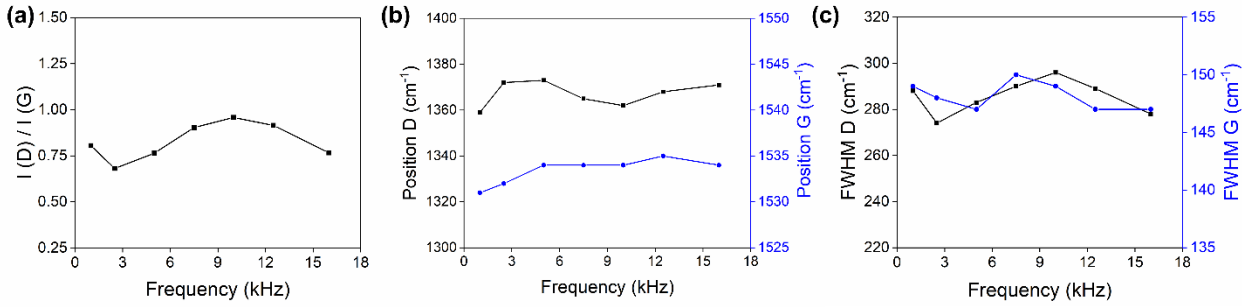

***Figure 43**: Fitting Raman spectra acquired on single-layered amorphous carbon films as a function of frequency plotted versus (a) I(D)/I(G), (b) D and G positions, and (c) D and G FWHM values are shown.*

Figure 43 shows Raman spectroscopy measurements on single-layered films as a function of the frequency. The I(D)/I(G) value increases from 0.68 to 0.95 as the frequency is increased from 2.5 to 10 kHz and decreases to 0.77 with further increase up to 16 kHz. Correlatedly, the G-peak position increases slightly from 1532 cm^{-1} up to 1535 cm^{-1}. Taken together, the trends in I(D)/I(G) ratios and G-peak values suggest that sp^3 contribution to the film structure peaks at an optimal frequency value. The D-peak position first decreases from 1372 cm^{-1} to 1362 cm^{-1} as the frequency increases from 2.5 to 10 kHz and rises back up to 1371 cm^{-1} at a frequency of 16 kHz. This reveals that the overall structural disorder, smaller aromatic rings and ordered aromatic rings first decrease for frequencies of 2.5 – 10 kHz and then increases from 12.5 to 16 kHz. The G-FWHM values are consistently between 147 – 149 cm^{-1} suggesting sp^2 disorder is nearly the same irrespective of frequencies.

5.2.3 Mechanical properties of single- and multi-layered films

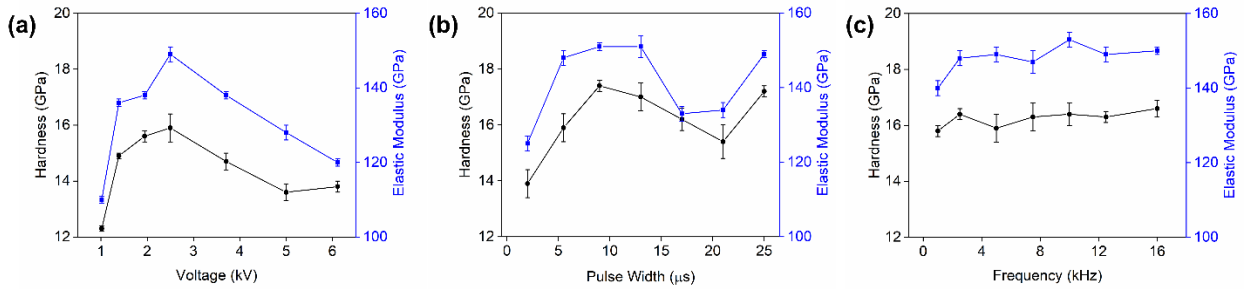

Figure 44*: Hardness and elastic modulus of single-layered amorphous carbon thin films versus (a) bias voltage, (b) pulse width and (c) frequency are shown.*

Figure 44 summarizes mechanical properties of single-layered thin films as a function of the deposition voltage, pulse width and frequency. The elastic recovery %, R is defined as $((h_{max} - h_{res}) \times 100)/h_{max}$, where h_{max} and h_{res} are the maximum indentation depth and residual depth [144]. R for all these films was calculated to be 65 – 70 % from load-displacement curves. Figure 44(a) shows a peak in H and E values corresponding to a voltage value of 2.5 kV, and this peak coincided with highest sp^3 fraction, highest sp^2 disorder and overall lowest disorder from Raman data shown in Figure 41. Figure 44(b) shows a peak in H and E values at a pulse width of 9 μs correlating with intermediate sp^3 contribution and highest overall disorder while the sp^2 disorder was nearly the same based on Raman data from Figure 42. Figure 44(c) shows that varying the frequency doesn't alter the mechanical properties a lot, but it is still worth pointing out that a peak in H and E occurred at a frequency of 2.5 kHz, and was correlated with highest sp^3 order, lowest sp^2 disorder and highest overall disorder as seen from Figure 43. The trends in H and E with varying bias voltage are consistent with the Raman data.

H/E ratio represents resistance of a material relative to elastic deformation, while H^3/E^2 represents it's resistance to plastic deformation [145,146]. These ratios have previously been shown to predict wear resistance. Figure 45(a) shows that resistance to elastic deformation is relatively high (as per H/E values) for films grown at voltages less than and up to 1.94 kV, above which it goes down (except for the film grown at 6.11 kV). The resistance to plastic deformation (as per H^3/E^2 values) shows a clear peak at 1.94 kV and then decreases with increasing voltage (except at 6.11 kV). Figure 45(b) shows a concurrent peak in resistance to elastic and plastic deformation at a pulse width of 17 μs, but it is interesting to note that this peak does not correspond to the highest measured mechanical properties in Figure 44(b). Figure 45(c) doesn't show a clear trend in resistances to elastic and plastic deformations due to frequency effect.

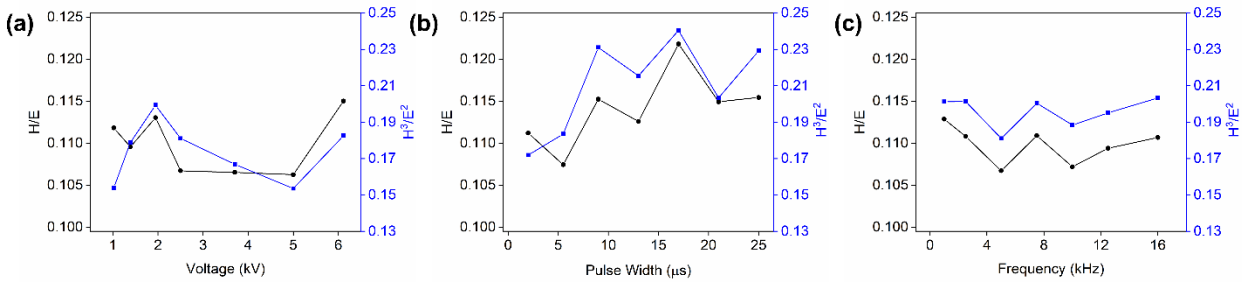

***Figure 45**: H/E and H^3/E^2 of single-layered amorphous carbon thin films versus (a) bias voltage, (b) pulse width and (c) frequency are shown.*

Based on this preliminary structure and mechanical properties characterization, we identified that voltage and pulse width seem to have a profound effect on film microstructure, while frequency is a less important parameter. Figure 46 compares mechanical properties of multilayered thin films to those of constituent single-layered films. Figure 46(a) clearly shows that multilayering can vary the film hardness from + 2.6 % to – 5.1 %, meaning high hardness can be

preserved while pursuing enhancing other properties. Figure 46(b) shows that elastic modulus is much more sensitive to multilayering (between + 1.5 % and – 24.6 %). Since elastic modulus is a proxy for film density, these results suggest that multilayering may introduce less dense regions at the interfaces. Figure 46(c) and (d) shows that multilayering increases both H/E and H^3/E^2 values as much as + 26.1 % and + 59.8 % as compared to the corresponding best performing single-layered films.

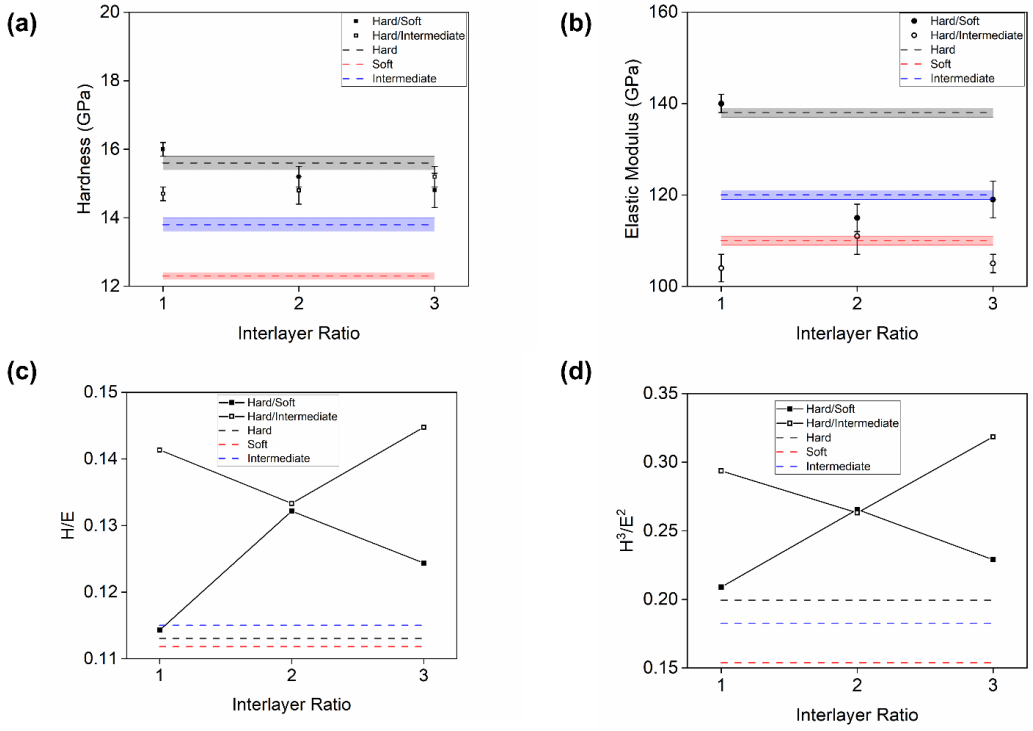

***Figure 46**: (a) Hardness and (b) elastic modulus of multi-layered amorphous carbon films are represented by the data points while the bands show corresponding values for single-layered films. (c) H/E and (d) H^3/E^2 of multi-layered amorphous carbon films are represented by the data points while the bands show corresponding values for single-layered films.*

5.2.4 Scratch testing – coefficient of friction

Figure 47 shows coefficient of friction (CoF) behavior for single-layered and multi-layered films as the diamond tip was scratched across samples for 10 µm at 3, 6 and 10 mN. While the data for 3 mN scratches was noisy possibly due to surface roughness effects, CoF data at 6 and 10 mN was very repeatable. For the single-layered films, the hard and intermediate samples had a lower CoF than the soft sample. Multilayering clearly reduced the CoF irrespective of the recipe used. For the hard-soft system, alternating 20 nm layers of hard-soft layers showed the best friction resistance. For the hard-intermediate system, alternating 10 nm layers of hard and intermediate layers showed best friction resistance.

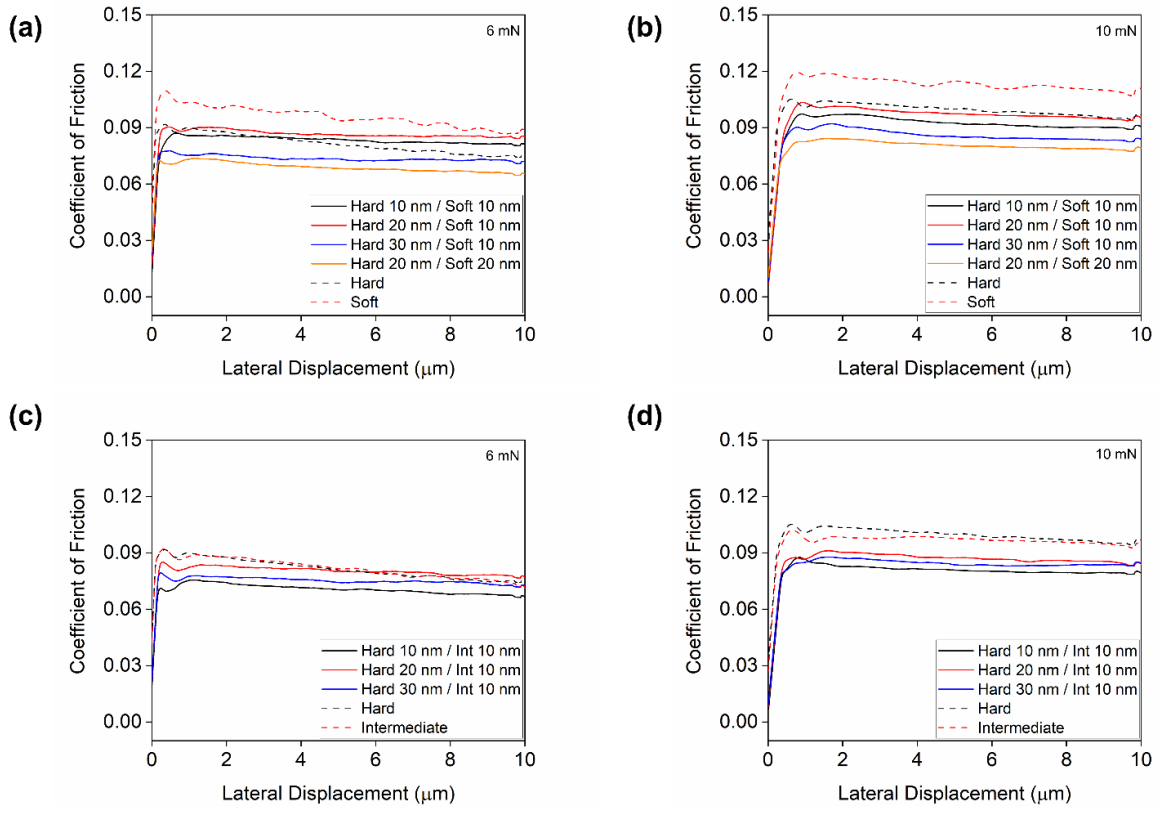

***Figure 47**: Coefficient of friction measurements on hard/soft multilayer stacks at (a) 6 mN and (b) 10 mN and those on hard/intermediate multilayers at (c) 6 mN and (d) 10 mN are shown.*

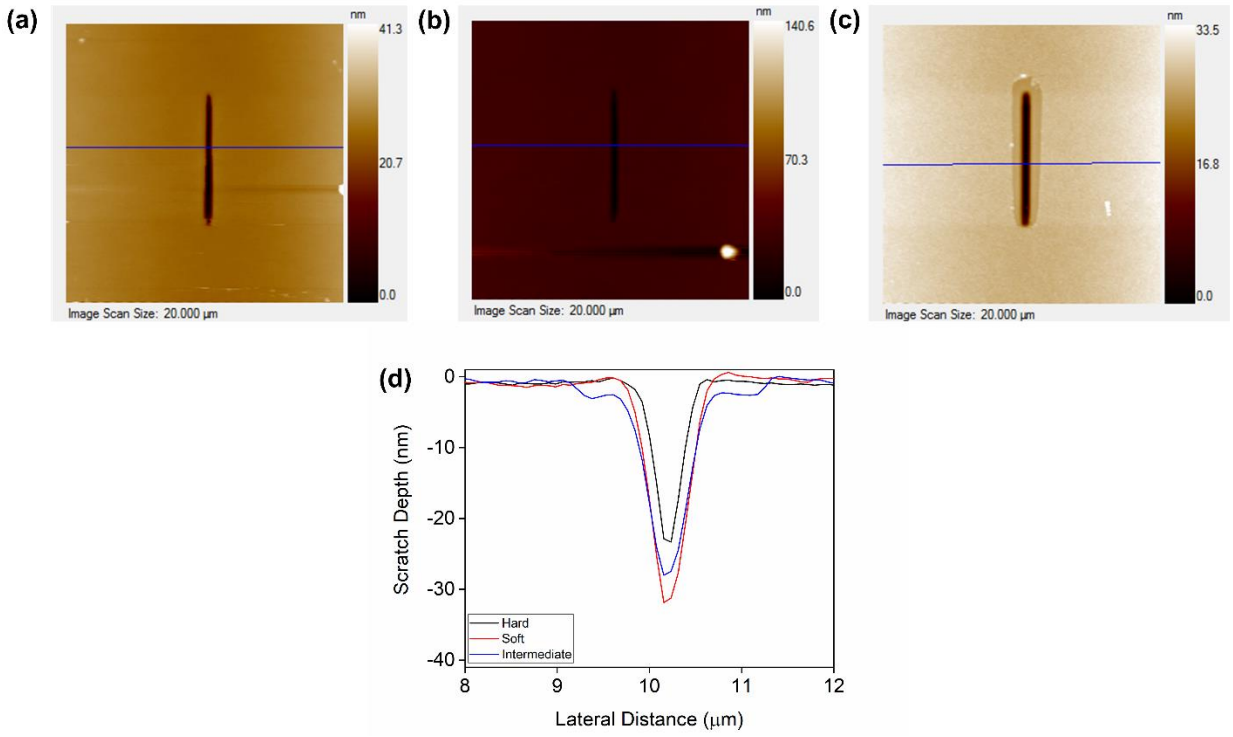

***Figure 48**: Post-scratch imaging at 10 mN peak load on single-layered thin films with hardness values of (a) hard, (b) soft and (c) intermediate are shown. (d) compares scratch profiles of the three samples along the blue line shown in (a), (b) and (c).*

Figure 48 shows the SPM images of scratches made on the single-layered films at peak load of 10 mN. The hard film shows the lowest scratch depth amongst the single-layered films and can be directly correlated to the CoF and hardness behaviors. Figure 49 shows SPM images of scratches made on hard-soft multilayered film system at peak load of 10 mN. Only the film grown with alternating 20 nm interlayers shows a better scratch resistance than the hard film, while other films show scratch resistance worse than the single-layered hard film. This multilayered film also has the lowest CoF and highest hardness of all. Figure 50 shows SPM images of scratches made on hard-intermediate multilayer system at peak load of 10 mN. All of these films show worse scratch resistance, better CoF and lower hardness than the hard film. It is worth pointing out that

the scratch depths reported here are true ones measured upon recovery after the actual scratch tests. Our results indicate that while the CoF can be consistently lowered by multilayering, the scratch resistance (and hence the wear resistance) seems to be dictated by the material's response to mechanical deformation (or in other words, hardness).

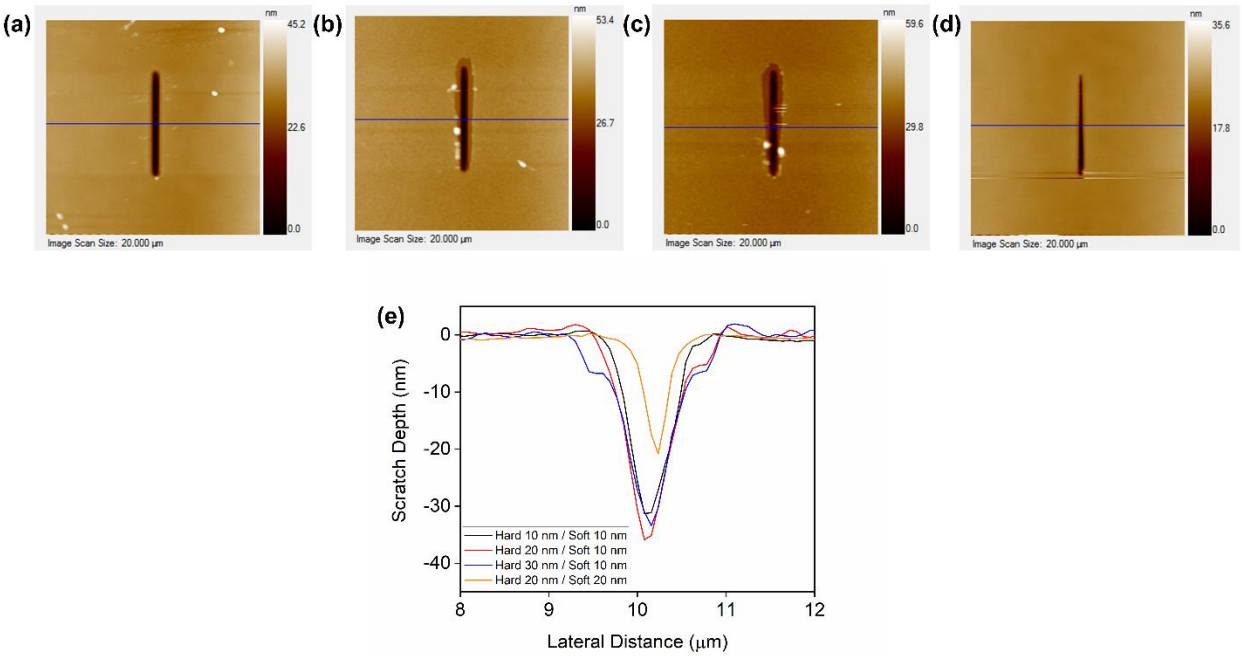

***Figure 49**: Post-scratch imaging at 10 mN peak load on hard/soft multi-layered stacks with interlayer ratio of (a) 1:1, (b) 2:1, (c) 3:1 and (d) 2:2 is shown. (e) compares scratch profiles of the three samples along the blue line shown in (a), (b), (c) and (d).*

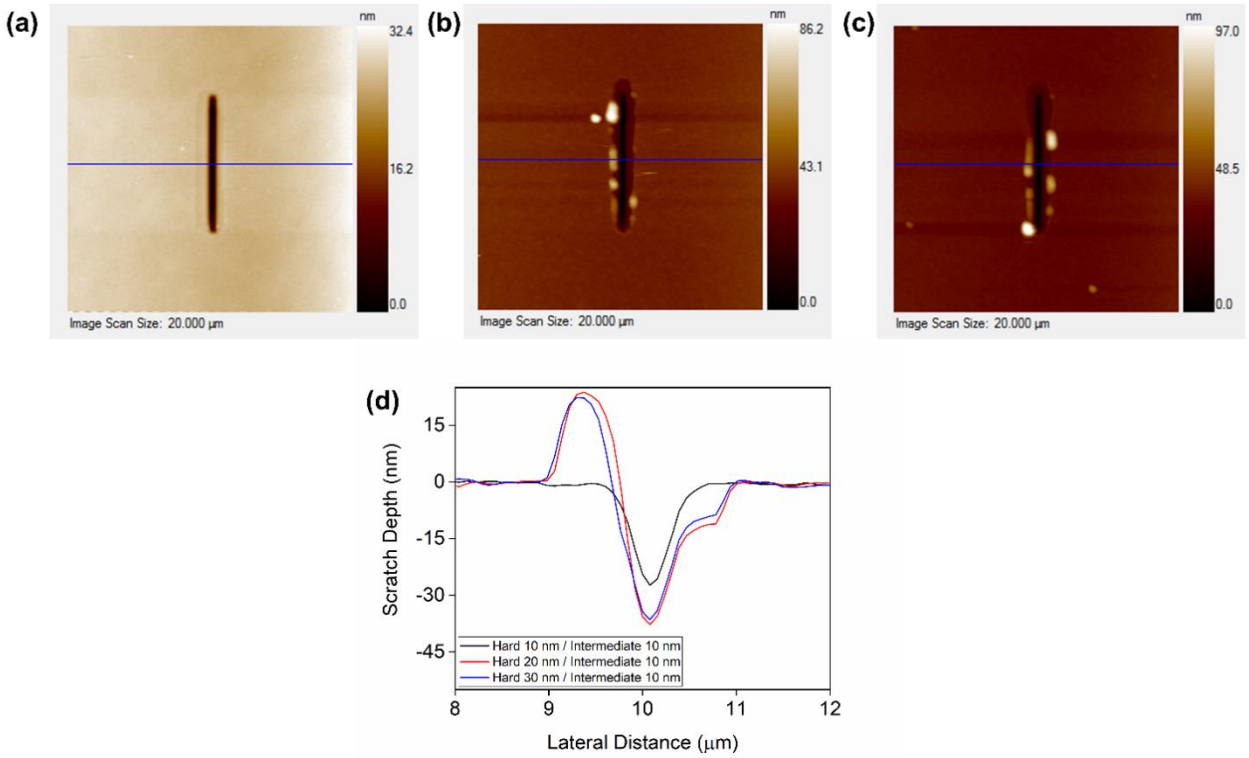

***Figure 50**: Post-scratch imaging at 10 mN peak load on hard/intermediate multi-layered stacks with interlayer ratio of (a) 1:1, (b) 2:1, and (c) 3:1 is shown. (d) compares scratch profiles of the three samples along the blue line shown in (a), (b), and (c).*

5.3 Summary

To summarize, we investigated the structure, mechanical properties and scratch behavior in single-layered and multilayered amorphous carbon thin films made by plasma immersion ion implantation-based plasma enhanced chemical vapor deposition. Varying the applied bias voltage and pulse width could improve the elastic modulus and hardness in single-layered films by as much as 35 and 30 % respectively, while mechanical properties were independent of pulse frequency within experimental uncertainty. Raman microscopy on single-layered films showed that the maxima in mechanical properties due to bias voltage coincided with highest sp^3 fraction, highest sp^2 disorder and overall lowest disorder. The maxima in mechanical properties due to pulse width

correlated with intermediate sp^3 contribution and highest overall disorder while the sp^2 disorder was nearly the same. Nanoindentation and scratch-testing showed that the scratch volume was strongly correlated to the hardness and multilayering preserved high hardness and improved friction behavior irrespective of the recipe.

Chapter 6 Case study: Investigation of shorter lifetime of upper Cu weld wheels in an industrial mash seam welding setup

This chapter is adapted from the manuscript under preparation: S. V. Muley et al. "Case study: investigation of shorter lifetime of upper Cu weld wheels in an industrial mash seam welding setup". A.O. Smith Corporation is a Milwaukee-based company that makes welded pipes for industrial heaters, amongst a multitude of other products. I along with my supervisors, Drs. Bruce Krakauer and Jon McCarthy investigated the failure mode of upper copper weld wheels in an industrial production line which had a much shorter lifetime than the lower electrode.

6.1 Background

Resistance spot welding is a widely used industrial technique to join thin metal sheets, either by intermittent spot welds or continuous seam welds [147,148]. The basic process involves clamping the weld pieces between two highly conductive electrodes and passing a large current of the order of tens of kilo-Amperes. Due to the combined action of pressure and high current, local weld nuggets form at the faying surfaces. In seam welding setups, electrodes in the form of either wheels or rollers drive the work pieces through the welder continuously. The process of welding occurs while the weld assembly is stationary by passing current and during the time the weld piece is being moved to arrive at a fresh section to be welded, no current is passed. The electrode material is chosen such that it has high electrical and thermal conductivities along with appropriate resistance to hot mechanical deformation. This is because (1) electrodes need to simultaneously transmit force and current through the work pieces, and (2) excess heat needs to be dissipated to limit heat-affected zone to ensure good weld quality, achieved in practice by internal water cooling of electrodes. Class 2 copper alloys are commonly used in seam welding setups [149].

Irrespective of the welding technique employed, weld productivity is driven by the ability to produce welds of acceptable quality over an extended production run, with minimal interruption [150]. This ability is primarily controlled by electrode life, defined as the number of welds that can be made before the weld nugget diameter falls below acceptable limits. Electrode degradation is a recurring and actively researched problem in industry because a short electrode lifetime leads to significant downtime [151]. In Chan's study of resistance spot welding hot dipped galvanized steel with TiC metal matrix composite coated electrodes, the electrode lifetime was affected by several process parameters such as weld force, weld electrode material properties, operating current, water cooling efficiency, electrode geometry, and weld times [152]. Most of the degradation modes led to an increase in contact radius at the electrode-sheet interface, causing a progressive decrease in current density until it was insufficient to create a weld nugget [152]. The degradation mechanisms are complex and proceed by one or a combination of plastic deformation, electrode wear and electrode-workpiece interactions [153]. Previously, numerous studies have focused on electrode wear due to spot welding of Zn-coated stainless steels [154–157], Al alloys [158–160] and Mg alloys [161]. Evaluating electrode lifetime and correcting for process inefficiencies requires a thorough understanding of the process.

While there is published literature on the degradation mechanisms of electrodes for spot welding as summarized above, the same is not true for a similar technique called mash seam welding. Mash seam welding can rapidly manufacture a continuous weld seam by means of overlapping resistance spot welds, and the weld overlap in mild steels can be mashed to about 1.5 times the sheet thickness while passing through the rollers [148]. This technique is used where straight welds are possible and flush welds are needed, such as manufacturing of pipes. We present

a case study about comparatively faster degradation rate of the upper wheels as compared to lower weld wheels in an industrial mash seam welding setup to weld mild steel. We performed failure analysis on a spent class 2 copper electrode by employing metallography, composition analyses and nanoindentation to reveal the degradation mechanism.

6.2 Materials and methods

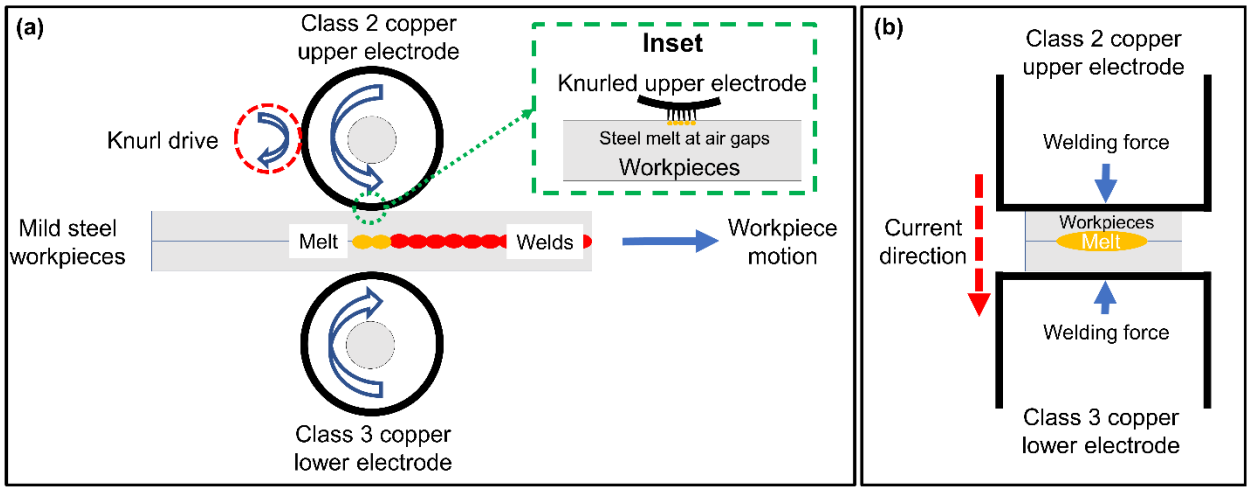

Figure 51*: Schematic shows (a) side-view and (b) end-on view of the mash seam welding setup. Inset in (a) shows a magnified view of electrode-workpiece surface contact. None of the drawings are to scale.*

The production line referred to in this study employs class 2 copper upper and class 3 copper lower weld wheel electrodes to mash seam weld mild steel pipes, as shown in Figure 51. Class 2 copper is a superior resistance welding electrode material used in high production operations. One of its types is a specially heat-treated Cu-Cr alloy that is first cast, then hot forged to create a 12” diameter by 1” thick disc with a homogeneous microstructure and finally machined to the required dimensions. With usage, the upper class 2 copper wheel was observed to degrade much faster than the lower class 3 copper wheel. Our initial assessment pointed towards electrode-workpiece interactions under operating conditions, causing the amount of current that could be passed through

the electrodes to drop. The upper wheel needed frequent redressing, meaning its face was mechanically machined back to its original geometry, thereby causing significant downtime and production losses.

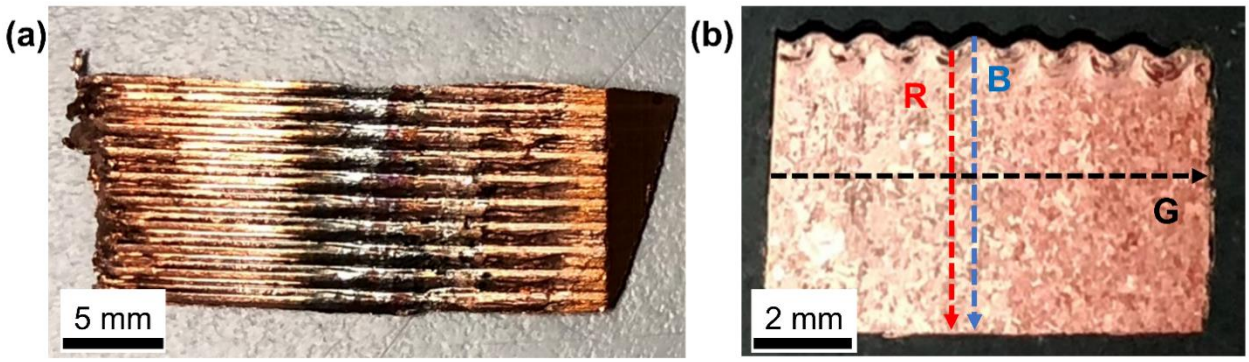

***Figure 52**: (a) View normal to the welding surface of the weld wheel, showing the dark band (DB) that represents the degradation of the weld wheel surface, (b) View parallel to the axis of the weld wheel, resulting in a cross-sectional view of the dark-band (CS). Series of indents were made along lines B, R and G.*

We performed failure analysis on a spent class 2 copper without redressing it and cut into two parts with a bandsaw. One cut resulted in a view normal to the welding surface of the weld wheel. The welding surface exhibited a dark band (DB) that represents the degradation of the weld wheel. The second cut resulted in a view parallel to the axis of the weld wheel, resulting in a cross-sectional view of the dark band (CS). Both views are shown in Figure 52. The CS surface was polished down to 0.5 µm roughness and etched for 7 seconds with an etchant solution of 25 ml NH_4OH + 25 ml H_2O + 20 ml H_2O_2 (3%). A Motic BA310 optical microscope (OM) and a Hitachi TM3000 desk top scanning electron microscopes (TSEM) (beam energy – 15 kV) were used. The sample CS was cloth-polished for nanoindentation studies with 0.04 µm colloidal silica solution

to obtain surface roughness of the order of tens of nanometers, as measured by Zygo New View 6300 white light interferometry. Elemental spectral images of DB and CS samples were collected by EDS measurements made in a Zeiss 1530-LEO SEM. The Zeiss SEM is equipped with a Thermo NORAN System 7 analyzer and 30mm^2 silicon drift EDS detector. Elemental X-ray spectra and images were collected at an electron beam energy of 15 kV, working distance of ~ 9 mm and magnifications ranging from 150X to 500X. In each scanned area, a secondary electron SEM image was collected with the Zeiss SE2 detector.

A Hysitron TI950 nanoindenter was first calibrated via load-controlled measurements on a standard quartz sample with peak loads of 0.015 and 0.05 N. The CS sample was glued onto the instrument stage with Loctite 460 instant adhesive and indented via a high load (HL) Berkovich tip in the nanoindenter to map changes in material's hardness (H). Load-controlled measurements were made with a basic trapezoid function that ramped up to a pre-selected peak load over 5 seconds, held at peak load for 2 seconds and unloaded over 5 seconds. Optimal load range was found to be between 0.02 - 0.5 N by indenting at different peak loads. A series of 25 indents was made along the G line shown in Figure 52(b) at a peak force of 0.5 N. A series of 50 indents spaced 0.12 mm apart were made along the blue lines B and R at a peak load of 0.5 N. For more localized probing of samples, two series of 40 × 3 indents spaced 0.05 mm apart were made along lines spaced 1 mm beside the lines (R and B (Figure 52(b)) at peak loads of 0.05 N. The load-displacement characteristics during indentation experiments were recorded by Hysitron Triboscan software. The H values were calculated by fitting the unloading curves to a power law, as per the Oliver-Pharr method [99]. H values reported in this study are as per the Meyer formula, $H =$

$\frac{F}{A_c}$ [100]. Optical images of indent distribution and shape were acquired at magnifications of 5X, 10X and 20X.

6.3 Results

6.3.1 Visual inspection by optical microscopy and table-top SEM

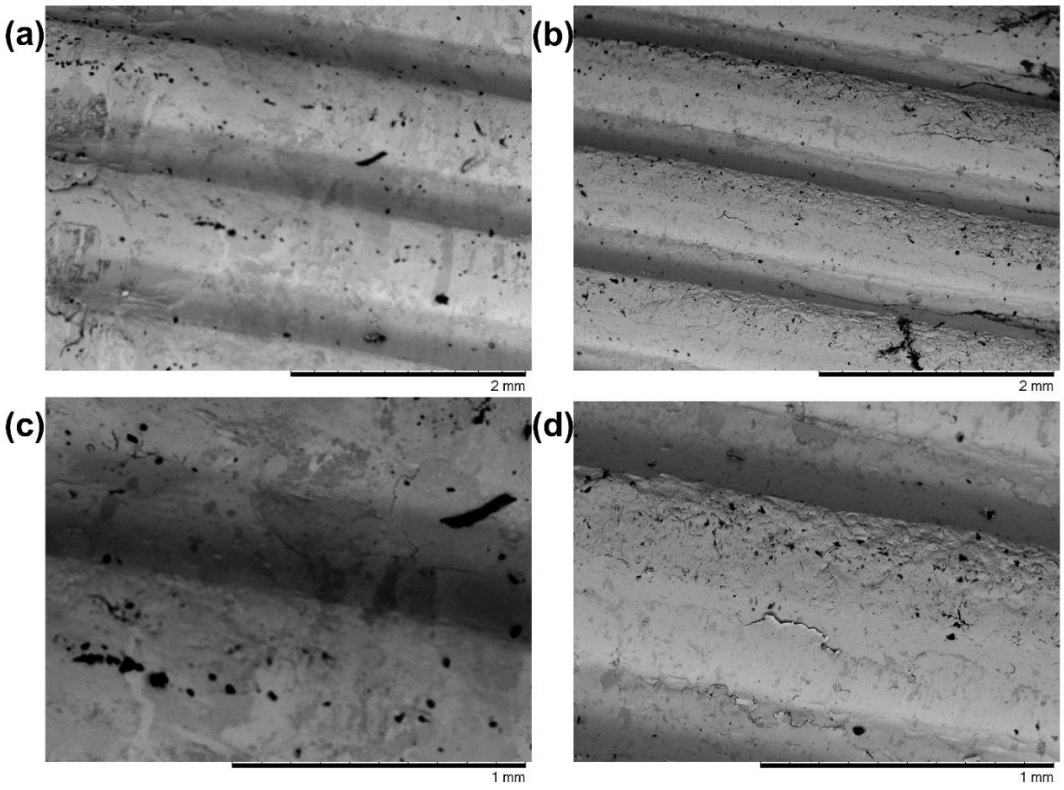

Figure 53*: Top-view TSEM on the DB sample (a) dark band at 40X, (b) dark band free region at 40X, (c) dark band at 100X, and (d) dark band free region at 100X are shown.*

Top view TSEM images on DB sample in Figure 53 show a difference in surface contrasts at 40X (Figure 53(a), (b)) and 100X (Figure 53(c), (d)) for dark band (Figure 53(a), (c)) and no dark band (Figure 53(b), (d)). Figure 54 shows TSEM imaging on the CS sample. Figure 54(a) shows a clear contrast at the repeating knurled surface (tens of microns in length), which suggests

presence of the dark band. Up to approximately 1 mm depth from knurled surface, the microstructure represents a heat-affected zone resulting from welding. The bottom part of Figure 54(a) shows polycrystalline copper, like copper microstructure seen 6 mm below the knurled as observed in Figure 54(b). These observations were further supported by OM (not shown).

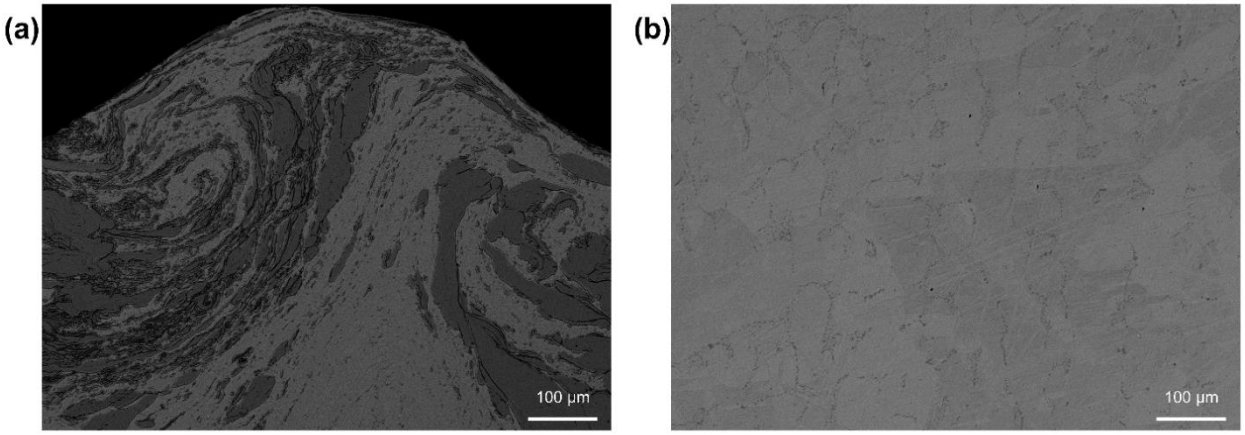

Figure 54*: TSEM images on CS sample at (a) dark band region near surface and (b) dark band region 6 mm below surface are shown.*

6.3.2 Chemical analysis by SEM-EDS

Chemical analysis by EDS was accomplished by both qualitative (suitable for rough surfaces like sample DB) and quantitative analyses (for the polished flat surface of sample CS). Two common methods of qualitative analysis are: 1) acquiring a X-ray spectra at selected points (or small area scans) on the sample and using peak identification software to identify elements present in the sample, and 2) acquiring X-ray spectral images over a scanned region to identify the distribution of elemental coverage in a region. On the other hand, quantitative analysis of the composition requires performing matrix correction calculations to determine the actual concentrations of elements in the sample, in addition to processing X-ray spectrum at each point.

A requirement of quantitative analysis is that the specimen be polished metallurgically flat (<0.1μm), and that the excitation conditions and the sample-to-detector geometry be precisely known and remain constant. In both methods, the relative intensities of elemental peaks in point spectra or X-ray map images were used to identify significant chemical phases in the samples. For sample DB, which has a rough surface, qualitative analysis methods were performed, while for sample CS, we were able to obtain quantitative results.

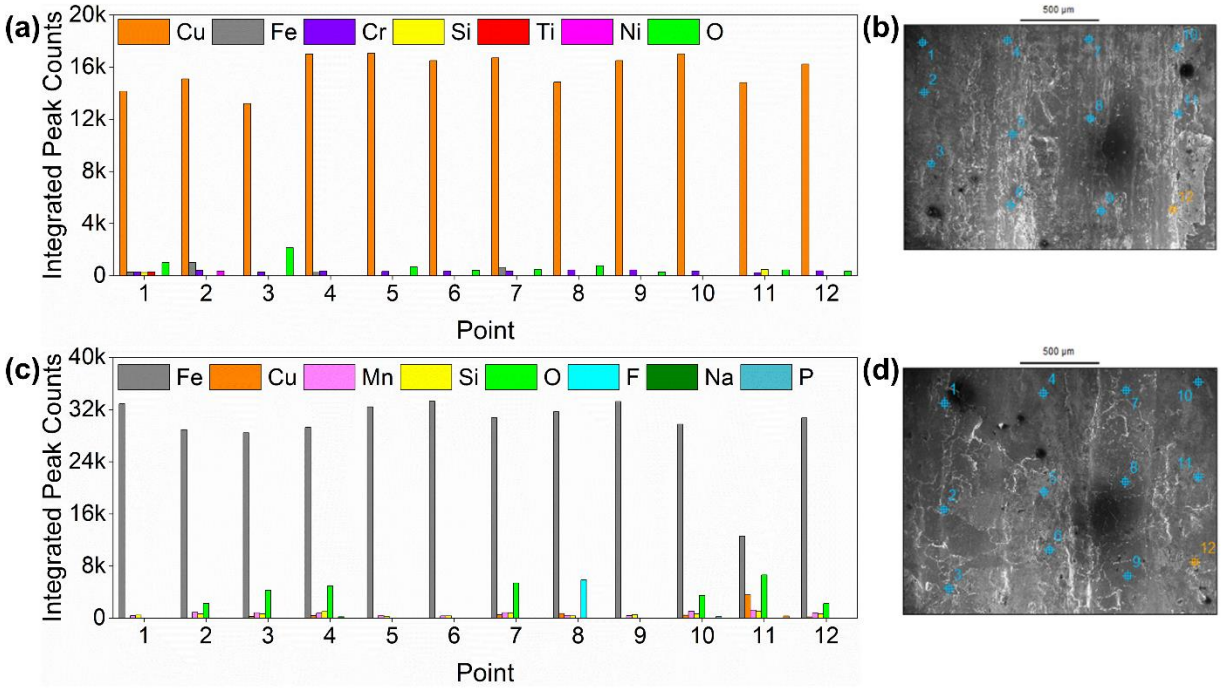

Figure 55*: The spot EDS measurements of elemental intensities obtained for two different counting times for the same areas are shown in (a) and (c). (b) and (d) show SEM images and the points from which data was collected. Some points show additional elements, that are surface contaminants. The Cu and Fe intensities clearly dominate in (a) and (c) respectively, suggesting that in the dark band region the surface is covered in a layer of steel.*

Figure 55(a) and (b) show qualitative elemental results of the knurled surface on the sample DB determined by measuring the net elemental peak counts in each spectra from 12 spot EDS measurements on copper areas away from the dark band, and 12 points from the area in the dark band, respectively. In the spot EDS results bar charts, the total counts for each element detected at that point are plotted as separate bars at each point. Each point in the dark band area contains Fe and Mn while each point in the copper area shows Cu and Cr. A minimum detection limit calculation similar to Ziebold's study [162] shows that for the acquisition times used for the spectra, Cr and Mn are just above the detection limits for those elements. Oxygen is seen in many of the point spectra and is likely due to oxidation of the sample during and after sample preparation. In addition, minor amounts of F, Si, P, Ti and Ni are seen at various points. These elements are most likely contaminants on the surface. As clearly seen from Figure 55(a), the area away from the dark band is primarily Cu and Cr, representing bulk composition of the copper alloy itself. In Figure 55(b), we see that Fe is now the major element with some Mn, which suggests that the dark band is a region covered by steel from the work piece. Using the ratio of the average Cu peak counts from both areas and the known mass absorption coefficient for Cu by Fe, we estimated the average thickness of the steel layer to be 1.2 ± 0.3 μm. As shown in Figure 55(b), the Fe counts vary significantly, so we also expect the steel film thickness varies over the area. This is confirmed by Figure 56 where the elemental x-ray images for Cu and Fe are shown both separately and overlaid in color tints on the SEM image. There are several regions where the Cu is the dominant element. An area calculation of the Fe x-ray image finds ~80% of the total image area is covered with the steel layer.

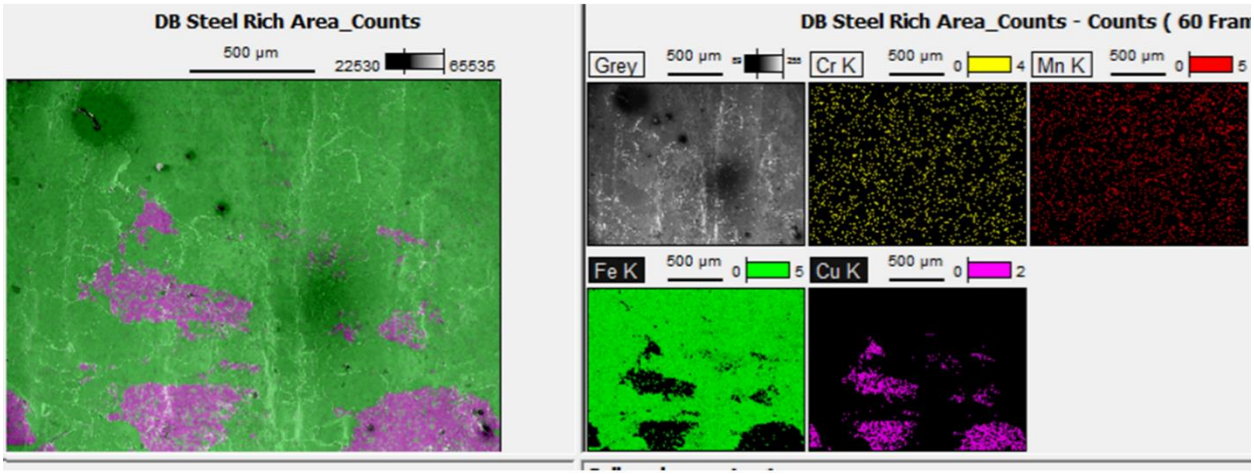

***Figure 56**: Software screenshot shows EDS elemental images for the dark band area, with Cu and Fe images (Fe – green tint, Cu – purple tint) overlaid on the SEM image. The Fe overlays >80 % of the total area, suggesting the steel coating has variable thickness in this region.*

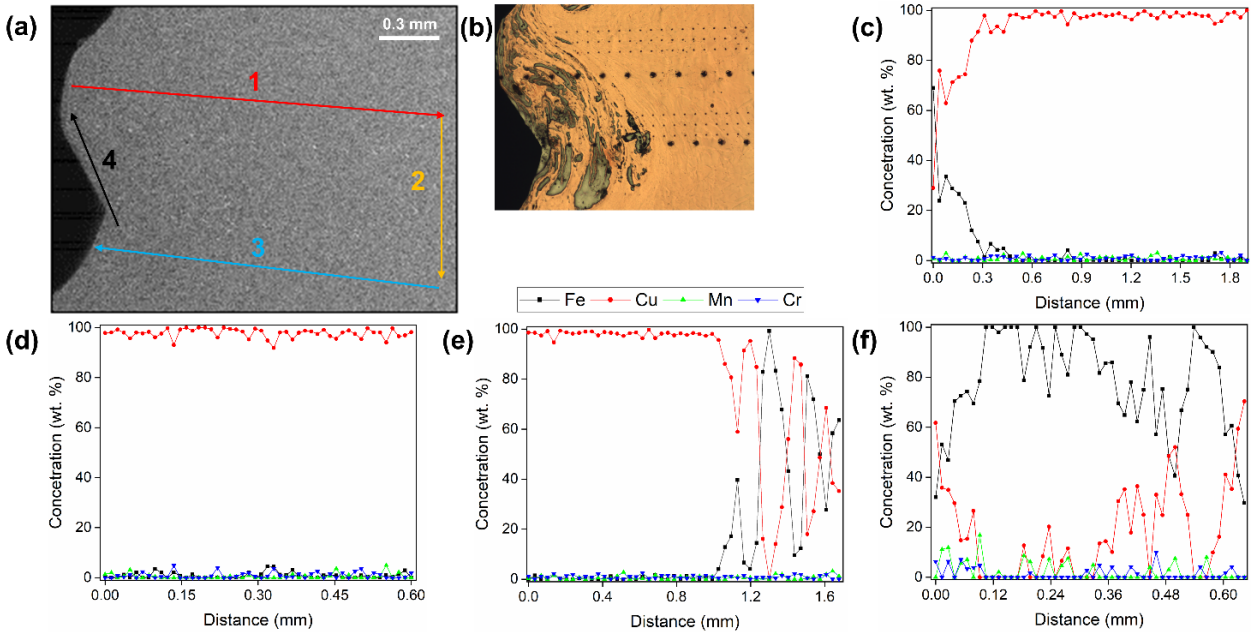

***Figure 57**: EDS linescans were acquired along the arrows shown in (a) SEM image and (b) corresponding optical image appropriately scaled are shown. (c), (d), (e) and (f) represent elemental composition along linescans 1, 2, 3 and 4 respectively while the symbols representing different elements are shown as legends. Distance is 0 mm at the beginning of each arrow.*

Since the sample CS is polished very flat (<0.1 μm), it was possible to obtain quantitative results from spectra and to obtain quantitative elemental line-scans to determine the composition and distribution of copper and steel areas within the electrode itself. Figure 57 shows composition profiles (in weight percent) along the four linescan directions shown in Figure 57(a). Scaling of the optical image in Figure 57(b) with respect to SEM image in Figure 57(a) is exact and can reasonably visualize the contrast in various regions in the Cu wheel. Linescan 1 captures composition perpendicular to the peak to a depth of ~ 1.9 mm (all Cu, some Cr), linescan 2 is deep inside the Cu wheel (all Cu, some Cr), linescan 3 is going back up the wheel to the valley (all Cu up to 0.95 mm, primarily Fe and Cu mixing for distances 0.95 – 1.54 mm and all Fe for distances 1.54 – 1.66 mm), linescan 4 captures composition along the knurled wheel (all Fe, very small Mn at a distance of 0.18 mm). A quantitative analysis was done on spectra from 19 individual points collected from the region deep in the sample along linescan 2. The wt. % results for Cu and Cr are 99.4 ± 0.8 and 0.7 ± 0.5 respectively, and 0.0 for Fe and Mn. This is in good agreement manufacturers reported composition for the class 2 material.

Additional insight is gleaned from Figure 58, which shows spectral imaging and subsequent phase analysis on SEM image, Figure 58(a). This analysis reveals 2-D distribution of two major phases C1 (major element – Cu, minor elements – Fe, Cr) and C2 (major element – Fe, minor elements – Cu, Al, Si). Clearly, there is evidence of steel from the workpiece mixing with the copper electrode. Even though some Cu is seen in phase C2, we suggest there isn't a Fe-Cu chemical phase. Instead, there seem to be steel inclusion mixed into the bulk copper. The transition from Fe to Cu is sharp, occurring in about 15 μm.

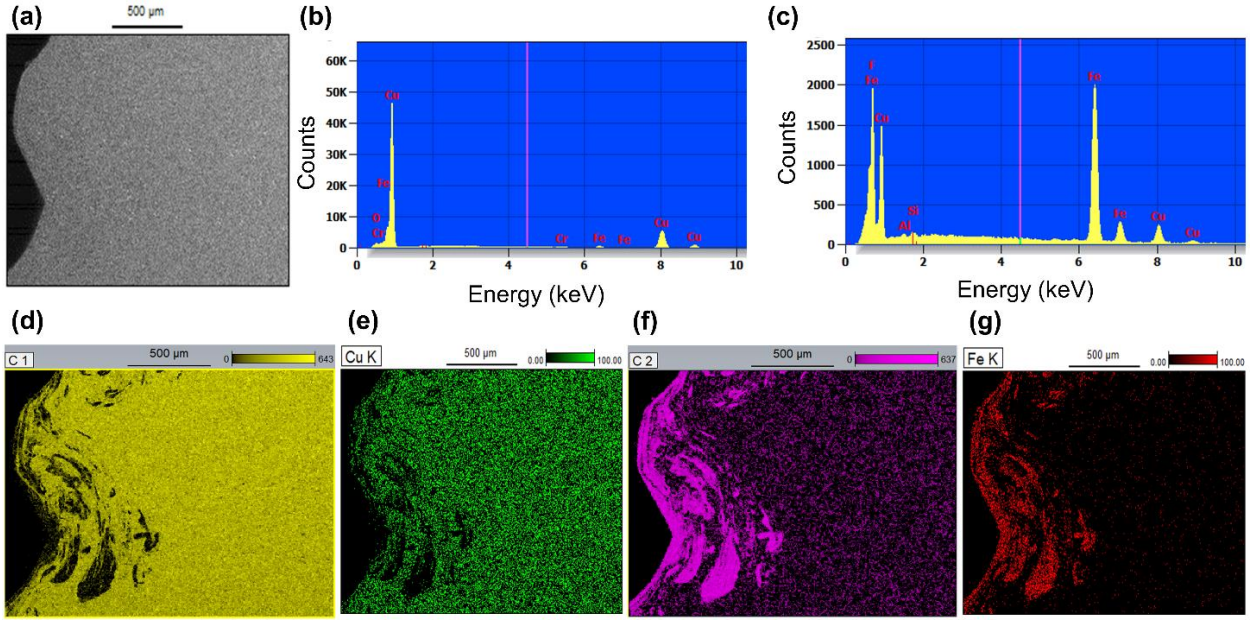

***Figure 58**: (a) Spectral imaging was acquired on the SEM image shown. (b) EDS spectrum of (d) phase C1 paired with (e) Cu map (c) EDS spectrum of (f) phase C2 paired with (g) Fe map.*

6.3.3 Hardness mapping by nanoindentation

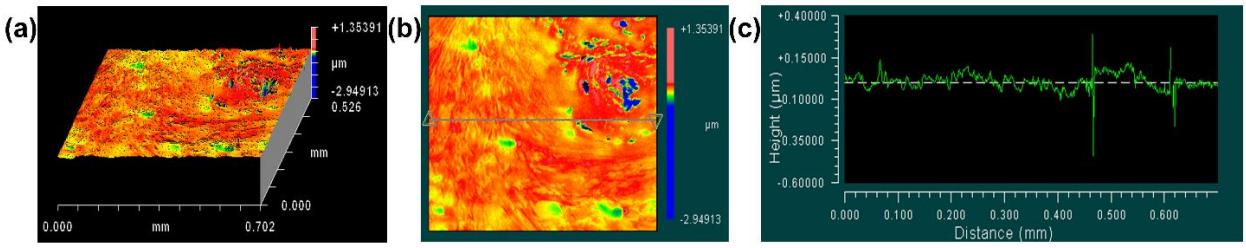

***Figure 59**: (a) A 3D surface plot of sample CS shows a reasonably flat sample post-cloth polishing. (b) 2D projection of (a) is shown. (c) Surface profile along the line in (b) shows a 1D cut with RMS roughness of 0.035 µm.*

Nanoindentation was employed for localized hardness testing with the goal to characterize the steel-copper mixed regions. Surface roughness can affect the reliability of H measurements [159]. Cloth-polishing CS with 0.04 µm colloidal silica solution resulted in a flat and smooth surface as shown in Figure 59. The root-mean-square roughness was ~ 0.035 µm, suggesting that surface

roughness effects on nanoindentation measurements would be negligible if the indent depth is more than 20 times the roughness (0.7 μm). Also, H measurements on metals by nanoindentation are known to show size effects up to indentation depths of a few hundred nanometers [160]. Nanoindentation on the polycrystalline base Cu alloy shows a negligible dependence of hardness values on indentation depth (range 0.65 – 7 μm) for the load range 0.02 – 2 N, meaning our results are not affected by size effects. Next, indentation along line G at 0.5 N was used to establish HG, average value of the base Cu alloy: 1.89 ± 0.06 (3%) GPa. The reported errors are standard deviations over 24 measurements.

Figure 60 and Figure **61** summarize nanoindentation measurements as a means of localized hardness mapping along B and R on sample CS. Figure 60(a) shows optical image of 40×3 smaller indents (spaced 0.05 mm apart from each other) at 0.05 N parallel to but separated by 0.1 mm from B (series of bigger indents at 0.5 N) from distance from edge, D = 0 mm to D = 0.25 mm and Figure 60(b) shows optical image of same smaller and larger indents but at D values ranging from 1.75 to 2.00 mm. Figure 60(c) shows H values for smaller indents at positions B1 (0.1 mm away from B), B2 (0.15 away from B) and B3 (0.20 mm away from B). Figure 60(c) shows a comparison of nanoindentation along B at 0.5 N (open circles) and 0.05 N (solid circles, squares and triangles) at positions B1, B2 and B3. The grey band represents average and error in HG values.

Similarly, Figure 61(a) shows optical image of 40×3 smaller indents (spaced 0.05 mm apart from each other) at 0.05 N parallel to but separated by 0.05 mm from R (series of larger indents at 0.5 N) from distance from edge, D = 0 mm to D = 0.25 mm and Figure 61(b) shows optical image of same smaller and larger indents but at D values ranging from 1.67 to 1.92 mm. Figure 61(c) H values for smaller indents at positions R1 (0.05 mm away from R), R2 (0.10 away from R) and R3

(0.15 mm away from R). Figure 61(c) shows a comparison of nanoindentation at 0.5 N (open circles) and 0.05 N (solid circles, squares and triangles) at position R1 as shown in Figure 61(a). The grey band represents average and error in H_G values.

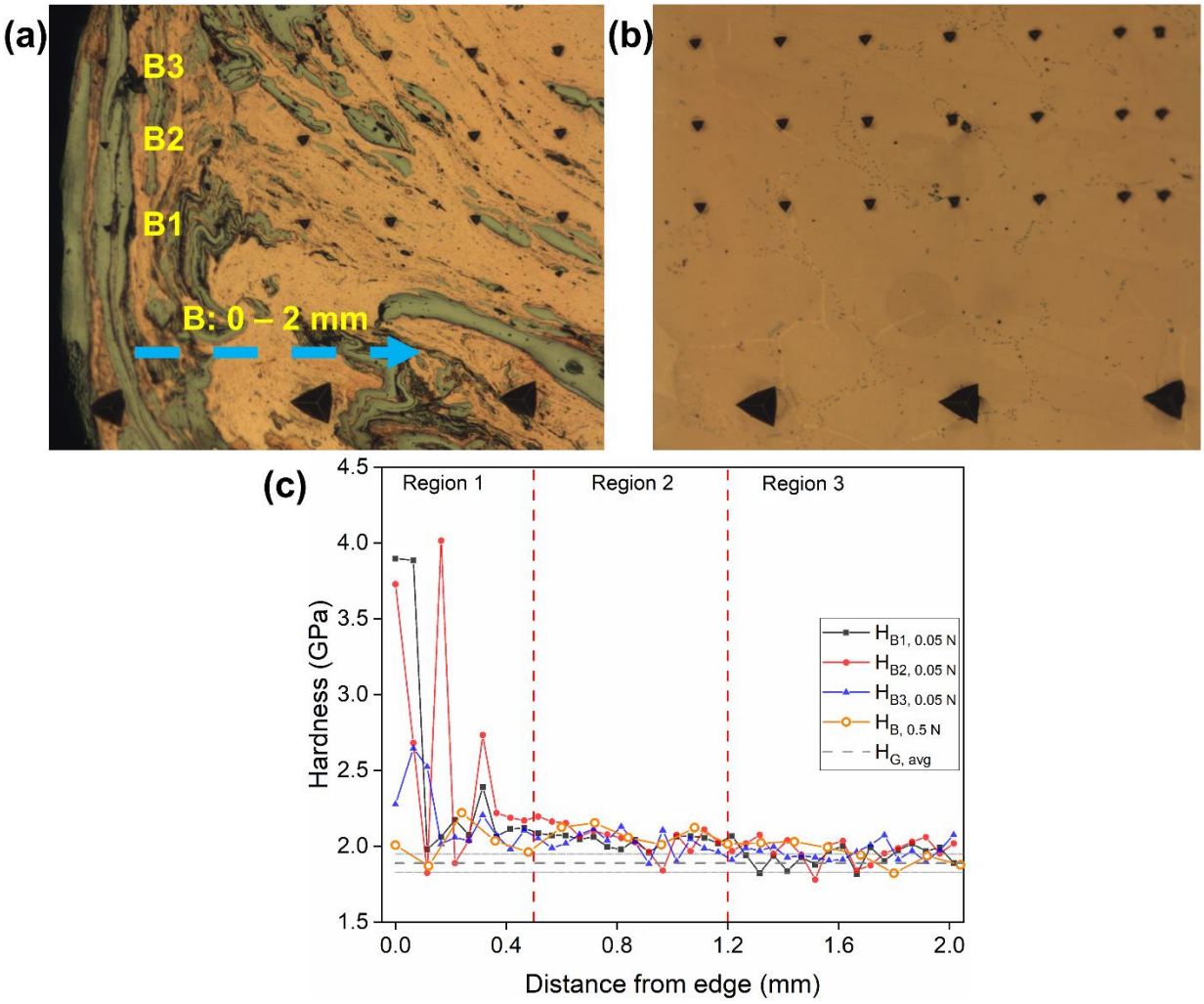

***Figure 60**: (a), (b) Optical images of 40×3 smaller indents along B1, B2 and B3 at 0.05 N and larger indents along B at 0.5 N. (c) Hardness of 40×3 smaller indents as a function of distance from peak edge.*

At peak loads of 0.05 N, indent depth is ~ 0.7 – 1.0 μm and the side length of triangular indents is ~ 5 – 7 μm. Optimizing nanoindentation for localized and denser sampling results in a

clearer demarcation of the steel pick-up region (up to D = ~ 0.5 – 0.6 mm). Previous optical and table-top SEM images have revealed a mixing of steel up to ~ 1 mm below the wheel surface. Interestingly, H values suggest presence of 3 regions: (a) D = 0 to D = 0.5 – 0.6 mm – steel pick-up region, (b) D = 0.5 – 0.6 to D = 1.2 mm – steel mixed with fragmented/deformed Cu and (c) D =1.2 to D = 2.0 mm – Cu polycrystalline region.

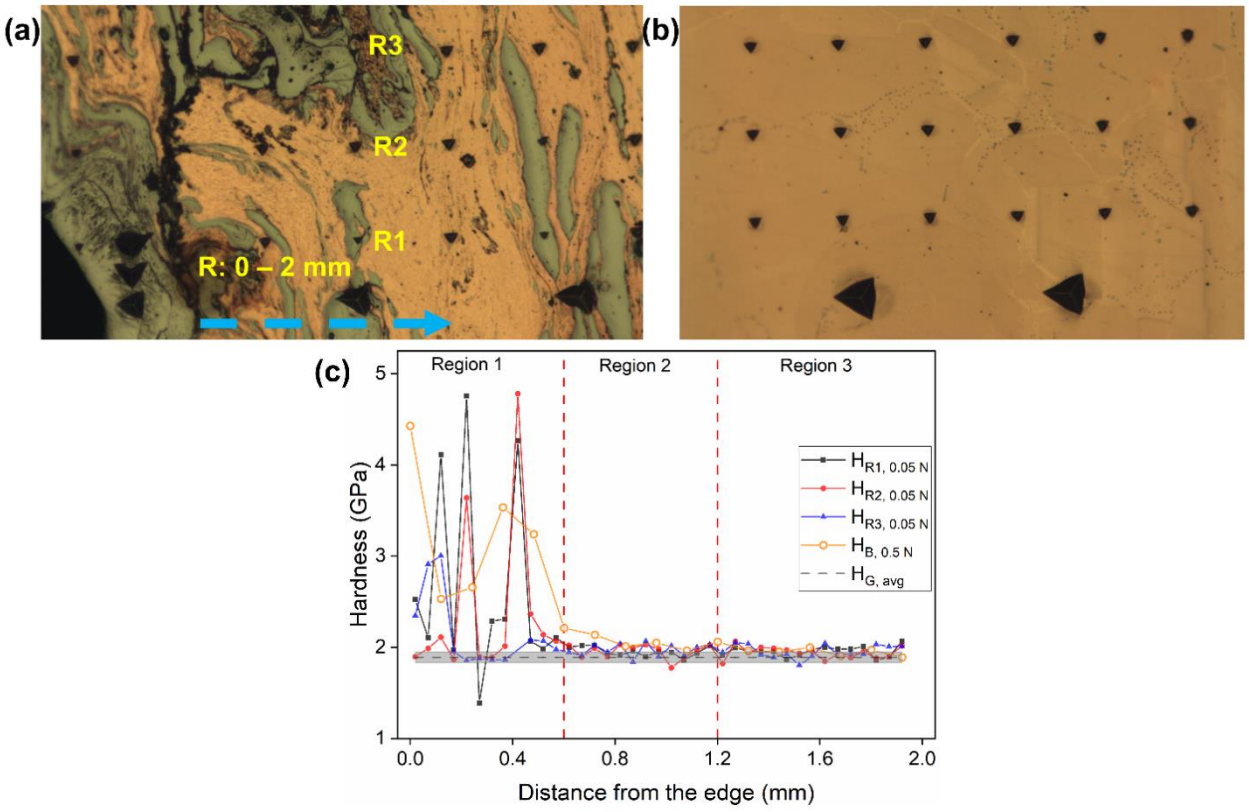

***Figure 61**: (a), (b) Optical images of 40×3 smaller indents along R1, R2 and R3 at 0.05 N and larger indents along R at 0.5 N. (c) Hardness of 40×3 smaller indents as a function of distance from peak edge.*

6.4 Discussion

Taken together, the OM, TSEM, SEM-EDS and hardness mapping results identified two distinct regions: one was Cu-rich and the other was steel-rich. These results point towards a simple

mechanical mixing of the steel and class 2 copper. The water-cooled weld wheels are likely not heating up enough to create additional phases from the Fe-Cu phase diagram that might otherwise have been promoted by significant bulk diffusion. We suggest intermittent air gaps occur between the electrode and work pieces as shown in inset of Figure 51(a), although other factors such as surface contamination, polarity of weld wheels and high weld currents are known to be contributing factors [150,155,160]. This allows the surface of the steel weld joint to melt because the water-cooled copper wheel is not in intimate contact with the steel surface. As the wheel rotates, a molten pool of steel can contact the weld wheel surface and stick to the surface; transferred steel. When the wheel with the transferred steel passes the knurl drive, the knurl pushes the steel into the copper wheel. The combination of steel inclusions and plastic deformation in the electrode is decreasing the overall electrode conductivity and contributing to its failure to produce a quality weld.

We recommend the short-term remedy is to redress the weld wheel surface by removing 0.025 to 0.076 mm of material from the surface of the weld wheel. This redressing is needed up to a point where the weld wheel surface is 100% class 2 material. Contrary to our suggested remedy, limited studies have identified consistent operation of resistance spot welding setups requires maintaining same electrode dimensions together with a constant electrical resistance between the electrodes. Generally speaking, the main dilemma for electrode dressing is between completely removing the picked-up layer at electrode face or taking off just enough surface material to return the electrodes to their original dimensions (also called burnishing), since this choice will strongly influence the electrode diameter and electrode/sheet resistance. This choice will eventually dictate the overall longevity of electrodes as defined by an “electrode campaign life”, or the number of

times a wheel can be redressed before it becomes unusable. Previously, electrode surface burnishing could maintain consistent resistance path without removing all pick-up in narrow wheel seam welding of zinc coated steels [150]. Holliday et al. [163] also concluded that returning electrodes to their original tip diameter without removing all pick-up material resulted in overall lower rate of growth and consistent electrode/sheet resistance during welding of hot-dip zinc coated steel. On the other hand, completely removing pick-up layer could not seam weld for any length of time [150]. The long-term remedy to maximize electrode campaign life is design changes in electrode characteristics such as knurled faces to eliminate air gaps.

6.5 Summary

We studied an exhausted upper Cu electrode wheel in an industrial mash seam welding setup. Combination of metallography and composition analyses revealed a steel mixing region near the electrode surface. Nanoindentation revealed deviation in local material hardness higher than that of base metal due to the mixing and the affected region was identified up to a depth of ~ 1 mm from the surface. The most likely degradation mechanism is an air gap between the upper weld wheel and steel workpieces, causing surface melting of the steel which then gets picked up by the copper electrode and worked in as it rolls. We recommend the short-term remedy is to redress the upper weld wheel surface up to a point where the weld wheel surface is 100% class 2 material. The long-term remedy is design changes in electrode characteristics such as knurled faces to eliminate air gaps.

Chapter 7 Summary and Future Outlook

7.1 Summary

In this thesis, we invoked the principles of materials paradigm to (1) manipulate metallic glass' thermal stability by vapor deposition route and identify the structural origin for these changes, (2) create a data library of processing-structure-property relationships in vapor deposited amorphous carbon thin films for industrial applications, and (3) investigate failure mechanism of copper weld wheels in an industrial manufacturing set-up which did not function as intended.

In chapter 4, we focused on a magnetron sputtering approach to manipulate metallic glass stability and discovered the effects of deposition parameters on thin film amorphicity. Our work advances the glass community's understanding of process/growth parameters, notably the deposition rate to manipulate glass stability and ascribes a structural origin to those stability changes. Our work primarily relied on deposition rate to tune monolayer residence time and substrate temperature to promote surface diffusion.

In chapter 5, we have mapped out the effect of the three major process parameters (voltage, pulse width, and frequency) on film mechanical properties and structure. From Raman spectroscopy, we have correlated high hardness to a few combinations of fractions of sp^3 bonding, sp^2 bonding, and overall film disorder. We built upon our knowledge of structure - mechanical property correlations to design multilayered thin films and establish the mechanical property limits of such multilayers. Multilayers grown at optimal deposition conditions showed improved friction behavior while preserving high hardness.

In chapter 6, we identified the process step causing comparatively shorter lifetime in class 2 copper alloy upper weld wheel. Metallography, imaging and composition analyses revealed steel pick-up from work pieces to weld electrode surface. Metallography and hardness mapping identified steel-mixing region up to a depth of ~ 1 mm. Degradation mechanism is most likely due to an air gap between electrode and weld pieces.

7.2 Future outlook for metallic glass thin films

We expect highly stable metallic glasses to find uses in biomedical, magnetic, optical, mechanical and electronic device applications [164,165]. Our work points to a correlation between improved glass stability and denser glass structure, which we think is an important new paradigm. Denser metallic glasses may have enhanced structural organization that is more typical of crystalline materials, while retaining the advantages of glassy structure such as high strength and improved corrosion resistance due to a lack of grain boundaries.

Surface diffusion-mediated glass relaxation is an enduring argument that can explain ultrastability in molecular glasses [35,166]. Recently, experiments and simulations [49,167–170] revealed fast surface dynamics coinciding with a lower surface glass transition temperature than that of the bulk in Pt-based and Zr-based metallic glasses. Like molecular [35], polymer [40] and chalcogenide glasses [41], promoting surface diffusion is thought to hold the key to attaining highly stable metallic glasses. Tuning surface diffusion with vapor deposition control is very tricky, given the number of process parameters at play and a wide variety of available deposition techniques.

The growth mechanisms of multielement, amorphous, complex metal films by PVD are unclear [164], unlike those of crystalline metal films which are known to grow by island nucleation

and layer growth [171]. Understanding the operating mechanisms may reveal the origin of ultrastable metallic glasses [38,39,44] and "nanoglasses" [172,173], which show very different kinetic states and film structure compared to traditional liquid quenched glasses. In principle, thin films grow by flight and addition of plasma-generated species to the growing film surface together with non-equilibrium plasma impact [174,175]. Several experimental and computational studies have isolated key mechanisms of film growth modes like thermally activated surface diffusion [47], interactions at different length scales [176], film surface and plasma interplay [177], etc. A few studies on amorphous metallic films have reported growth processes different than island nucleation and growth seen in crystalline films: while Cao et. al. discovered a continuous growth mode [51], Xie et. al. [178] and Zhang et. al. [179] proposed film structure evolved by mid-flight aggregation and deposition of the resulting nano-sized clusters rather than surface hops of individual atoms. Practically, relations between deposition conditions and film structure correlate with empirical observations rather than a precise control over fundamental growth processes. Hence, tailoring thin film structure will require coupling study of experimental control to insights into the underlying growth mechanisms.

Our work can be extended to explore alternative deposition technologies with a goal to tune the interplay of numerous process parameters. Since the first reports on ultrastable metallic glasses by magnetron sputtering [39,43], researchers have successfully explored different plasma energy and substrate temperature regimes using other thin film deposition techniques such as ion beam assisted deposition [38,42] and pulsed laser deposition [51]. Identifying optimal deposition techniques that are scalable for manufacturing will require optimizing the monolayer addition rate, plasma duty cycle and incident ion energies and angles at the substrate. Once monolayers are added

and allowed sufficient time, surface diffusivities will need to be tuned. While substrate temperature is the most popular way, other approaches like ion irradiation of growing film surfaces and substrate biasing to increase energy of condensation seem like plausible alternatives. Recently, Bishop et al. [180] explored the concept of deposition rate/substrate temperature superposition principle in molecular glasses, allowing the two-parameter space of deposition rate and substrate temperature to be collapsed into a single variable of an effective deposition rate. Although it has been shown for only a few model non-metallic systems so far, the ability to attain the same glass state by optimizing two parameters instead of one can potentially provide exceptional flexibility for manufacturing considerations and deserves special attention for metallic glasses.

Establishing stability/property limits of highly stable metallic glasses will be crucial to adopt these materials for applications. Going forward, understanding the formation kinetics and thermodynamics of metallic glasses via the vapor deposition route will prove pivotal if their widespread applications are to be reliably realized. An additional consideration with metallic glasses is their propensity to crystallize during processing unlike molecular glasses. Recently, molecular dynamics simulations showed the concentration of icosahedral-like ordering is promoted in a Cu-Zr glass' surface layer and protects the surface against crystallization [181]. Crystallization of bulk alloy melts is very complex and is thermodynamically driven. Numerous models exist for bulk alloy crystallization, but more experiments and simulations will provide additional insight into thin film growth mechanisms of metallic glass films.

Metallic glasses' stability and their response to stimuli, whether by heating or mechanical deformation has been intimately linked to the kind and distribution of medium-range order motifs making up glass structure. Studying glass structure is non-trivial and requires

sophisticated experimental and simulation tools. Our group and others in the glass community have made impressive recent progress in developing such tools including fluctuation electron microscopy, hybrid reverse Monte Carlo simulations [105,106] and angular correlations [118]. As these methods are further developed, we can expect more clarity on the most important glass structure characteristics. To conclude, pathways to connect these glass structure characteristics to vapor deposited glasses' processing, composition, thermodynamics and kinetics, and small volume mechanical deformation promises to advance glass stability improvements otherwise unachievable by conventional liquid-quenching approaches.

References

[1] *Ceramic Glass Cook Top*, https://en.wikipedia.org/wiki/File:Ceranfeld.jpg.

[2] *Glass Building*, https://en.wikipedia.org/wiki/File:The_Shard_from_the_Sky_Garden_2015.jpg.

[3] *Bulk Metallic Glass*, https://en.wikipedia.org/wiki/File:Bulk_Metallic_Glass_Sample.jpg.

[4] *Rewritable Compact Disc*, https://en.wikipedia.org/wiki/File:CD-RW_bottom.jpg.

[5] *Measuring Cup*, https://upload.wikimedia.org/wikipedia/commons/c/ce/Measuring_cup.jpg.

[6] *Glass and Crystal Structures*, https://www.quantamagazine.org/ideal-glass-would-explain-why-glass-exists-at-all-20200311/.

[7] *Edge Dislocation*, https://www.nuclear-power.net/wp-content/uploads/2019/10/edge-dislocation-figure.png.

[8] *Bulk Metallic Glass Gears*, https://www.spaceflightinsider.com/space-centers/jet-propulsion-laboratory/jpl-uses-metallic-glass-make-better-robot-gears/.

[9] *Biomedical and Optical Thin Films*, https://www.ncdtechnologies.com/industrial.

[10] *Cutting Tool Thin Films*, https://www.ctemag.com/news/articles/need-ta-c.

[11] *Sputtering Schematic*, https://en.wikipedia.org/wiki/Sputter_deposition#/media/File:Sputtering2.gif.

[12] *Plasma Schematic*, https://www.britannica.com/science/phase-state-of-matter.

[13] *Plasma Sun*, https://phys.org/news/2019-09-plasma-sun-surface-sunspots-solar.html.

[14] G. Parisi and F. Sciortino, *Structural Glasses: Flying to the Bottom*, Nat. Mater. **12**, 94 (2013).

[15] L. Berthier and M. D. Ediger, *Facets of Glass Physics*, Phys. Today **69**, 40 (2016).

[16] *Starfish*, https://www.thesprucepets.com/starfishes-reef-tank-janitors-2920586.

[17] *Okra Slices*, https://depositphotos.com/122092992/stock-photo-fresh-young-okra-slices.html.

[18] *Rotational Symmetry*, https://www.varsitytutors.com/hotmath/hotmath_help/topics/rotational-symmetry.

[19] *Rotational Symmetries*, https://medium.com/@TheConstructionZone/forbidden-geometry-penrose-tiling-in-hybycozo-8a9c6f427780%0A.

[20] *Silver Lining*, https://theconversation.com/silver-lining-could-covid-19-lead-to-a-better-future-134204.

[21] S. A. Speakman, *Introduction to High Resolution X-Ray Diffraction of Epitaxial Thin Film*, http://prism.mit.edu/xray/oldsite/Introduction to HRXRD.pdf.

[22] *Titan Picture*, https://wcnt.wisc.edu/microscopy/transmission-electron-microscopy/fei-titan-aberration-corrected-stem/.

[23] *TEM Schematic*, https://www.dummies.com/education/science/nanotechnology/see-at-the-nano-level-with-electron-microscopy/.

[24] J. P. Chu, C. Yu, Y. Tanatsugu, M. Yasuzawa, and Y. Shen, *Non-Stick Syringe Needles: Beneficial Effects of Thin Film Metallic Glass Coating*, Sci. Rep. **6**, 31847 (2016).

[25] *Materials Paradigm Tetrahedron*, https://en.wikipedia.org/wiki/File:Materials_science_tetrahedron;structure,_processing,_performance,_and_proprerties.svg#/media/File:Materials_science_tetrahedron;structure,_processing,_performance,_and_proprerties.svg.

[26] O. Milton, *Materials Science of Thin Films* (Elsevier, 2002).

[27] L. K. Alexander Fridman, *Plasma Physics and Engineering*, 2nd ed. (Taylor & Francis, 2011).

[28] A. Anders, *Cathodic Arcs*, Vol. 50 (Springer New York, New York, NY, 2008).

[29] L. L. Alt, S. W. Ing, and K. W. Laendle, *Low-Temperature Deposition of Silicon Oxide Films*, J. Electrochem. Soc. **110**, 465 (1963).

[30] M. Chen, *A Brief Overview of Bulk Metallic Glasses*, NPG Asia Mater. **3**, 82 (2011).

[31] W. Klement, R. H. Willens, and P. Duwez, *Non-Crystalline Structure in Solidified Gold–Silicon Alloys*, Nature **187**, 869 (1960).

[32] J. C. Mauro, *Grand Challenges in Glass Science*, Front. Mater. **1**, 1 (2014).

[33] G. Parisi and F. Sciortino, *Structural Glasses: Flying to the Bottom*, Nat. Mater. **12**, 94 (2013).

[34] P. G. Debenedetti and F. H. Stillinger, *Supercooled Liquids and the Glass Transition*, Nature **410**, 259 (2001).

[35] S. F. Swallen, K. L. Kearns, M. K. Mapes, Y. S. Kim, R. J. McMahon, M. D. Ediger, T. Wu, L. Yu, and S. Satija, *Organic Glasses with Exceptional Thermodynamic and Kinetic Stability*, Science (80-.). **315**, 353 (2007).

[36] K. R. Whitaker, M. Tylinski, M. Ahrenberg, C. Schick, and M. D. Ediger, *Kinetic Stability and Heat Capacity of Vapor-Deposited Glasses of o -Terphenyl*, J. Chem. Phys. **143**, (2015).

[37] K. R. Whitaker, D. J. Scifo, M. D. Ediger, M. Ahrenberg, and C. Schick, *Highly Stable Glasses of Cis-Decalin and Cis/Trans-Decalin Mixtures.*, J. Phys. Chem. B **117**, 12724 (2013).

[38] P. Luo, C. R. Cao, F. Zhu, Y. M. Lv, Y. H. Liu, P. Wen, H. Y. Bai, G. Vaughan, M. di Michiel, B. Ruta, and W. H. Wang, *Ultrastable Metallic Glasses Formed on Cold Substrates*, Nat. Commun. **9**, 1389 (2018).

[39] H. B. Yu, Y. Luo, and K. Samwer, *Ultrastable Metallic Glass*, Adv. Mater. **25**, 5904 (2013).

[40] Y. Guo, A. Morozov, D. Schneider, J. W. Chung, C. Zhang, M. Waldmann, N. Yao, G. Fytas, C. B. Arnold, and R. D. Priestley, *Ultrastable Nanostructured Polymer Glasses*, Nat. Mater. **11**, 337 (2012).

[41] K. Zhang, Y. Li, Q. Huang, B. Wang, X. Zheng, Y. Ren, and W. Yang, *Ultrastable Amorphous Sb 2 Se 3 Film*, J. Phys. Chem. B **121**, 8188 (2017).

[42] M. Liu, C. R. Cao, Y. M. Lu, W. H. Wang, and H. Y. Bai, *Flexible Amorphous Metal Films with High Stability*, Appl. Phys. Lett. **110**, 031901 (2017).

[43] D. P. B. Aji, A. Hirata, F. Zhu, L. Pan, K. M. Reddy, S. Song, Y. Liu, T. Fujita, S. Kohara,

and M. Chen, *Ultrastrong and Ultrastable Metallic Glass*, ArXiv Prepr. 1 (2013).

[44] D. J. Magagnosc, G. Feng, L. Yu, X. Cheng, and D. S. Gianola, *Isochemical Control over Structural State and Mechanical Properties in Pd-Based Metallic Glass by Sputter Deposition at Elevated Temperatures*, APL Mater. **4**, 086104 (2016).

[45] S. Y. Liu, Q. P. Cao, X. Qian, C. Wang, X. D. Wang, D. X. Zhang, X. L. Hu, W. Xu, M. Ferry, and J. Z. Jiang, *Effects of Substrate Temperature on Structure, Thermal Stability and Mechanical Property of a Zr-Based Metallic Glass Thin Film*, Thin Solid Films **595**, 17 (2015).

[46] J. H. Chu, H. W. Chen, Y. C. Chan, J. G. Duh, J. W. Lee, and J. S. C. Jang, *Modification of Structure and Property in Zr-Based Thin Film Metallic Glass via Processing Temperature Control*, Thin Solid Films **561**, 38 (2014).

[47] Y. G. Yang, R. A. Johnson, and H. N. G. Wadley, *A Monte Carlo Simulation of the Physical Vapor Deposition of Nickel*, Acta Mater. **45**, 1455 (1997).

[48] S. Capaccioli, K. L. Ngai, M. Paluch, and D. Prevosto, *Mechanism of Fast Surface Self-Diffusion of an Organic Glass*, **051503**, 1 (2012).

[49] C. R. Cao, Y. M. Lu, H. Y. Bai, and W. H. Wang, *High Surface Mobility and Fast Surface Enhanced Crystallization of Metallic Glass*, Appl. Phys. Lett. **107**, (2015).

[50] J. Tersoff, A. W. Denier van der Gon, and R. M. Tromp, *Critical Island Size for Layer-by-Layer Growth*, Phys. Rev. Lett. **72**, 266 (1994).

[51] C. R. Cao, K. Q. Huang, N. J. Zhao, Y. T. Sun, H. Y. Bai, L. Gu, D. N. Zheng, and W. H.

Wang, *Ultrahigh Stability of Atomically Thin Metallic Glasses*, Appl. Phys. Lett. **105**, 011909 (2014).

[52] M. Gopinadhan, Z. Shao, Y. Liu, S. Mukherjee, R. C. Sekol, G. Kumar, A. D. Taylor, J. Schroers, and C. O. Osuji, *Finite Size Effects in the Crystallization of a Bulk Metallic Glass*, Appl. Phys. Lett. **103**, 111912 (2013).

[53] G. B. Bokas, L. Zhao, D. Morgan, and I. Szlufarska, *Increased Stability of CuZrAl Metallic Glasses Prepared by Physical Vapor Deposition*, J. Alloys Compd. **728**, 1110 (2017).

[54] H. W. Sheng, W. K. Luo, F. M. Alamgir, J. M. Bai, and E. Ma, *Atomic Packing and Short-to-Medium-Range Order in Metallic Glasses*, Nature **439**, 419 (2006).

[55] Y. Q. Cheng, H. W. Sheng, and E. Ma, *Relationship between Structure, Dynamics, and Mechanical Properties in Metallic Glass-Forming Alloys*, Phys. Rev. B **78**, 014207 (2008).

[56] Y. Q. Cheng and E. Ma, *Atomic-Level Structure and Structure–Property Relationship in Metallic Glasses*, Prog. Mater. Sci. **56**, 379 (2011).

[57] Y. Q. Cheng, E. Ma, and H. W. Sheng, *Atomic Level Structure in Multicomponent Bulk Metallic Glass*, Phys. Rev. Lett. **102**, 245501 (2009).

[58] Y. Q. Cheng, E. Ma, and H. W. Sheng, *Alloying Strongly Influences the Structure, Dynamics, and Glass Forming Ability of Metallic Supercooled Liquids*, Appl. Phys. Lett. **93**, 10 (2008).

[59] F. H. . Zetterling, M. Dzugutov, and S. . Simdyankin, *Formation of Large-Scale Icosahedral Clusters in a Simple Liquid Approaching the Glass Transition*, J. Non. Cryst. Solids **293**–

295, 39 (2001).

[60] M. Dzugutov, S. I. Simdyankin, and F. H. M. Zetterling, *Decoupling of Diffusion from Structural Relaxation and Spatial Heterogeneity in a Supercooled Simple Liquid*, Phys. Rev. Lett. **89**, 195701 (2002).

[61] J. Gibson and M. Treacy, *Diminished Medium-Range Order Observed in Annealed Amorphous Germanium*, Phys. Rev. Lett. **78**, 1074 (1997).

[62] H. Bin Yu, Y. Luo, and K. Samwer, *Ultrastable Metallic Glass*, Adv. Mater. **25**, 5904 (2013).

[63] J. Robertson, *Diamond-like Amorphous Carbon*, Mater. Sci. Eng. R Reports **37**, 129 (2002).

[64] J. Robertson, *Properties of Diamond-like Carbon*, Surf. Coatings Technol. **50**, 185 (1992).

[65] J. C. Angus and C. C. Hayman, *Low-Pressure , Metastable Growth of Diamond and "Diamondlike" Phases*, Science (80-.). **241**, 913 (1988).

[66] A. A. Voevodin and M. S. Donley, *Preparation of Amorphous Diamond-like Carbon by Pulsed Laser Deposition: A Critical Review*, Surf. Coatings Technol. **82**, 199 (1996).

[67] A. Grill, *Diamond-like Carbon Coatings as Biocompatible Materials - An Overview*, Diam. Relat. Mater. **12**, 166 (2003).

[68] P. J. Heaney, A. V. Sumant, C. D. Torres, R. W. Carpick, and F. E. Pfefferkorn, *Diamond Coatings for Micro End Mills: Enabling the Dry Machining of Aluminum at the Micro-Scale*, Diam. Relat. Mater. **17**, 223 (2008).

[69] P. R. Goglia, J. Berkowitz, J. Hoehn, A. Xidis, and L. Stover, *Diamond-like Carbon*

Applications in High Density Hard Disc Recording Heads, Diam. Relat. Mater. **10**, 271 (2001).

[70] N. Savvides, *Optical Constants and Associated Functions of Metastable Diamondlike Amorphous Carbon Films in the Energy Range 0.5-7.3 EV*, J. Appl. Phys. **59**, 4133 (1986).

[71] E. G. Spencer, P. H. Schmidt, D. C. Joy, and F. J. Sansalone, *Ion-Beam-Deposited Polycrystalline Diamondlike Films*, Appl. Phys. Lett. **29**, 118 (1976).

[72] A. Anders, N. Pasaja, S. H. N. Lim, T. C. Petersen, and V. J. Keast, *Plasma Biasing to Control the Growth Conditions of Diamond-like Carbon*, Surf. Coatings Technol. **201**, 4628 (2007).

[73] A. Pauschitz, J. Schalko, and T. Koch, *Nanoindentation and AFM Studies of PECVD DLC and Reactively Sputtered Ti Containing Carbon Films*, Bull. Mater. Sci. **26**, 585 (2003).

[74] Q. Wei, A. K. Sharma, J. Sankar, and J. Narayan, *Mechanical Properties of Diamond-like Carbon Composite Thin Films Prepared by Pulsed Laser Deposition*, Compos. Part B **30**, 675 (1999).

[75] A. Gangopadhyay, *Mechanical and Tribological Properties of Amorphous Carbon Films*, Tribol. Lett. **5**, 25 (1998).

[76] Weiler, *Amorphous Hydrogenated Carbon Prepared from a Plasma Beam Source*, Appl. Phys. Lett. **2797**, (1998).

[77] E. H. T. Teo, D. H. C. Chua, and B. K. Tay, *Mechanical Properties of Alternating High-Low Sp3 Content Thick Non-Hydrogenated Diamond-like Amorphous Carbon Films*, Diam.

Relat. Mater. **16**, 1882 (2007).

[78] D. Sheeja, B. K. Tay, S. P. Lau, and X. Shi, *Tribological Properties and Adhesive Strength of DLC Coatings Prepared under Different Substrate Bias Voltages*, Wear **249**, 433 (2001).

[79] P. Zhang, B. K. Tay, C. Q. Sun, and S. P. Lau, *Microstructure and Mechanical Properties of Nanocomposite Amorphous Carbon Films*, J. Vac. Sci. Technol. A Vacuum, Surfaces, Film. **20**, 1390 (2002).

[80] S. Anders, D. L. Callahan, G. M. Pharr, T. Y. Tsui, and C. S. Bhatia, *Multilayers of Amorphous Carbon Prepared by Cathodic Arc Deposition*, Surf. Coatings Technol. **94**–**95**, 189 (1997).

[81] S. Logothetidis, S. Kassavetis, C. Charitidis, Y. Panayiotatos, and A. Laskarakis, *Nanoindentation Studies of Multilayer Amorphous Carbon Films*, Carbon N. Y. **42**, 1133 (2004).

[82] N. Xu, H. T. E. Teo, M. Shakerzadeh, X. Wang, C. M. Ng, and B. K. Tay, *Electrical Properties of Textured Carbon Film Formed by Pulsed Laser Annealing*, Diam. Relat. Mater. **23**, 135 (2012).

[83] C. W. Tan, S. Maziar, E. H. T. Teo, and B. K. Tay, *Microstructure and Through-Film Electrical Characteristics of Vertically Aligned Amorphous Carbon Films*, Diam. Relat. Mater. **20**, 290 (2011).

[84] H. Li, T. Xu, C. Wang, J. Chen, H. Zhou, and H. Liu, *Annealing Effect on the Structure, Mechanical and Tribological Properties of Hydrogenated Diamond-like Carbon Films*,

Thin Solid Films **515**, 2153 (2006).

[85] D. W. M. Lau, D. G. McCulloch, N. A. Marks, N. R. Madsen, and A. V. Rode, *High-Temperature Formation of Concentric Fullerene-like Structures within Foam-like Carbon: Experiment and Molecular Dynamics Simulation*, Phys. Rev. B - Condens. Matter Mater. Phys. **75**, 3 (2007).

[86] L. Ji, H. Li, F. Zhao, W. Quan, J. Chen, and H. Zhou, *Effects of Pulse Bias Duty Cycle on Fullerenelike Nanostructure and Mechanical Properties of Hydrogenated Carbon Films Prepared by Plasma Enhanced Chemical Vapor Deposition Method*, J. Appl. Phys. **105**, 106113 (2009).

[87] M. I. Mejía, G. Restrepo, J. M. Marín, R. Sanjines, C. Pulgarín, E. Mielczarski, J. Mielczarski, and J. Kiwi, *Magnetron-Sputtered Ag Surfaces. New Evidence for the Nature of the Ag Ions Intervening in Bacterial Inactivation*, ACS Appl. Mater. Interfaces **2**, 230 (2010).

[88] H. Yasuda, *General Characteristics of Plasma Polymers*, in *Plasma Polymerization* (Elsevier, 1985), pp. 334–369.

[89] W. Ensinger, *Correlations between Process Parameters and Film Properties of Diamond-like Carbon Films Formed by Hydrocarbon Plasma Immersion Ion Implantation*, Surf. Coatings Technol. **203**, 2721 (2009).

[90] B. D. Cullity, *Elements of X Ray Diffraction - Scholar's Choice Edition* (Scholar's Choice, 2015).

[91] H. Xiang, Engineering and Characterizing Inverse Tunneling Magnetoresistance Magnetic Tunnel Junctions with Novel Ferromagnetic Electrodes, University of Wisconsin-Madison, 2011.

[92] J. I. Goldstein, D. E. Newbury, P. Echlin, D. C. Joy, C. E. Lyman, E. Lifshin, L. Sawyer, and J. R. Michael, *Scanning Electron Microscopy and X-Ray Microanalysis*, 3rd ed. (Springer US, Boston, MA, 2003).

[93] T. E. Everhart and R. F. M. Thornley, *Wide-Band Detector for Micro-Microampere Low-Energy Electron Currents*, J. Sci. Instrum. **37**, 246 (1960).

[94] W. Jansen and M. Slaughter, *Elemental Mapping of Minerals by Electron Microprobe*, Am. Mineral. **67**, 521 (1982).

[95] A. Moy and J. Fournelle, *BadgerFilm: An Open Source Thin Film Analysis Program*, Microsc. Microanal. **26**, 496 (2020).

[96] B. Cappella and G. Dietler, *Force-Distance Curves by Atomic Force Microscopy*, Surf. Sci. Rep. **34**, 1 (1999).

[97] P. J. Bryant, R. G. Miller, and R. Yang, *Scanning Tunneling and Atomic Force Microscopy Combined*, Appl. Phys. Lett. **52**, 2233 (1988).

[98] Y. Gao, B. Zhao, J. J. Vlassak, and C. Schick, *Nanocalorimetry: Door Opened for in Situ Material Characterization under Extreme Non-Equilibrium Conditions*, Prog. Mater. Sci. **104**, 53 (2019).

[99] C. Oliver and M. Pharr, *An Improved Technique for Determining Hardness and Elastic*

Modulus Using Load and Displacement Sensing Indentation Experiments, Journal of Materials Research.

[100] M. Sakai, *Meyer Hardness: A Measure for Plasticity?*, J. Mater. Res. **14**, 3630 (1999).

[101] Y. Li, S. Feng, W. Wu, and F. Li, *Temperature Dependent Mechanical Property of PZT Film: An Investigation by Nanoindentation*, PLoS One **10**, 1 (2015).

[102] M. Ghidelli, S. Gravier, J. J. Blandin, P. Djemia, F. Mompiou, G. Abadias, J. P. Raskin, and T. Pardoen, *Extrinsic Mechanical Size Effects in Thin ZrNi Metallic Glass Films*, Acta Mater. **90**, 232 (2015).

[103] R. Vaidyanathan, M. Dao, G. Ravichandran, and S. Suresh, *Study of Mechanical Deformation in Bulk Metallic Glass through Instrumented Indentation*, Acta Mater. **49**, 3781 (2001).

[104] A. Bolshakov and G. M. Pharr, *Influences of Pileup on the Measurement of Mechanical Properties by Load and Depth Sensing Indentation Techniques*, J. Mater. Res. **13**, 1049 (1998).

[105] J. Hwang, Z. Melgarejo, Y. E. Kalay, I. Kalay, M. J. Kramer, D. S. Stone, and P. M. Voyles, *Nanoscale Structure and Structural Relaxation in Zr_{50}Cu_{45}Al_{5} Bulk Metallic Glass*, Phys. Rev. Lett. **108**, 195505 (2012).

[106] P. Zhang, J. J. Maldonis, M. F. Besser, M. J. Kramer, and P. M. Voyles, *Medium-Range Structure and Glass Forming Ability in Zr–Cu–Al Bulk Metallic Glasses*, Acta Mater. **109**, 103 (2016).

[107] P. M. Voyles, J. M. Gibson, and M. M. J. Treacy, *Fluctuation Microscopy: A Probe of Atomic Correlations in Disordered Materials*, J. Electron Microsc. (Tokyo). **49**, 259 (2000).

[108] M. M. J. Treacy, J. M. Gibson, L. Fan, D. J. Paterson, and I. McNulty, *Fluctuation Microscopy: A Probe of Medium Range Order*, Reports Prog. Phys. **68**, 2899 (2005).

[109] A. C. Y. Liu, M. J. Neish, G. Stokol, G. A. Buckley, L. A. Smillie, M. D. De Jonge, R. T. Ott, M. J. Kramer, and L. Bourgeois, *Systematic Mapping of Icosahedral Short-Range Order in a Melt-Spun Zr 36Cu64 Metallic Glass*, Phys. Rev. Lett. **110**, 1 (2013).

[110] J. Hwang, *Doctoral Thesis*, Univeristy of Wisconsin-Madison (2011).

[111] X. Jiang, K. Reichelt, and B. Stritzker, *Mechanical Properties of a -C:H Films Prepared by Plasma Decomposition of C 2 H 2*, J. Appl. Phys. **68**, 1018 (1990).

[112] G. M. Pharr, *Measurement of Mechanical Properties by Ultra-Low Load Indentation*, Mater. Sci. Eng. A **253**, 151 (1998).

[113] D. Nečas, *Basic Data Processing*, in *Quantitative Data Processing in Scanning Probe Microscopy*, edited by P. B. T.-Q. D. P. in S. P. M. (Second E. Klapetek (Elsevier, 2018), pp. 65–96.

[114] D. Ma, A. D. Stoica, and X.-L. Wang, *Power-Law Scaling and Fractal Nature of Medium-Range Order in Metallic Glasses.*, Nat. Mater. **8**, 30 (2009).

[115] D. Lee, B. Zhao, E. Perim, H. Zhang, P. Gong, Y. Gao, Y. Liu, C. Toher, S. Curtarolo, J. Schroers, and J. J. Vlassak, *Crystallization Behavior upon Heating and Cooling in Cu50Zr50 Metallic Glass Thin Films*, Acta Mater. **121**, 68 (2016).

[116] K. L. Kearns, M. D. Ediger, H. Huth, and C. Schick, *One Micrometer Length Scale Controls Kinetic Stability of Low-Energy Glasses*, J. Phys. Chem. Lett. **1**, 388 (2010).

[117] J. M. Gibson, M. M. J. Treacy, T. Sun, and N. J. Zaluzec, *Substantial Crystalline Topology in Amorphous Silicon*, Phys. Rev. Lett. **105**, 1 (2010).

[118] S. Im, Z. Chen, J. M. Johnson, P. Zhao, G. H. Yoo, E. S. Park, Y. Wang, D. A. Muller, and J. Hwang, *Direct Determination of Structural Heterogeneity in Metallic Glasses Using Four-Dimensional Scanning Transmission Electron Microscopy*, Ultramicroscopy **195**, 189 (2018).

[119] J. H. Chu, H. W. Chen, Y. C. Chan, J. G. Duh, J. W. Lee, and J. S. C. Jang, *Modification of Structure and Property in Zr-Based Thin Film Metallic Glass via Processing Temperature Control*, Thin Solid Films **561**, 38 (2014).

[120] J. Hwang, Z. H. Melgarejo, Y. E. Kalay, I. Kalay, M. J. Kramer, D. S. Stone, and P. M. Voyles, *Nanoscale Structure and Structural Relaxation in Zr50Cu45Al5 Bulk Metallic Glass*, Phys. Rev. Lett. **108**, 195505 (2012).

[121] K. L. Kearns, T. Still, G. Fytas, and M. D. Ediger, *High-Modulus Organic Glasses Prepared by Physical Vapor Deposition*, Adv. Mater. **22**, 39 (2010).

[122] B. Yang, C. T. Liu, and T. G. Nieh, *Unified Equation for the Strength of Bulk Metallic Glasses*, Appl. Phys. Lett. **88**, 221911 (2006).

[123] P. Zhang, S. X. Li, and Z. F. Zhang, *General Relationship between Strength and Hardness*, Mater. Sci. Eng. A **529**, 62 (2011).

[124] J. Saida, R. Yamada, and M. Wakeda, *Recovery of Less Relaxed State in Zr-Al-Ni-Cu Bulk Metallic Glass Annealed above Glass Transition Temperature*, Appl. Phys. Lett. **103**, 221910 (2013).

[125] O. Haruyama, Y. Nakayama, R. Wada, H. Tokunaga, J. Okada, T. Ishikawa, and Y. Yokoyama, *Volume and Enthalpy Relaxation in Zr55Cu30Ni5Al10 Bulk Metallic Glass*, Acta Mater. **58**, 1829 (2010).

[126] A. Rauf, C. Y. Guo, Y. N. Fang, Z. Yu, B. A. Sun, and T. Feng, *Binary Cu-Zr Thin Film Metallic Glasses with Tunable Nanoscale Structures and Properties*, J. Non. Cryst. Solids **498**, 95 (2018).

[127] S. V. Ketov, R. Joksimovic, G. Xie, A. Trifonov, K. Kurihara, and D. V. Louzguine-Luzgin, *Formation of Nanostructured Metallic Glass Thin Films upon Sputtering*, Heliyon **3**, e00228 (2017).

[128] D. Manova, J. W. Gerlach, and S. Mändl, *Thin Film Deposition Using Energetic Ions*, Materials (Basel). **3**, 4109 (2010).

[129] K. L. Kearns, S. F. Swallen, M. D. Ediger, T. Wu, Y. Sun, and L. Yu, *Hiking down the Energy Landscape: Progress Toward the Kauzmann Temperature via Vapor Deposition*, J. Phys. Chem. B **112**, 4934 (2008).

[130] N. Chen, D. V. Louzguine-Luzgin, G. Q. Xie, P. Sharma, J. H. Perepezko, M. Esashi, A. R. Yavari, and A. Inoue, *Structural Investigation and Mechanical Properties of a Representative of a New Class of Materials: Nanograined Metallic Glasses*, Nanotechnology **24**, 045610 (2013).

[131] G. B. Bokas, L. Zhao, D. Morgan, and I. Szlufarska, *Increased Stability of CuZrAl Metallic Glasses Prepared by Physical Vapor Deposition*, J. Alloys Compd. **728**, 1110 (2017).

[132] F. H. . Zetterling, M. Dzugutov, and S. . Simdyankin, *Formation of Large-Scale Icosahedral Clusters in a Simple Liquid Approaching the Glass Transition*, J. Non. Cryst. Solids **293**–**295**, 39 (2001).

[133] A. L. Greer, Y. Q. Cheng, and E. Ma, *Shear Bands in Metallic Glasses*, Mater. Sci. Eng. R **74**, 71 (2013).

[134] M. M. Trexler and N. N. Thadhani, *Mechanical Properties of Bulk Metallic Glasses*, Prog. Mater. Sci. **55**, 759 (2010).

[135] Z. H. Melgarejo, J. E. Jakes, J. Hwang, Y. E. Kalay, M. J. Kramer, P. M. Voyles, and D. S. Stone, *Variation of Hardness and Modulus across the Thickness of Zr-Cu-Al Metallic Glass Ribbons*, MRS Proc. **1520**, mrsf12 (2012).

[136] Y. Q. Cheng, A. J. Cao, and E. Ma, *Correlation between the Elastic Modulus and the Intrinsic Plastic Behavior of Metallic Glasses: The Roles of Atomic Configuration and Alloy Composition*, Acta Mater. **57**, 3253 (2009).

[137] H. L. Peng, M. Z. Li, and W. H. Wang, *Structural Signature of Plastic Deformation in Metallic Glasses*, Phys. Rev. Lett. **106**, 135503 (2011).

[138] P. Guan, M. Chen, and T. Egami, *Stress-Temperature Scaling for Steady-State Flow in Metallic Glasses*, Phys. Rev. Lett. **104**, 205701 (2010).

[139] A. C. Ferrari and J. Robertson, *Interpretation of Raman Spectra of Disordered and*

Amorphous Carbon, Phys. Rev. B **61**, 14095 (2000).

[140] M. A. Tamor and W. C. Vassell, *Raman "Fingerprinting" of Amorphous Carbon Films*, J. Appl. Phys. **76**, 3823 (1994).

[141] G. Irmer and A. Dorner-Reisel, *Micro-Raman Studies on DLC Coatings*, Adv. Eng. Mater. **7**, 694 (2005).

[142] Y. R. Jeng, P. C. Tsai, K. Te Wu, Y. M. Wang, F. C. N. Hong, S. M. Huang, and K. C. Chen, *Effect of Feed Gas Composition Effects on the Nanotribological Properties of Diamond-like Carbon Films*, Thin Solid Films **529**, 301 (2013).

[143] A. Modabberasl, P. Kameli, M. Ranjbar, H. Salamati, and R. Ashiri, *Fabrication of DLC Thin Films with Improved Diamond-like Carbon Character by the Application of External Magnetic Field*, Carbon N. Y. **94**, 485 (2015).

[144] W. T. Zheng, H. Sjöström, I. Ivanov, K. Z. Xing, E. Broitman, W. R. Salaneck, J. E. Greene, and J. -E. Sundgren, *Reactive Magnetron Sputter Deposited CN X : Effects of N 2 Pressure and Growth Temperature on Film Composition, Bonding, and Microstructure* , J. Vac. Sci. Technol. A Vacuum, Surfaces, Film. **14**, 2696 (1996).

[145] K. L. Johnson, *Contact Mechanics*, (1989).

[146] T. Y. Tsui, G. M. Pharr, W. C. Oliver, C. S. Bhatia, R. L. White, S. Anders, A. Anders, and I. G. Brown, *Nanoindentation and Nanoscratching of Hard Carbon Coatings for Magnetic Disks*, MRS Proc. **383**, 447 (1995).

[147] E. Thomson, *Method of Electric Welding*, 451,345 (1891).

[148] P. Houldcraft, *Welding Process Technology* (Cambridge University Press, Cambridge, England, 1977).

[149] R. W. M. Association, *Resistance Welding Manual*, fourth (1989).

[150] N. T. Williams and J. D. Parker, *Review of Resistance Spot Welding of Steel Sheets Part 2 Factors Influencing Electrode Life*, Int. Mater. Rev. **49**, 77 (2004).

[151] R. S. Florea, K. N. Solanki, D. J. Bammann, J. C. Baird, J. B. Jordon, and M. P. Castanier, *Resistance Spot Welding of 6061-T6 Aluminum: Failure Loads and Deformation*, Mater. Des. **34**, 624 (2012).

[152] K. R. Chan, Weldability and Degradation Study of Coated Electrodes for Resistance Spot Welding, University of Waterloo, 2005.

[153] D. Ing and M. Spitz, Electrode Degradation during Resistance Spot Welding of Conversion Coated Hot Dip Galvanized Steel Sheets, Vienna University of Technology, 2014.

[154] S. Pawar, S. Sahoo, and G. Mukhopadhyay, *Failure Analysis of Weld Joint of High Strength Quality Steel Sheets in Cold Rolling Mill*, Eng. Fail. Anal. **103**, 392 (2019).

[155] J. D. Parker, N. T. Williams, and R. J. Holliday, *Mechanisms of Electrode Degradation When Spot Welding Coated Steels*, Sci. Technol. Weld. Join. **3**, 65 (1998).

[156] A. de, L. Dorn, and O. P. Gupta, *Analysis and Optimisation of Electrode Life for Conventional and Compound Tip Electrodes during Resistance Spot Welding of Electrogalvanised Steels*, Sci. Technol. Weld. Join. **5**, 49 (2000).

[157] E. Gauthier, D. Carron, P. Rogeon, P. Pilvin, C. Pouvreau, T. Lety, and F. Primaux,

Numerical Modeling of Electrode Degradation During Resistance Spot Welding Using CuCrZr Electrodes, J. Mater. Eng. Perform. **23**, 1593 (2014).

[158] L. Han, M. Thornton, D. Li, and M. Shergold, *Effect of Governing Metal Thickness and Stack Orientation on Weld Quality and Mechanical Behaviour of Resistance Spot Welding of AA5754 Aluminium*, Mater. Des. **32**, 2107 (2011).

[159] M. Rashid, *Some Tribological Influences on the Electrode-Worksheet Interface During Resistance Spot Welding of Aluminum Alloys*, J. Mater. Eng. Perform. **20**, 456 (2011).

[160] S. M. Manladan, F. Yusof, S. Ramesh, M. Fadzil, Z. Luo, and S. Ao, *A Review on Resistance Spot Welding of Aluminum Alloys*, Int. J. Adv. Manuf. Technol. **90**, 605 (2017).

[161] B. Lang, D. Q. Sun, G. Z. Li, and B. Q. Zhu, *Electrode Degradation in Resistance Spot Welding of Magnesium Alloy*, ISIJ Int. **49**, 1744 (2009).

[162] T. O. Ziebold, *Precision and Sensitivity in Electron Microprobe Analysis*, Anal. Chem. **39**, 858 (1967).

[163] N. T. W. R. Holliday, J. D. Parker, *Relative Contribution of Electrode Tip Growth Mechanisms in Spot Welding Zinc Coated Steels*, Weld. World **37**, 186 (1996).

[164] J. P. Chu, J. S. C. Jang, J. C. Huang, H. S. Chou, Y. Yang, J. C. Ye, Y. C. Wang, J. W. Lee, F. X. Liu, P. K. Liaw, Y. C. Chen, C. M. Lee, C. L. Li, and C. Rullyani, *Thin Film Metallic Glasses: Unique Properties and Potential Applications*, Thin Solid Films **520**, 5097 (2012).

[165] S. Liu, Q. Cao, D. Zhang, and J. Jiang, *Metallic Glassy Thin Films: Perspective on Mechanical, Magnetic, Biomedical, and Optical Properties*, Adv. Eng. Mater. **21**, 1900046

(2019).

[166] L. Berthier, P. Charbonneau, E. Flenner, and F. Zamponi, *Origin of Ultrastability in Vapor-Deposited Glasses*, Phys. Rev. Lett. **119**, 188002 (2017).

[167] P. Zhang, J. J. Maldonis, Z. Liu, J. Schroers, and P. M. Voyles, *Spatially Heterogeneous Dynamics in a Metallic Glass Forming Liquid Imaged by Electron Correlation Microscopy*, Nat. Commun. **9**, 1129 (2018).

[168] P. M. V. Debaditya Chatterjee, Ajay Annamareddy, Jittisa Ketkaew, Jan Schroers, Dane Morgan, *Fast Surface Dynamics on a Metallic Glass Nanowire*, To Be Submitt. (2020).

[169] D. M. Ajay Annamareddy, Paul M. Voyles, *Factors Controlling the Enhanced Surface Diffusion in Metallic Glasses*, To Be Submitt. (2020).

[170] D. M. Ajay Annamareddy, Paul M. Voyles, John H. Perepezko, *Mechanisms of Bulk and Surface Diffusion in Metallic Glasses Determined from Molecular Dynamics Simulations*, To Be Submitt. (2020).

[171] K. Oura, M. Katayama, A. V Zotov, V. G. Lifshits, and A. A. Saranin, *Growth of Thin Films*, in *Surface Science: An Introduction* (Springer Berlin Heidelberg, Berlin, Heidelberg, 2003), pp. 357–387.

[172] H. Gleiter, *Nanoglasses: A New Kind of Noncrystalline Materials*, Beilstein J. Nanotechnol. **4**, 517 (2013).

[173] H. Gleiter, *Our Thoughts Are Ours, Their Ends None of Our Own: Are There Ways to Synthesize Materials beyond the Limitations of Today?*, Acta Mater. **56**, 5875 (2008).

[174] E. Tam, I. Levchenko, K. Ostrikov, M. Keidar, and S. Xu, *Ion-Assisted Functional Monolayer Coating of Nanorod Arrays in Hydrogen Plasmas*, Phys. Plasmas **14**, 033503 (2007).

[175] R. Alvarez, P. Romero-Gomez, J. Gil-Rostra, J. Cotrino, F. Yubero, A. Palmero, and A. R. Gonzalez-Elipe, *On the Microstructure of Thin Films Grown by an Isotropically Directed Deposition Flux*, J. Appl. Phys. **108**, 064316 (2010).

[176] J. Yu and J. G. Amar, *Effects of Short-Range Attraction in Metal Epitaxial Growth*, Phys. Rev. Lett. **89**, 286103 (2002).

[177] S. Mráz and J. M. Schneider, *Influence of the Negative Oxygen Ions on the Structure Evolution of Transition Metal Oxide Thin Films*, J. Appl. Phys. **100**, 023503 (2006).

[178] L. Xie, P. Brault, A.-L. Thomann, and J.-M. Bauchire, *AlCoCrCuFeNi High Entropy Alloy Cluster Growth and Annealing on Silicon: A Classical Molecular Dynamics Simulation Study*, Appl. Surf. Sci. **285**, 810 (2013).

[179] J. Y. Zhang, Z. Y. Ding, F. C. Li, and Y. Yang, *Controlled Synthesis of Nanostructured Glassy and Crystalline High Entropy Alloy Films*, Nanotechnology **31**, 045601 (2020).

[180] C. Bishop, A. Gujral, M. F. Toney, L. Yu, and M. D. Ediger, *Vapor-Deposited Glass Structure Determined by Deposition Rate–Substrate Temperature Superposition Principle*, J. Phys. Chem. Lett. **10**, 3536 (2019).

[181] H. Chen, B. Qu, D. Li, R. Zhou, and B. Zhang, *Atomic Structure and Dynamics Properties of Cu 50 Zr 50 Films*, J. Appl. Phys. **123**, 025307 (2018).

[182] *Continuum and Molecular Flow*, https://vacaero.com/information-resources/vac-aero-training/170466-the-fundamentals-of-vacuum-theory.html.

[183] *Rotary Vane Pump Schematic*, https://en.wikipedia.org/wiki/Rotary_vane_pump.

[184] *Cryopump Schematic*, https://cds.cern.ch/record/1047069/files/p241.pdf.

[185] *Continuum and Molecular Flow through Pipes*, https://vacaero.com/information-resources/vac-aero-training/170466-the-fundamentals-of-vacuum-theory.html.

Appendix A Magnetron sputtering chamber design and operation

This chapter aims to capture my experience with high vacuum chamber design, operation and maintenance. As I and my mentor, Dr. Felix P. Lu set out to develop a magnetron sputtering approach to fabricate metallic glass thin films, the first challenge for us was to resurrect a previously defunct sputtering tool. The desired functionality was split into two parts: one, we wanted to build a high vacuum deposition system which was pumped by a combination of a roughing pump, cryopump and LN_2-cooled cryotrap. Two, we needed a spinning substrate stage that could get hot while the alloy films were being grown by sputtering. Towards achieving this end, we had to contend with a range of issues. Briefly, we were able to individually troubleshoot all the vacuum components such as the various valves, process gas connections, vacuum feedthroughs, pumps, etc. We custom-built a heated spinning stage that is high vacuum compatible. We could diagnose electrical and vacuum-related issues with the sputter guns and their power supplies. We worked together with target manufacturers to get the desired sputter target composition and microstructural features. Personally, the learning experience was very rewarding, and I got a rigorous hands-on training in vacuum technology and equipment design.

A.1 Vacuum technology principles

The discussion in this chapter is based on the books, “The materials science of thin films” by Milton Ohring, “A user’s guide to vacuum technology” by John O’Hanlon and course notes from EP777 by Prof. John Pfotenhauer. In simple terms, achieving “vacuum” in a closed volume means to evacuate all gaseous molecules within this volume. Depending on the application and desired level of cleanliness, most vacuum systems used for research and development can be categorized into low (750 – 0.75 Torr), medium (75 – 0.75 mTorr), high (7.5×10^{-4} – 7.5×10^{-8}

Torr) and ultra-high vacuum systems ($7.5 \times 10^{-8} – 7.5 \times 10^{-13}$ Torr). These ranges are critical to identify pressure-dependent gas flow regimes and thus, advise design selection of vacuum components, pumps and operating and maintenance procedures. The well-established kinetic theory of gases can be applied to describe gas properties: important parameters like molecular density, mean free path, molecular velocity, gas temperature and their inter-relationships with chamber pressure can easily be calculated by standard relations. These equations can be easily found in standard physical chemistry textbooks.

Attaining the target vacuum level requires a thorough understanding of the gas flow regimes as related to pumping technology. Gas pressure primarily drives the way a gas flows inside a vacuum chamber. At rough vacuum, the molecular density is high, and their collisions are frequent, resulting in a flow dominated by these interactions. This means groups of molecules can be pumped out in a superimposed, ordered motion. The ordered motion results from internal friction between the molecules termed viscosity and hence, continuum or viscous flow dominates in rough vacuum as shown in Figure 62(a). On the other hand, intermolecular collision events are much scarcer in high and ultrahigh vacuum ranges. Individual molecules move freely and primarily collide with either the vessel walls or pipe connected to the high vacuum pumps. Typically, the mean free path for gas molecules is much larger than the pipe diameter and they can move in arbitrary directions, making continuum flow impossible. This gas flow regime is called molecular flow, as shown in Figure 62(b). In the intermediate or medium vacuum regime, gas flow characteristics are influenced both by intermolecular collisions and wall collisions, resulting in a transitional range called Knudsen flow. The gas flow regime drives the choice of vacuum pumps.

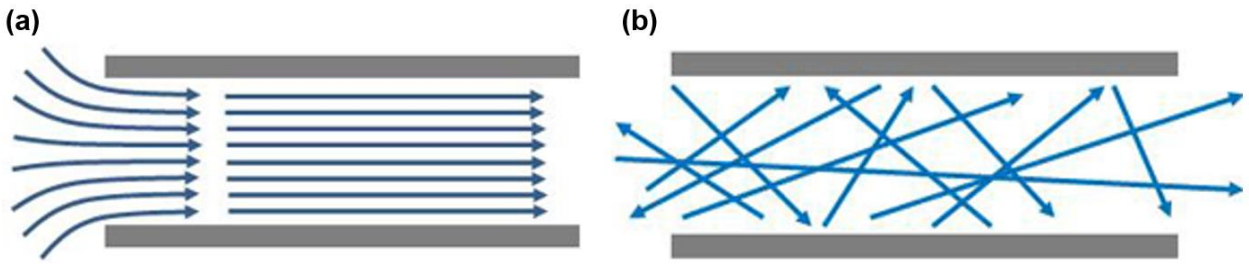

***Figure 62**: (a) Continuum flow and (b) molecular flow of gas molecules through a pipe are shown* [182].

Vacuum pumps used in the continuum gas flow regime include rotary vane pumps, scroll pumps, roots blower pumps, etc. They create suction to pull out gas volumes to the pump inlet, then expel the gas molecules through the pump mechanism to the atmosphere. As an example, rotary vane pumps (shown in Figure 63) are oil-based positive-displacement pumps comprising of vanes mounted to a rotor rotating inside a larger circular cavity. Positive displacement pumps move a fluid by trapping a fixed volume and displacing it into a discharge pipe. The circles' centers are offset, resulting in eccentricity. Vanes slide in and out of the rotor and seal at the edges, thereby creating vane chambers for the actual pumping. Vane chambers on the intake side increase in volume due to fluid being forced in by the inlet pressure of vacuum chamber. At the pump outlet side, vane chambers decrease in volume, expelling the fluid out of the pump, usually to atmosphere. These pumps can generate high throughput and fast pump-down to rough vacuum, with ultimate pressures as low as 0.1 mTorr.

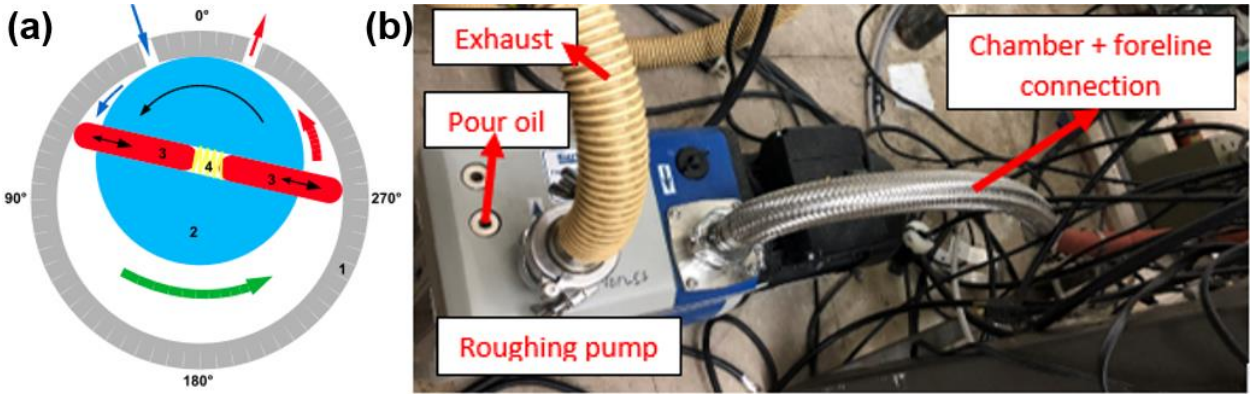

***Figure 63**: (a) Schematic* [183] *and (b) picture of a Kurt J Lesker Company's rotary vane pump are shown.*

Pump technology used in the molecular gas flow regime to reach high and ultra-high vacuum differs markedly from the low-vacuum pumps. These include cryogenic pumps, diffusion pumps, turbomolecular pumps, etc. Instead of "pulling" out gas molecules by suction, these pumps entrap molecules entering the pump inlet by physical or chemical interactions on their internal surfaces. For instance, consider a cryopump: pumping proceeds by relatively weak van der Waals' forces between the gas particles being pumped and a large, cold surface area provided by the cryopump. With adequately low temperatures, cryopumps can pump out all gases including noble gases. Modern cryopumps are cooled by closed-loop mechanical refrigerators using a He gas circuit. He is circulated continuously between a compressor and expander, connected with self-sealing, flexible hoses. These devices have two stages as shown in Figure 64(a): the first stage operates at 50 – 75 K and traps majority of all gases except H, He and Ne, while the second stage operates at ~ 10 K and immobilizes gases which make it past the baffle structures. At the first stage, condensate layers form by crystal growth out of the gas phase by a process called cryocondensation. The growth mechanism has three steps – thermal accommodation and adsorption of impinging gas flux at the surface followed by diffusion to the growth site and finally,

atomic incorporation. Cryocondensation proceeds by island nucleation and growth, resulting in non-uniform condensate thickness. With increase in thickness, the cryocondensation process can become inefficient to trap gases because of higher surface mobility. At the lower temperature second stage, gas particles lose so much of their incident energy that they stay attached to the cold surface by weak intermolecular forces or physisorption, also described as cryosorption due to the prevalent vacuum and temperature conditions. Cryosorption is aided by large surface area available due to the activated charcoal. The efficiency of cryopumping relies heavily on the ability to maintain low temperatures. From a design perspective, it is important to assess and mitigate the effects of heat loads arising from solid state conduction and radiative heat transfer from sources within the vacuum vessel. Placing a liquid nitrogen or even air-cooled cryotrap as shown in Figure 64(b) can provide a barrier to heat flow from chamber to cryopump. Since cryopumps can retain pumped gases until their capacity isn't exceeded and appropriately low temperature can be maintained, they must be regularly regenerated by heating up the cryosurfaces and pumping away the released gas particles by mechanical pumps for optimal operation.

To minimize chamber pump down times, we need to understand the parameters influencing gas flow, namely pumping characteristics, pipe diameter, pipe bends and devices such as filters and condensers. The rate at which gas is removed by pumps from a vacuum system is measured by a pumping speed, $S_p = dV/dt = Q/p$, where dV/dt gives the volume of gas removed from the system at an inlet pressure p and flow rate Q. Obviously, a high pumping speed bodes well for faster pump-down but that is not the only parameter. Another important metric is the concept of "conductance" in vacuum piping to "conduct" gas. Analogous to electrical systems in which wire conductivity dictates electron flow on account of an applied electrical voltage, conductance in

vacuum systems permits gas flow due to the pressure differential originating from vacuum pumps and is defined by $C = Q/\Delta p$, where Δp is the pressure differential. Conductance values depend on the gas flow regime: highest in viscous regime, lowest in molecular regime and intermediate in transition regime. This can be understood as follows: when a pressure differential is exerted in the viscous flow regime as shown in Figure 65(a), gas molecules move collectively and result in lower flow resistance. On the other hand, high vacuum pumps operating in the molecular regime rely on random walk of molecules to enter the pump inlet as shown in Figure 65(b). Finally, an effective pumping speed S_{eff} can be related to a pump with nominal pumping speed S_p and the total conductance of connections between pump and vacuum chamber, C_{tot} by the expression, $1/S_{eff} = 1/S_p + 1/C_{tot}$.

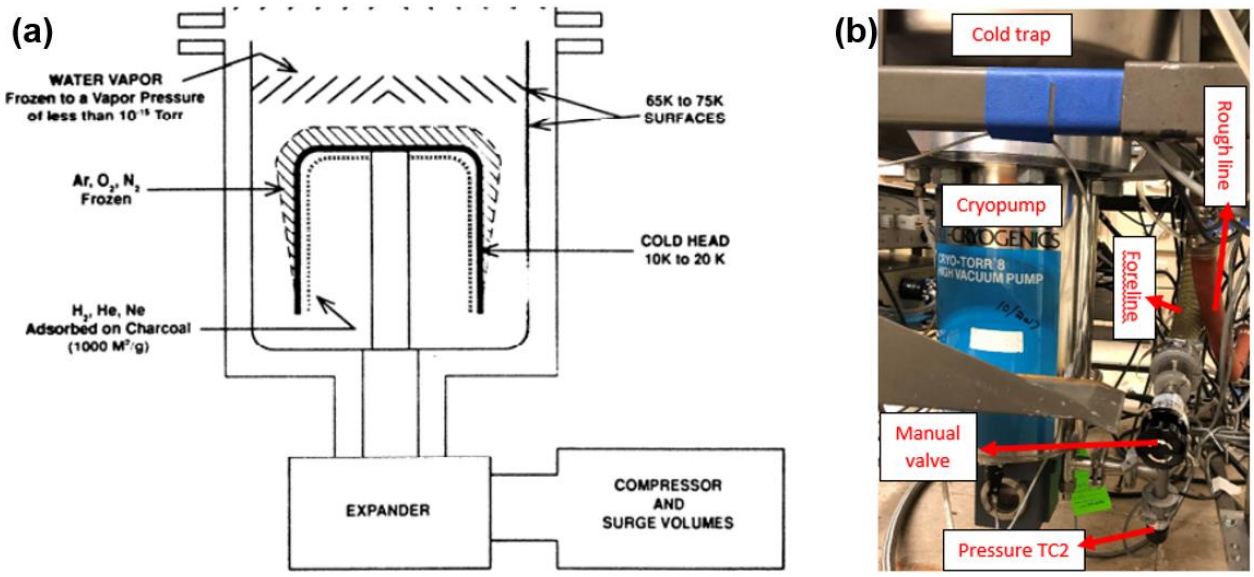

Figure 64*: (a) Schematic* [184] *and (b)picture of a cryopump are shown.*

The concepts of pumping speeds and conductance have important implications on vacuum system design and optimization. As noted above, conductance of a system is not constant but

changes with gas flow regime. When calculating system conductance, it is critical to consider dependence on conductance with system pressure. Particularly, conductance values are independent of pressure in the molecular range but depend on the system pressure in viscous and transient flow regimes. It is worth mentioning that conductance values of components such as valves, filters and traps are provided by manufacturers. Selection of the pumping system should be informed by the total system conductance such that it can provide the desired flow rate in each pressure range. Good design practice should include the following considerations:

1. Short pipe lengths and larger diameters should be preferred.
2. Piping diameter should either be same or greater than vacuum pump inlet.
3. The pumping system should be physically as close to the chamber as possible.
4. Bends, elbows and turns should be minimized.

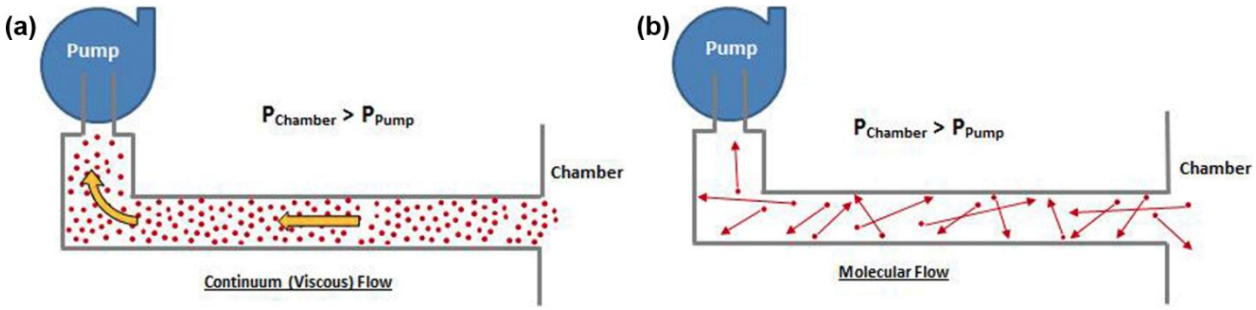

Figure 65*: Flow through a pipe in (a) continuum and (b) molecular ranges are represented* [185].

Now, we discuss working principles of commonly used pressure gauges in our vacuum system, specifically thermocouples, convectron Pirani and Bayard-Alpert ion gauges. All these gauges are indirect in nature: they record pressure by measuring a property that changes predictably with density. The thermocouple gauge (Figure 66(a)) measurement depends on thermal conduction of heat between a thin, hot metal strip heated by passing AC or DC current and the cold outer surface

of a glass tube (usually at room temperature). A heated metal wire suspended in gas will lose heat as gas molecules collide and remove its heat. If the gas pressure drops, the number of molecules fall off proportionately and the wire loses heat more slowly. The metal strip's temperature is measured by a thermocouple and depends on the thermal conductivity of gas in the tube, and hence its pressure as per kinetic theory of gases. A convectron Pirani gauge (Figure 66(b)) operates on the same principle of detecting thermal conductivity of gas due to change in temperature, except it senses the temperature by change in heated wire's resistance. Thermocouple and convectron Pirani gauges are typically used in the rough vacuum pressure range of $1 - 1 \times 10^{-4}$ Torr and $760 - 1 \times 10^{-4}$ Torr respectively. The Bayard-Alpert ion gauge (Figure 66(c)) is a sensitive gauge used for measuring very low pressures in high vacuum environments. An electrically heated filament produces an electron beam, which then travels through the gauge and ionizes surrounding gas molecules. Resulting ions are collected at negative electrode and the current depends on number of ions, which in turn depends on the gas pressure. These gauges are accurate for the pressure range $10^{-10} - 10^{-3}$ Torr.

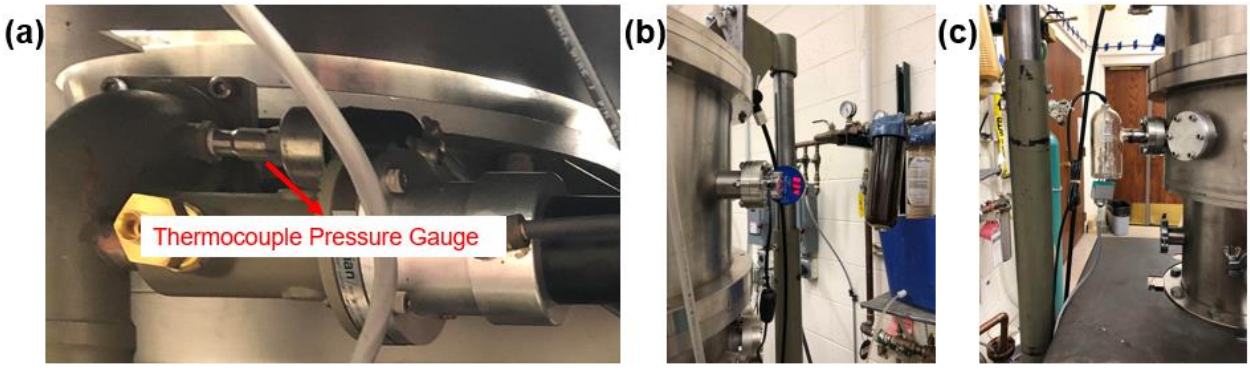

Figure 66*: Picture of (a) thermocouple, (b) Pirani, and (c) Bayard-Alpert ion pressure gauges are shown.*

No discussion of vacuum technology can be complete without referring to the arduous yet extremely important task of leak checking. Vacuum leak detection seems simple in principle: spraying the atmosphere side of the leak with a gas or liquid that triggers a different response than air on a "detection device". Vapor then diffuses through the leak and the detection device picks it up. In practice, this concept is merely a starting point along with the limited knowledge that the pressure is higher than expected. In addition to a leak, other factors can be at play: outgassing from heating and new vacuum components, venting to humid atmosphere, failure of high vacuum pump, etc. Further, leak detection is complicated by ability to reach all joints with test gas, tracking all the joints that were sprayed, water line leaks into the chamber, etc. After verifying that the system indeed leaks, it is helpful to rank places most likely to leak such as o-ring seals, metal gaskets, electrical feedthroughs, shut-off valves, chamber welds, etc.

The choice of leak checking procedure depends on the leak size. For relatively big leaks that won't allow the chamber to go into high vacuum, two most promising tests are positive pressure test and spraying isopropanol at the joints. For the positive pressure test, a constant stream of dry nitrogen is passed into the chamber and a thick, viscous soap solution (commercially called "snoop") is sprayed at the joints. At leaky joints, the soap will form bubbles and indicate a leak. For the isopropanol test, the chamber is pumped down to rough vacuum until the pumping speed is close to zero (but far from its ultimate pressure) and then isopropanol is sprayed at the joints. One of two things will happen in case of a leak: either the isopropanol vapor will enter the chamber and cause a pressure spike, or it will freeze hence plugging the leak and cause the chamber pressure to go down.

For relatively smaller leaks that allow the chamber to go into high vacuum regime (< 10^{-4} Torr), either a He leak detector, or a residual gas analyzer (RGA) are good choices. A He leak detector is a self-contained mass spectrometer tuned to the mass of He. After pumping the chamber and the leak detector to the lowest pressure it will go to, He is sprayed at all the joints sequentially and the leaky joints will cause a spike in the detector signal, thus identifying the leaks. The RGA is a more sophisticated mass spectrometer that can detect different gases making up the background. It can be operated in the He leak detection mode to double up as a He leak detector. However, its true value lies in its ability to give a break-up of all the gases making up the background gas, such as shown in Figure 67: in a leaky vacuum system made of stainless steel, the RGA will typically show that nitrogen peak is the tallest amongst air constituents and the nitrogen-to-oxygen partial pressures' ratio is ~ 4, representing air is present. In a vacuum system with no leaks, the water vapor peak will be the taller than other air constituents, due to a slow monolayer-wise desorption off the chamber walls.

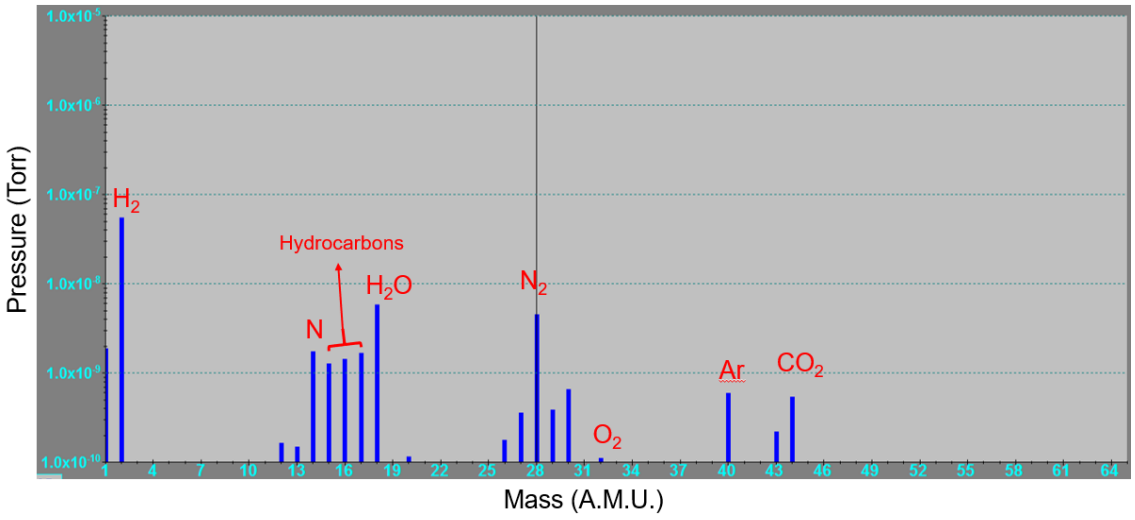

***Figure 67**: Example RGA plot shows residual gas composition with no leaks.*

A.2 Overview of deposition chamber

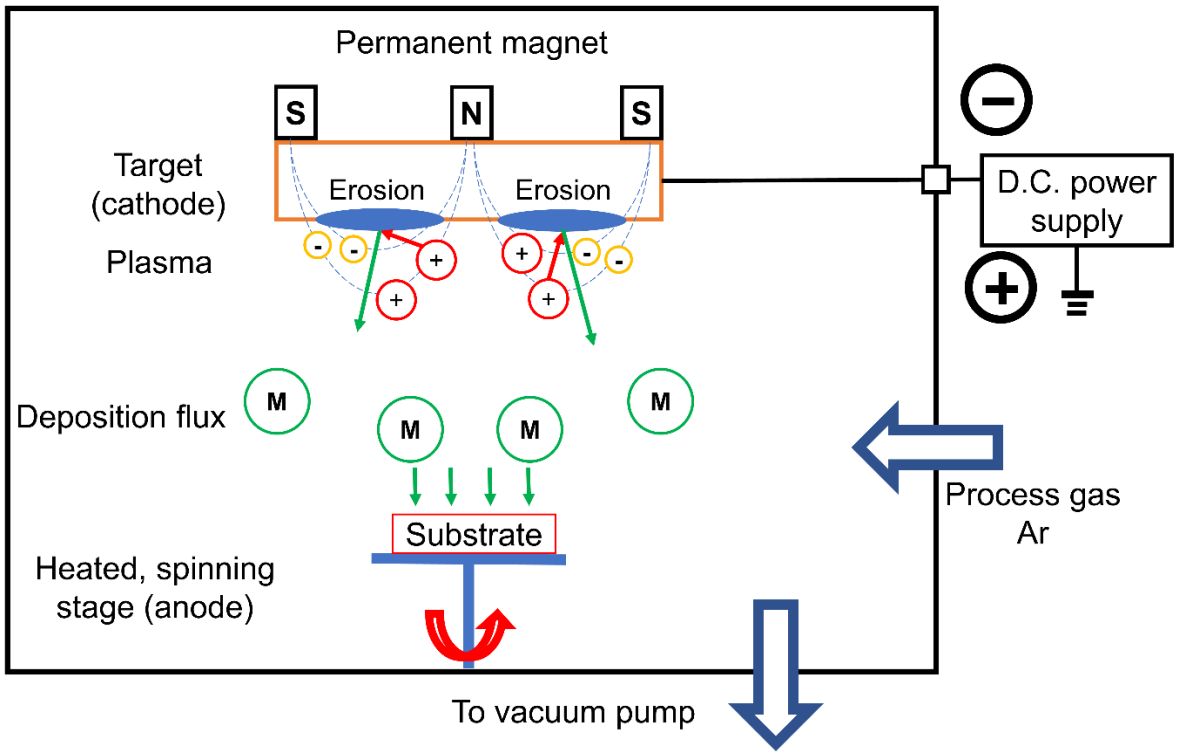

***Figure 68**: Simple schematic represents different parts of the sputtering system.*

Our high vacuum chamber for DC magnetron sputtering (simple schematic shown in Figure 68) has the following main parts:

1. The vacuum vessel is pumped to high vacuum by a combination of roughing pump (760 Torr to 20 mTorr) and cryopump aided by liquid nitrogen cooled cold trap (~ mid 10^{-8} Torr). Pump-down relies on the pumping system, pneumatic and manual hand valve systems, various types of thermocouples for pressure monitoring and the supporting connections to keep cryopump running.
2. The spinning heated stage is two part: one is the heater assembly itself, connected to its controller via feedthroughs and the other is the spinning stage, with motor outside the chamber.

3. The process gas connections are all metal tubings and manual valves connected to a BIP-grade (highest purity available) argon cylinder while the venting is by industrial grade dry nitrogen.
4. The sputter gun assembly is controlled by a DC power supply and requires cooling water to be turned on before operation.

A.3 Substrate cleaving, cleaning and curing

A.3.1 Cleaving Si wafer

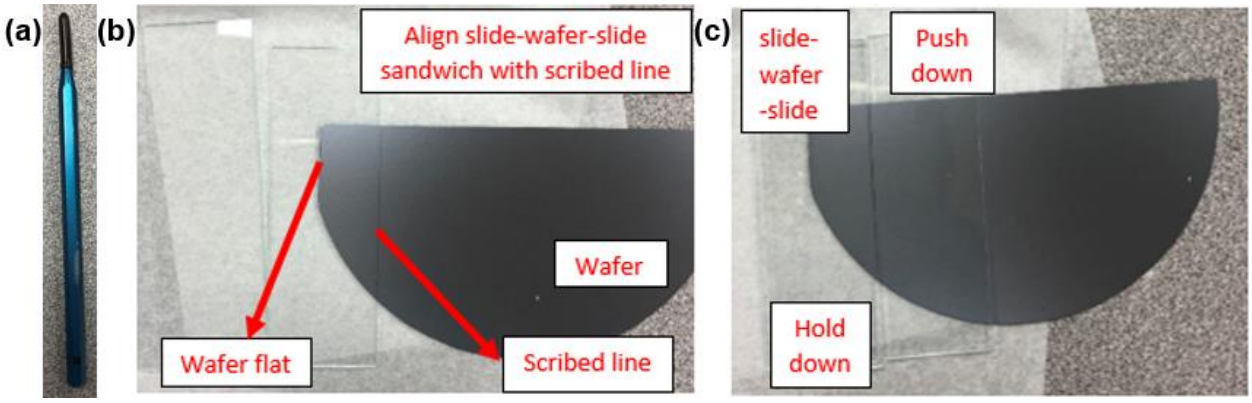

Figure 69*: (a) Picture of a diamond scribe, (b) and (c) show steps to cleave a Si wafer.*

1. Carefully place SiN-coated Si wafers with clean plastic tweezers on a kimwipe on a flat work desk with the shiny side facing down.
2. Using a diamond scribe and ruler, scratch straight lines either parallel or perpendicular to wafer flat.
3. Take three clean glass slides, place the wafer between two slides and align the scratch you made to the two slide edges.
4. Hold down the slide-wafer-slide sandwich firmly, then place the third glass slide along straight line and push down firmly to cleave.

A.3.2 Sample mounting – thick samples

1. Normal 2 cm x 2 cm SiN on 001 Si, 2 cm x 1 cm Al on 001 Si (dissolvable substrate), 5 min sonication with solvent sequence: acetone – IPA – methanol – DI water.
2. Blow dry with nitrogen, make sure to clean C-paste residue on alumina plate with a blade and DI water, then blow dry.
3. Apply carbon paste (a thin uniform layer, not too much), press on sides of substrates so they stick, then program 3-cure cycle (overnight recommended) on heater (a. 3 hr at 35°C, b. 3 hr at 93°C, c. 3 hr at 260°C), let it cool down before handling.

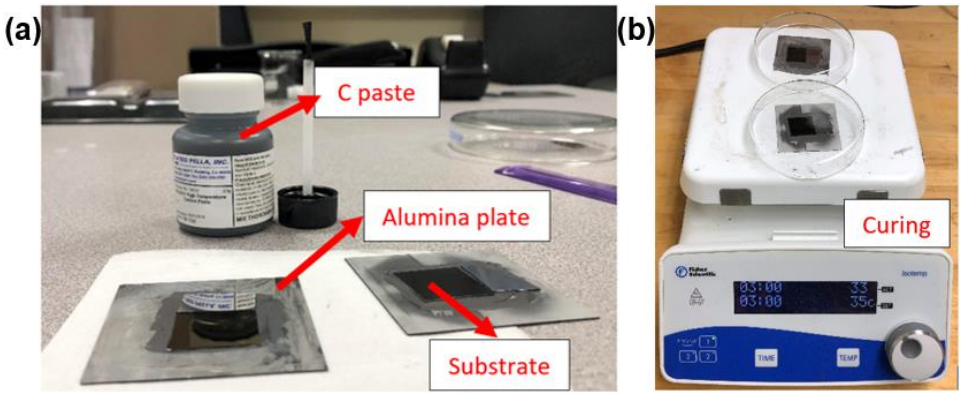

Figure 70*: (a) and (b) show steps to mount and cure a Si wafer substrate.*

A.3.3 Sample mounting – thin samples for TEM

1. Take off rotating platen by unscrewing the middle screw.
2. Place bare alumina plate in the slot and apply a layer of C-paste.
3. Keep the stainless-steel holder lightly on the paste, then adjust so that a small portion of the 3 mm TEM window grid is bolted down by Cu strip (so the grid can't fly off during pumping).
4. Then put on a sister SiN on 001 Si substrate for other studies such as roughness, XRR, etc.

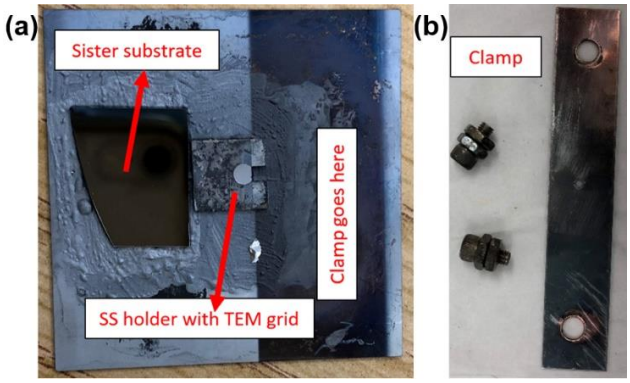

Figure 71*: (a) and (b) show steps to mount and cure an electron-transparent window for TEM studies.*

A.4 Temperature Calibration (this step is required before each deposition)

1. Place substrate and alumina plate assembly carefully on spinning stage then slide slowly into slot.
2. Place TC on substrate surface (a corner), hold down by weight as shown in **Figure 72**.

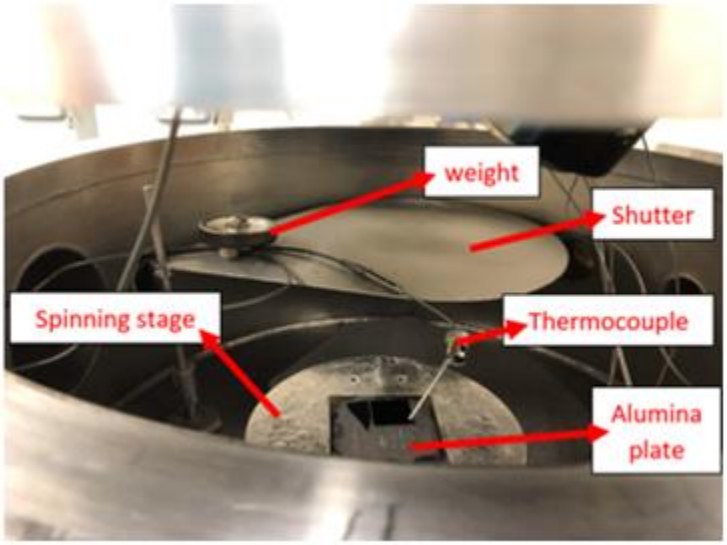

Figure 72*: Picture shows set-up for temperature calibration and the various parts.*

3. Lower chamber top, watch that TC doesn't move, push the chamber top to align with bottom, pump down with rough pump until 20 mTorr as read by TC1, switch to cryopump by first closing rough valve and then opening the hi-vac valve (**BE CAREFUL**, never open hi-vac with rough valve open).
4. Allow system to pump down to ~ 2×10^{-7} Torr (takes about 5-6 hours), then pour 4 liters of LN2 into the cold trap, wait 30 – 60 min before the ion gauge reads $5 – 7 \times 10^{-8}$ Torr (how to read pressure at high vacuum: long press ON button on the 843 ionization gauge shown in Figure 73 until filament turns on, then read from the display on left, there is a knob to set the pressure scale).
5. Ramp up to desired power over 10 min in 5 ramp-steps, wait 2 minutes before next ramp (**NEVER EXCEED 30% power**).
6. Heater currently takes 1 hour to equilibrate (10 min ramp + 50 min equilibration).

***Figure 73**: Picture shows the various parts making up 843 ionization gauge readout.*

7. First, make sure ion gauge is turned off (long press OFF) before flowing any Ar gas. Then flow Ar at 55 min mark (open Ar cylinder valve, Vernier valve is adjusted for 1 mTorr as measured by old Stinger gauge (don't touch it unless you want to change Ar pressure), open Swagelok shut-off valve all the way, then back up just a little to prevent the valve from getting stuck).

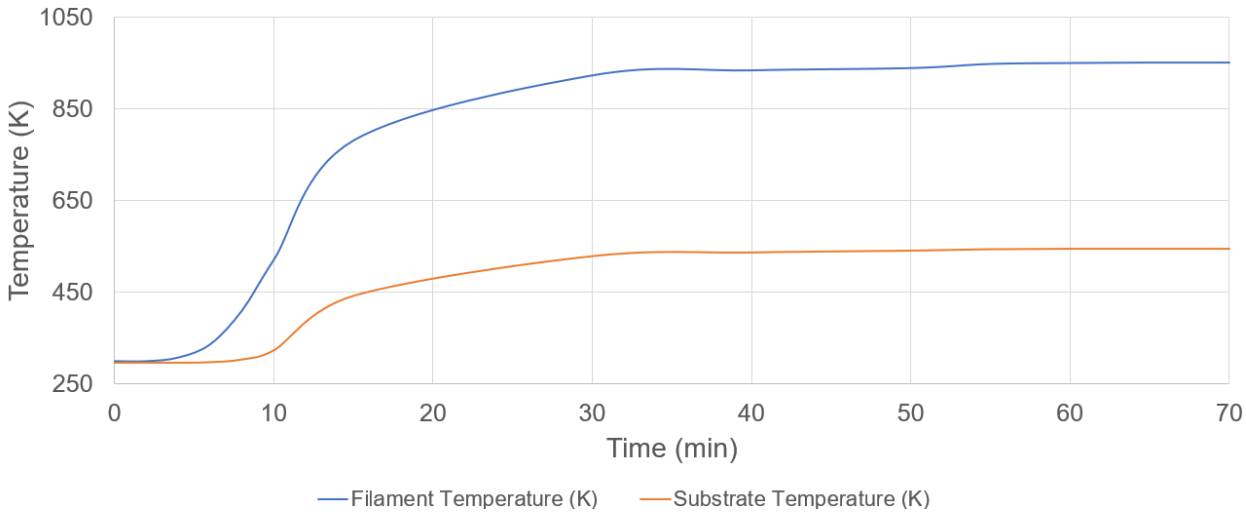

***Figure 74**: Example calibration plot of filament and substrate temperatures is shown.*

8. Turn off heater all the way (okay to kill power immediately), close shut off valve very carefully and slowly until resistance is felt (don't close too hard, it is very easy to break).
9. Close hi vac valve (wait for two clicks – 1. Gate valve slides out, 2. Gate valve latches on and forms an o-ring seal to isolate cryopump from chamber), flow dry N2 through metal gas lines for a couple of minutes, then open air release valve to vent.
10. Wait until N2 can be felt flowing out of chamber (easiest to feel at divide between chamber bottom and liftable top).

A.5 Deposition

1. Post temperature calibration and venting the system, take off the temperature thermocouple T1 on top of substrate and the weight holding it down, and leave it on chamber floor.
2. Lower the chamber top, align top with bottom by slowly and slightly pushing the chamber top.
3. Swing the shutter with hand knob at chamber bottom to make sure it can swing freely (and isn't blocked by any wires).

4. Rough pump to ~ 20 mTorr as read by TC1, then switch to cryopump as stated previously.
5. Allow system to pump down to ~ 2×10^{-7} Torr (takes about 5-6 hours), then pour 4 liters of LN2 into the cold trap, wait 30 – 60 min before the ion gauge reads $5 – 7 \times 10^{-8}$ Torr.
6. Ramp up using same ramp function as temperature calibration.

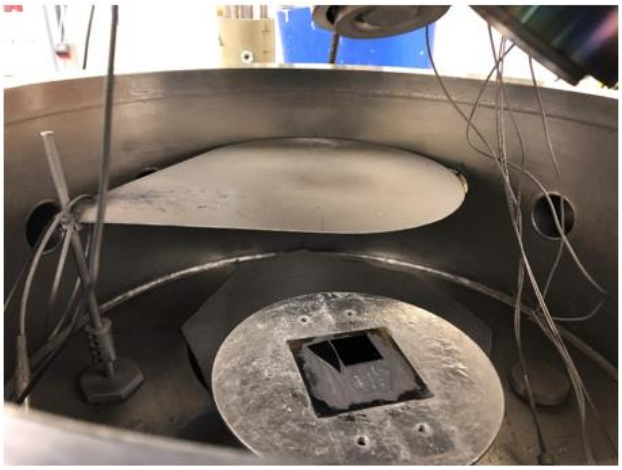

Figure 75*: Picture shows a peek inside the chamber before running actual deposition.*

7. Heater currently takes 1 hour to equilibrate (10 min ramp + 50 min stabilization).
8. Flow Ar at 55 min mark (open Ar cylinder valve, Vernier valve is adjusted for 1 mTorr as measured by old Stinger gauge (should be reproducible every time, don't touch it unless you want to change Ar pressure), open Swagelok shut-off valve all the way, then back up just a little to prevent the valve from getting stuck). Gas pressures ranging from 1 to 7.5 mTorr as measured by the Stinger gauge were previously used. Choose the minimum operating pressure such as to get the desired film composition. So, a simple calibration experiment would be to grow 500-600 nm thick films at three pressures (try 1, 2, 3 mTorr) and same power to see if there is any composition dependence. Choosing the lowest pressure that gives the correct composition is important to avoid Ar inclusion inside films.

9. Allow 10 min for Ar gas stabilization. In these 10 minutes, set the desired power on DC power supply in the following way:
    a. turn on power button (left side),
    b. make sure the desired control parameter is set (power, voltage or current) on the regulation (left side), on right display,
    c. press set-point (red LED will light up), set desired value of P/V/I by rotating the big knob on bottom right,
    d. set ramp period by adjusting the "ramp adjust" knob. (choose between 1-10 s and 1-10 min from a switch at the back – check power supply manual to figure out which of the three switches it is, recommended: 1-3 minutes for powers above 100W)
    e. Now the deposition P/V/I is set. To read the right display's P, V and I output, toggle by pressing the "actual" button. Periodically note these values as they are helpful with diagnostics later.
    f. We have two operational power supplies: for powers 0-300 W, use the 1K MDX. For powers greater than 300W, use the 1.5K MDX. Be careful to incorporate enough ramp time to not thermally shock the target (basically go slow on the ramp – a good rule of thumb is 50-75 W/min).
10. About a minute before pre-sputtering turn on the motor for stage rotation (currently set to 6 RPM, can be adjusted by the power supply).
11. Before actual sputtering, do a pre-sputtering step for target surface cleaning: firstly, close the shutter with hand-knob, start the P/V/I ramp, then let the target sit at the preset P/V/I value for 30 seconds. Pre-sputter is now done.

12. Now open the shutter and allow the deposition for desired time. No matter what mode of regulation is being used, periodically read the P, V and I off the power supply's display. This is especially important for diagnostics.
13. After the time is up, close everything in the following order:
    a. turn off sputter power,
    b. the heater power,
    c. turn off stage rotation
    d. Close the shut-off valve slowly and carefully until resistance is felt
    e. Now let the sample sit in high vacuum for 2-3 hours to cool. Never open immediately, otherwise the sample will oxidise.
14. Now vent the chamber to retrieve the sample.

A.6 Sample storage

The thick samples are cleaved and resulting two pieces are stored separately: one goes to the back of the N2 storage box permanently, the other goes in and out of the storage box for measurements (typically XRD, SEM-EDS, SEM imaging, AFM, nanoindentation, flash DSC).

A.7 Target change

We have two sputter guns on the chamber. Targets should have a backing plate with a single hole to put on magnetic disc: the target is held on magnetically onto the gun.

1. To put a new target on, first screw on the magnetic disc, then spread a light layer of Apiezon vacuum grease on the back of the target.
2. Bring the target near the sputter gun, let it be pulled by the magnetic field, then adjust so that the magnetic disc slides into its designated slot. Now press the target lightly on the sides.

NEVER TWIST since that would break the intimate contact between target and gun cooling well (which is very bad for cooling and can break the target).

3. To take target off, pull lightly and carefully by gripping on the sides until it comes off.

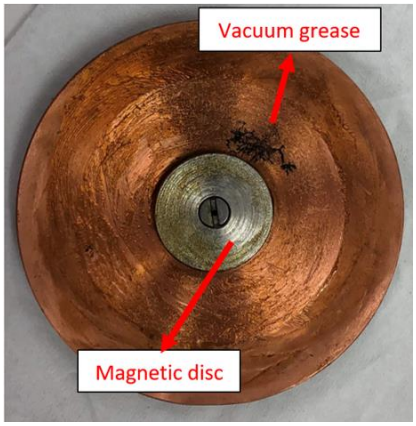

***Figure 76**: Picture shows the backside of a target with the magnetic disc fastened and vacuum grease applied.*

A.8 Periodic maintenance

1. Replace adsorber filter of cryopump every 12 months (refer to manual for instructions).
2. Pour machine oil in hoist for smooth operation every 6 months.
3. Check oil level in rotary vane pump periodically and fill if necessary.
4. Change water filters in cooling line every 3-4 months or if they become visibly dirty.
5. Change out N2 cylinders when empty.

A.9 Troubleshooting

The three most common problems encountered with the cryopump are as follows:

1. While connecting self-sealing He lines to cryopump and compressor, static He pressure drops below 250 psi. Remedy – fill UHP grade He (atleast 99.999% purity) as per manual instructions.
2. Water condensation on the outside of cryopump – usually indicates a big air leak to the cryopump. Remedy – isolate cryopump with hi-vac valve, leak check and fix them.
3. Upon cooling down the cryopump, you hear a loud grinding noise which goes away on warming up and returns upon cooling down – He gas circuit is contaminated. Remedy – run He circuit decontamination procedure as per manual instructions using He manifold.